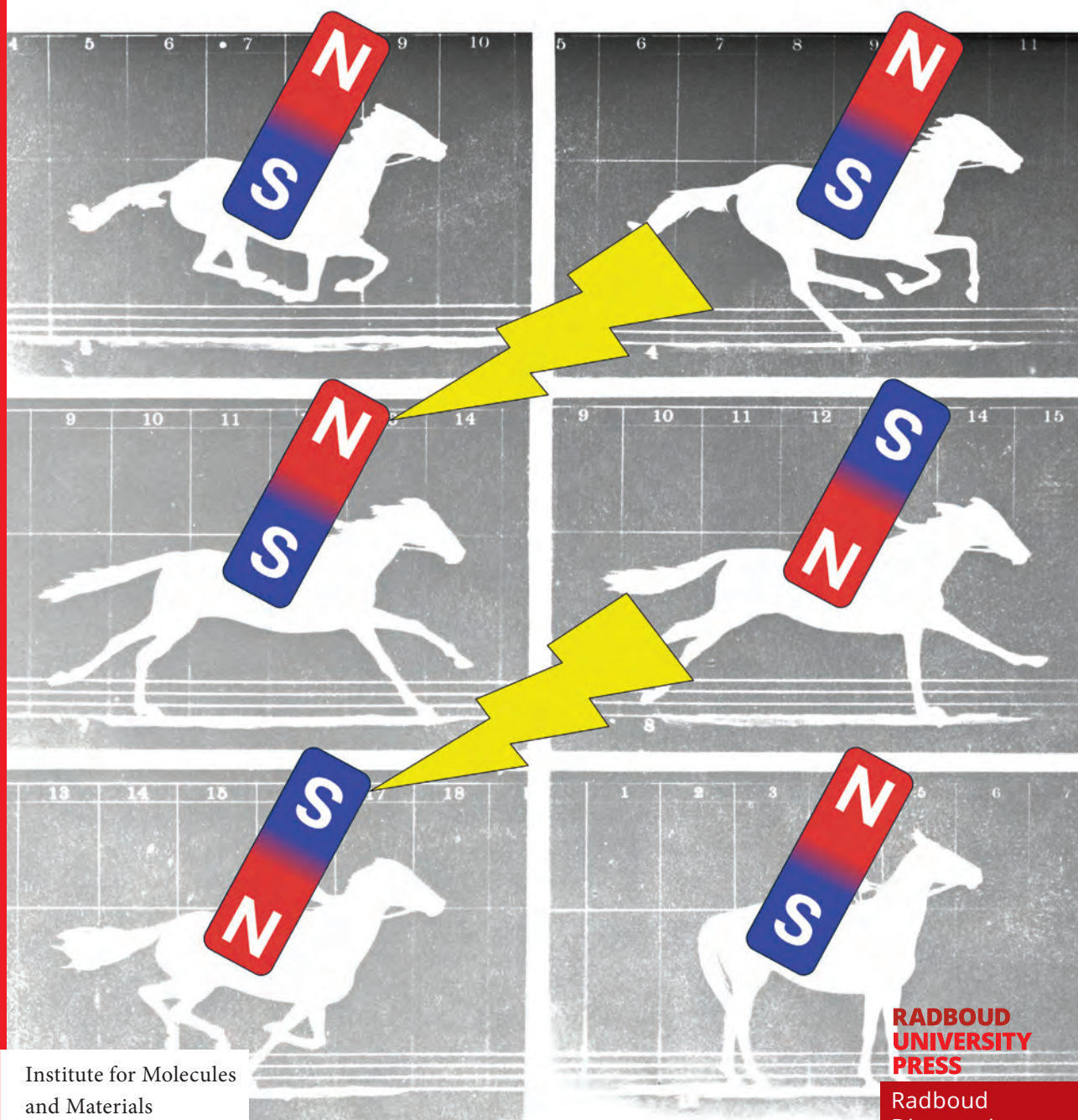


Ultrafast Dynamics of Magneto-Electrics

Timur Gareev



Ultrafast Dynamics of Magneto-Electrics

Timur Tagirovich Gareev



The work described in this thesis has received funding from the European Union's Horizon 2020 Research and Innovation Program under Marie Skłodowska-Curie Grant Agreement No. 861300 (COMRAD).

Ultrafast Dynamics of Magneto-Electrics

Timur T. Gareev

Radboud Dissertation Series

ISSN: 2950-2772 (Online); 2950-2780 (Print)

Published by RADBOUD UNIVERSITY PRESS

Postbus 9100, 6500 HA Nijmegen, The Netherlands

www.radbouduniversitypress.nl

Design: Timur T. Gareev

Cover and illustrations: Timur T. Gareev

Cover image based on "The Horse in Motion" (1878)

by Eadweard Muybridge (public domain)

Printing: DPN Rikken/Pumbo

ISBN: 9789465151441

DOI: 10.54195/9789465151441

Free download at: <https://doi.org/10.54195/9789465151441>

© 2025 Timur T. Gareev

**RADBOUD
UNIVERSITY
PRESS**

This is an Open Access book published under the terms of Creative Commons Attribution-Noncommercial-NoDerivatives International license (CC BY-NC-ND 4.0). This license allows reusers to copy and distribute the material in any medium or format in unadapted form only, for noncommercial purposes only, and only so long as attribution is given to the creator, see <http://creativecommons.org/licenses/by-nc-nd/4.0/>.

Ultrafast Dynamics of Magneto-Electrics

Proefschrift ter verkrijging van de graad van doctor
aan de Radboud Universiteit Nijmegen
op gezag van de rector magnificus prof. dr. J.M. Sanders,
volgens besluit van het college voor promoties
in het openbaar te verdedigen op

woensdag 3 december 2025
om 14:30 uur precies

door

Timur Tagirovich Gareev

geboren op 17 augustus 1996
te Davlekanovo, Rusland

Promotoren:

Prof. dr. A.V. Kimel

Prof. dr. T.H.M. Rasing

Manuscriptcommissie:

Prof. dr. A.A. Khajetoorians (voorzitter)

Prof. dr. M.V. Mostovoy (Rijksuniversiteit Groningen)

Dr. I.L. Prejbeanu (CEA, Frankrijk)

Preface

My journey began in February 2020, when I arrived in the Netherlands to study at Radboud University for six months and conduct my MSc project under the supervision of Alexey Kimel and Theo Rasing. I greatly enjoyed meeting new people and following inspiring courses on Light–Matter Interaction, Fundamentals of Magnetism, Lasers and Electro-Optics.

In March 2020, the university closed due to quarantine, and my planned experiments came to a halt. Work resumed in July, but with only a month left before returning home, there was little time to begin a new project. Still, Alexey and I discussed future research ideas, and a year later, in September 2021, I joined the group as a PhD candidate within the COM-RAD project.

From that moment, I focused on my first independent projects, supported by many wonderful people to whom I am deeply grateful.

First and foremost, I owe my sincerest thanks to my supervisor and mentor, Alexey, for your invaluable guidance, belief in me, and constant encouragement throughout these years. Your feedback and support were crucial in shaping my research and helping me overcome challenges. Much like in my 5 km record run, where I broke my personal best with your help, you pushed me to surpass my own limits in science as well.

I would also like to thank Theo, and your grandson Manoah, for your invaluable help in shaping this dissertation and for your sharp eye for detail. Without your support, this work would not have been possible.

My heartfelt thanks go to Dima, for your steady stream of ideas, enthusiasm, and mentorship from the very beginning. It was also a pleasure to co-host the Photonics course for MSc students with you.

To Nikolai, I am grateful for your rigor and structured approach to our projects, as well as the many enjoyable moments inside and outside the lab.

I am glad to call you not only a colleague but also a friend.

To Sasha and Ira, who guided my very first steps in both the lab and the Netherlands, I feel fortunate to have you as friends.

Many thanks to Sergey, who introduced me to ultrafast laser systems and optical alignment. I am glad we have remained in contact.

To Chris, thank you for your support in the lab and for our always enjoyable conversations. En hartelijk bedankt dat je altijd in het Nederlands met me praat zonder over te schakelen!

To Kamyar, our adventurous climb to the Swiss waterfall remains unforgettable, just as in the lab, you made sure we always found the safest path forward. I look forward to the outcome of our ongoing project.

To Marilou, thank you for your constant support in everyday matters and for organizing so much behind the scenes.

I would also like to thank my colleagues at NXP, Marc van Veenhuizen and Jeroen Jalink, for giving me the opportunity to explore the world of Failure Analysis. The outcome of our work led to an NWO grant, and I am pleased that our collaboration continues.

I am grateful as well to the members of our group: Victoria, for our many pleasant conversations. Lukas, for your patience and thoughtful discussions during our joint project. Vlad, for always being a reliable colleague and a true friend when it matters most. Dinar, for your expertise that brought great results to our work. Jim, ik vond het altijd leuk om met je samen te werken en ben blij dat we het probleem met symmetrie uiteindelijk hebben opgelost! Shuang, though you joined only recently, your expertise already shines – I know the Kaleidoscope setup is in good hands. Peter, thank you for your support and assistance with the new laser system. Ketty, I appreciated having the opportunity to work together in the lab when you first joined our group. Paul en Wiebe, het is altijd gezellig om met jullie te praten! Hrvoje, for organizing such enjoyable PPIMM activities.

I also want to thank those I met during my very first stay in Nijmegen. To Andrei Kiriliouk, for teaching the Fundamentals of Magnetism course. To Fabio, for inspiring tutorials and for showing me how to work with the Kaleidoscope setup. To Kirill, for kindly introducing me to the details of pump-probe spectroscopy. To Qiao and Xinuye, for your warm welcome.

To Long Cheng, I am grateful for your friendship and glad that we remain in touch. I still fondly remember our trip to London and our long

Skype sessions during the corona period.

My thanks also go to Rostislav, Mikola, Oleksander, and Yuichi for welcoming me into your group in Lancaster. Even during my one-month in May 2024, we achieved strong results together.

To Andrzej Stupakiewicz, thank you for the stimulating scientific discussions at conferences and project meetings.

I also wish to express my deep gratitude to Alexander Pyatakov from Lomonosov Moscow State University. You were my supervisor during both my BSc and MSc studies, and I am glad we remain in close contact and continue to collaborate.

Aan mijn taalmaatje, Jos Compen: hartelijk dank dat je me hebt geholpen mijn Nederlands te verbeteren! Het is altijd best leuk om met je te praten.

Of course, my deepest thanks go to my family. To Lida, my girlfriend – thank you for your constant support and belief in me. I am immensely happy to have you by my side. I love you very much.

To my mother and father, thank you for your unwavering encouragement. To my brother Shamil, for always being there. To my grandmother, who instilled in me a love for mathematics and running, and to my aunt and mother for nurturing my passion for science from childhood – I owe you all a great deal.

Finally, I would like to thank the members of my thesis committee. To Alexander Khajetoorians, for your valuable comments and insightful discussions. To Maxim Mostovoy, whom I was glad to finally meet in person this summer – I greatly enjoyed our exchange during the GRC conference. And to Lucian Prejbeanu, for evaluating this work and inspiring talks during COMRAD meetings.

I also extend my sincere thanks to all committee members for their time and thoughtful evaluation of this thesis.

Someone once said, “*A PhD is not a sprint, it is a marathon*”. Over these years, those words became more than a metaphor. I have not only run the long race of a PhD, but also tested myself on real marathon tracks – crossing the finish line in Rotterdam in 2023 and now preparing for another in Eindhoven this October.

Like every marathon, a PhD requires endurance when energy is low, perseverance when the path seems endless, and the discipline to keep mov-

ing forward, one step at a time. And just as a runner approaches the finish line with a mix of exhaustion and triumph, I now reach the final stretch of this academic race with gratitude, pride, and a profound sense of accomplishment. To everyone who stood by me along the way – thank you very much. I hope you enjoy reading this thesis.

Timur
Nijmegen, 23 September 2025

Contents

1	Introduction	1
1.1	Introduction	2
1.2	Magnetism	6
1.2.1	Magnetism fundamentals	6
1.2.2	Types of magnetic ordering	7
1.2.3	Magneto-electric effects	11
1.3	Ultrafast control over magnetization	15
1.4	Scope of the thesis	18
	References	20
2	Experimental Methods	25
2.1	Introduction	26
2.2	Light-matter interaction	26
2.2.1	Linear optical response from a thermodynamic perspective	26
2.2.2	Second harmonic generation fundamentals	27
2.2.3	SHG-based approach of antiferromagnetic order imaging in Cr_2O_3	29
2.3	Optical pump-probe spectroscopy for ultrafast lattice and spin dynamics	30
2.3.1	Ultrafast laser systems and pulse characterization	30
2.3.2	Introduction to the pump-probe technique	32
2.4	Magneto-optical imaging of spin dynamics	33
2.4.1	Experimental setup for spatially resolved measurements	33
2.5	Integration of electric fields with optical measurements	34
2.5.1	Electrical gating in ultrafast spin dynamics	34

2.5.2	SHG imaging of antiferromagnetic domains under a locally applied electric field in Cr_2O_3	37
2.6	Conclusion	39
	References	41
3	Strongly inhomogeneous spin dynamics induced by ultra-short laser pulses with a gradient intensity profile in magnetoelectric iron garnet	45
3.1	Introduction	46
3.2	Experiment	46
3.3	Results and discussion	48
3.4	Conclusion	53
	References	54
4	Electrically-gated laser-induced spin dynamics in magnetoelectric iron garnet at room temperature	57
4.1	Introduction	58
4.2	Sample and experimental setup	58
4.3	Results and discussion	61
4.4	Conclusion	65
	References	66
5	Electric field control of an antiferromagnetic domain wall in Cr_2O_3	69
5.1	Introduction	70
5.2	Sample and experimental setup	71
5.3	Results and discussion	72
5.4	Conclusion	78
5	References	79
	References	79
6	Optical excitation of coherent THz dynamics of the rare-earth lattice through resonant pumping of an $f - f$ electronic transition in the complex perovskite DyFeO_3	81
6.1	Introduction	82
6.2	Sample and scheme of the experiment	83
6.3	Results and discussion	85

6.4 Conclusion	92
A Additional Data	95
A.1 Frequencies of Raman-active phonons in DyFeO ₃	95
References	97
Summary	103
Samenvatting	107
Research Data Management	111
List of Publications	113
Curriculum Vitae	115

Chapter 1

Introduction

This chapter is meant to briefly introduce the subject of the thesis – ultrafast laser-induced spin dynamics in magneto-electric media. Starting with a very general view on the problem of the evolution of data storage technology over the past decades, the chapter shows how the research discussed in the thesis can potentially contribute to future technology. Further, the chapter introduces the basic fundamental principles of magnetism, including various types of magnetic ordering and methods for controlling magnetic states. Regarding the focus of the thesis, special attention is paid to the control of magnetism using electric fields and ultrashort pulses of light.

1.1 Introduction

The ability to store, retrieve, and manipulate information has driven technological innovation for centuries, transforming societies and economies alike. From the first mechanical systems to modern-day magnetic and electronic solutions, data storage has evolved to meet the ever-growing demands of an increasingly interconnected world. This growth is now fueled by revolutionary developments in artificial intelligence (AI), big data analytics, blockchain technology, and all other modern technologies, which have collectively contributed to an unprecedented surge in global information generation. Data storage began in the early 19th century with punch cards, which offered a basic but effective means of encoding binary information. By the mid-20th century, the advent of magnetic tape revolutionized data management, enabling larger storage capacities and faster access compared to punch cards. Magnetic tape became an essential element of early computing, laying the groundwork for advancements in scientific research and commercial data processing. This was followed by the introduction of magnetic disk storage, created by IBM's groundbreaking 305 RAMAC in 1956 [1], the first hard disk drive capable of storing 5 megabytes of data on a series of rotating magnetic platters. The advent of hard disk drives (HDDs) marked an essential moment in data storage history, still offering the cheapest and the most reliable way to store information. The rise of the semiconductor industry in the second half of the 20th century further transformed the landscape. Advances in materials science, such as the development of silicon-based technologies, enabled the creation of smaller, faster, and more energy-efficient devices. This progress not only improved storage systems but also accelerated innovations in computation, forming the basis for modern data processing infrastructure. Concurrently, flash memory and solid-state drives (SSDs) emerged. SSDs quickly gained prominence in portable devices and high-performance computing applications, although magnetic storage remained dominant in enterprise and cloud systems due to its superior cost-to-capacity ratio.

Today, the exponential growth of information is driven by the convergence of technologies such as AI, big data, and blockchain. AI algorithms, particularly those in machine learning and deep learning, require colossal datasets for training and optimization [4, 5]. This need has led to the creation of data centers housing petabytes of information, much of it stored on magnetic drives optimized for large-scale, sequential access. Big data analytics, spanning industries from finance to healthcare, relies on similar infrastructures to process vast quantities of structured and unstructured data. Blockchain technology, with its decentralized and immutable ledger, introduces new challenges, as every transaction must be stored redundantly across distributed networks, further amplifying storage requirements. The sheer volume of data generated is astonishing. In 2025 alone, global data

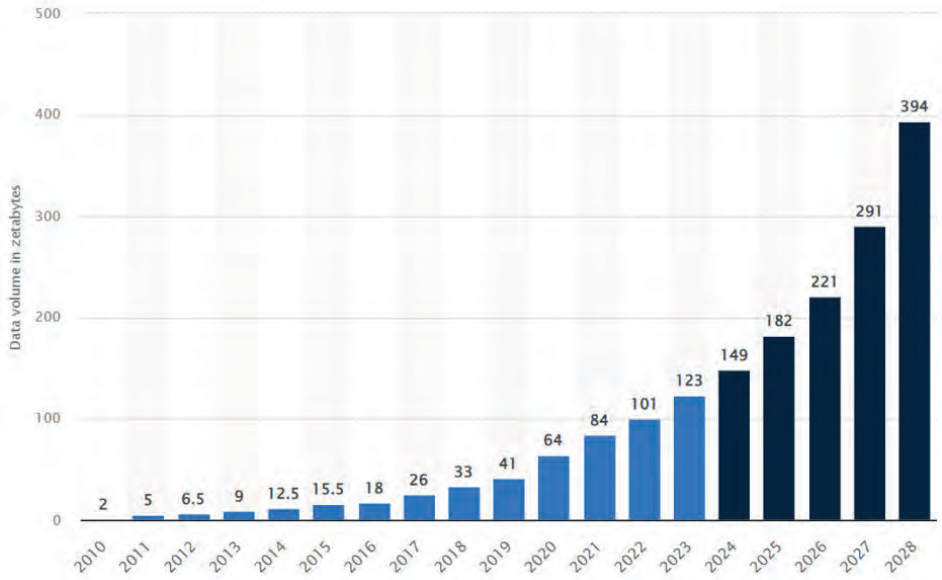


Figure 1.1: The volume of data/information created, captured, copied, and consumed worldwide from 2010 to 2024, with forecasts from 2025 to 2028 (in zettabytes) [2].

creation was estimated to exceed 180 zettabytes (1 zettabyte = 10^{21} bytes!), with projections indicating continued exponential growth (see Figure 1.1) [2]. This deluge has strained existing storage technologies, exposing limitations in speed, scalability, and energy efficiency. Conventional magnetic switching processes, which achieve rates of approximately one bit per nanosecond, are insufficient to meet the demands of terahertz-scale data transmission in optical networks, which can approach rates of 100 terabytes per second [5]. Efforts to overcome these limitations fueled interest in fundamental studies of spin dynamics triggered in magnets by sub-nanosecond stimuli. Eventually this research direction led to the foundation of a new research field – ultrafast magnetism – which was started by the seminal paper of E. Beaurepaire *et al.* [6], followed by the discovery of ultrafast All-Optical Switching (AOS) [7] and other mechanisms for writing magnetic bits with femto- or picosecond laser pulses [8]. As for now, AOS reverses magnetic states up to fifty times faster than traditional methods while achieving energy efficiencies millions of times greater [3, 9]. An example of AOS from Ref. [3] is shown in Figure 1.2. From the figure, one realizes the greatest disadvantage of AOS. Due to the diffraction limit of light, which restricts laser focusing to areas no smaller than hundreds

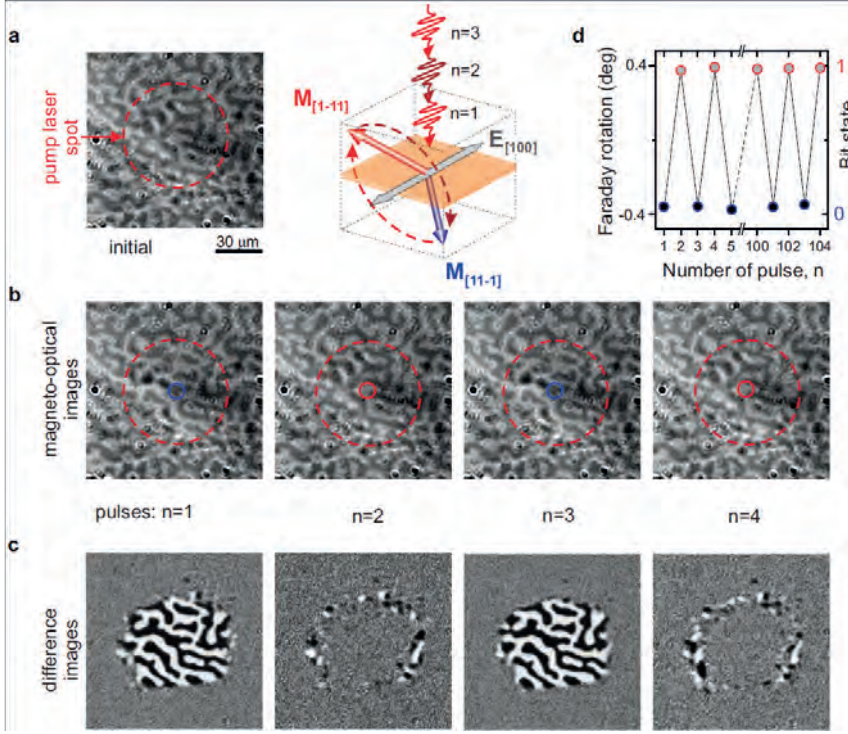


Figure 1.2: All-optical toggle switching of magnetization in Co-substituted iron garnet from Ref. [3]. (a) Magnetic domain pattern, where initially the magnetization can be either in the $[11-1]$ state (black domain) or in the $[1-11]$ state (white domain). Schematic illustration of the magnetic switching between $[11-1]$ and $[1-11]$ in iron garnet (right panel). (b) Magneto-optical images of Co-substituted yttrium iron garnet (YIG:Co) after illumination with a series of pump pulses (c) Differential magneto-optical images obtained as the difference between the images after the n -th and $(n-1)$ -th pump pulses. The images reveal the toggle switching. (d) Changes of the Faraday rotation in the black domain upon excitation by a sequence of laser pulses. Every single pulse changes the magneto-optical effect, suggesting that the magnetization is toggled between two stable bit states. Scale bar for all images is 30 μm .

of nanometers [10, 11] presents a significant barrier to implementing AOS at the

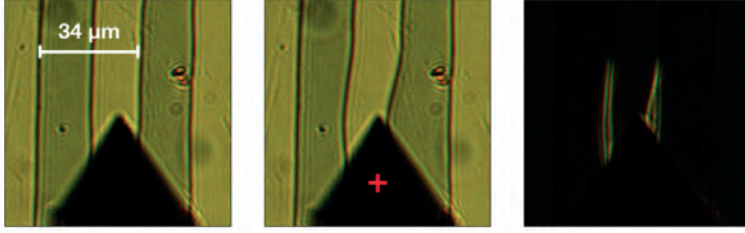


Figure 1.3: Electric-field domain-wall control with a $5\ \mu\text{m}$ tip of a scanning probe microscope: the left figure corresponds to the initial domain structure; the central photograph shows the distortion of the domain structure in the electric field of the tip electrode; the right picture is the result of the image subtraction of the two photographs [13].

nanoscale, where modern magnetic storage devices already achieve bit sizes well below 100 nanometers [12].

In parallel, alternative methods have been explored for high-resolution data manipulation. One promising avenue lies in the magnetoelectric effect, a phenomenon in which electric fields directly influence magnetic order [14–18]. Unlike optical methods, which are constrained by the wavelength of light, magnetoelectric coupling enables precise control of magnetic states at nanometer scales [8, 19, 20]. By leveraging electric fields instead of lasers, spatial resolution becomes defined by the size of the electrodes used to apply the field [8], providing a scalable solution for nanoscale data writing. For instance, one can exploit the inhomogeneous magneto-electric effect by positioning the sharp tip of a scanning-probe microscope just nanometers above a magnetic film. The tip’s highly localized electric field then reconfigures the micromagnetic structure, e.g., magnetic domain walls displacement, as illustrated in Figure 1.3 [13], potentially enabling controlled, energy-efficient writing of magnetic bits at the nanoscale. Without charge current, there is negligible Joule heating, and nearly all input energy drives the local magnetoelectric switch. For a bit volume of $V = 20 \times 20 \times 10\ \text{nm}^3$ in iron garnet under a field $E \sim 100\ \text{MV/m}$ [13, 20], the switching energy can be estimated using the formula for the electric field energy in a dielectric medium [21]:

$$U = \frac{1}{2} \varepsilon_0 \varepsilon_r E^2 V, \quad (1.1)$$

using $\varepsilon_r \approx 12.5$ for yttrium iron garnet [22], the required energy to switch one bit will be about $\sim 2.2\ \text{aJ}$. This is more than 10^9 times lower than in conventional SSDs and HDDs [23, 24]. Since ultrafast AOS alone requires $\sim 26\ \text{aJ}$ for similarly sized bits [9], the localized electric-field assistance could make it even more energy efficient. Moreover, a nanoscale tip confines the field to one bit, leaving neighbors

unaffected.

This intersection of magnetic, optical, and electric technologies highlights a general trend in the development of new physical principles for data storage, where integration of mechanisms allows principles to maintain continuous improvement of data storage. Heat-Assisted Magnetic Recording is the most recent example of the success of such an approach [25].

This thesis is inspired by the idea to merge ultrafast magnetism, which enables picosecond writing of magnetic bits, with magnetoelectric effects that allow the writing of bits at the nanoscale. In this chapter, we briefly review the theoretical foundations of magnetism and magnetoelectric phenomena, as well as theoretical models allowing us to describe light-matter interaction and ultrafast optical control of magnetism.

1.2 Magnetism

Magnetic phenomena form a fundamental pillar of condensed matter physics, emerging from the quantum interactions among atomic magnetic moments. Their impact spans foundational principles and transformative technologies, with magnetic materials playing key roles in data storage, sensing, and energy conversion. Beyond these applications, magnetic phenomena encompass diverse ordering types and dynamic processes that continually expand our understanding of material behavior. The primary magnetic orders, ferromagnetism, ferrimagnetism, and antiferromagnetism, discussed in detail later, are defined by the spatial arrangement and interactions of magnetic moments. Moreover, the interplay between magnetic and electric properties in materials with magnetoelectric coupling offers novel avenues for controlling magnetization.

1.2.1 Magnetism fundamentals

In classical electrodynamics, the circular motion of a charged particle naturally produces a magnetic dipole moment, analogous to a miniature bar magnet. For a localized current density, $\mathbf{j}(\mathbf{r})$, confined within a volume V , the overall magnetic moment is given by

$$\boldsymbol{\mu} = \frac{1}{2} \int_V |\mathbf{r} \times \mathbf{j}(\mathbf{r})| dV. \quad (1.2)$$

When one considers an electron as a classical charged particle with charge e , mass m_e , and velocity \mathbf{v} that moves in a circular orbit, its contribution to the magnetic moment is directly linked to its orbital angular momentum as

$$\boldsymbol{\mu} = \frac{1}{2} \sum_i e_i (\mathbf{r}_i \times \mathbf{v}_i) \quad (1.3)$$

The orbital angular momentum is defined by $\mathbf{L} = m_e (\mathbf{r} \times \mathbf{v})$, so that the corresponding orbital magnetic moment is given by

$$\boldsymbol{\mu}_L = -\frac{e}{2m_e} \mathbf{L}. \quad (1.4)$$

Here, the negative sign reflects the negative charge of the electron.

Beyond the orbital motion, electrons possess an intrinsic angular momentum called spin, \mathbf{S} . Quantum mechanically, the Dirac equation shows that the spin generates its own magnetic moment:

$$\boldsymbol{\mu}_S = -\frac{e}{m_e} \mathbf{S}. \quad (1.5)$$

The total magnetic moment of an electron is the sum of these two contributions:

$$\boldsymbol{\mu} = -\frac{e}{2m_e} (\mathbf{L} + 2\mathbf{S}), \quad (1.6)$$

indicating that, per unit of angular momentum, the spin contribution is twice as effective as the orbital one.

It is standard practice to express the magnetic moment in terms of the reduced Planck constant \hbar and the Bohr magneton, defined as

$$\mu_B = \frac{e\hbar}{2m_e}. \quad (1.7)$$

Thus, the total magnetic moment can be expressed as

$$\boldsymbol{\mu} = -\mu_B \left(\frac{\mathbf{L} + 2\mathbf{S}}{\hbar} \right). \quad (1.8)$$

Such description combining both orbital and spin contributions, forms the basis for understanding magnetic properties from the microscopic to the macroscopic level.

1.2.2 Types of magnetic ordering

Magnetic ordering encompasses diverse phenomena, from the parallel alignment in ferromagnetism to the more complex interactions in ferrimagnetism and anti-ferromagnetism. Each type offers unique properties and applications, serving as the foundation for advanced technologies. The following sections explore these magnetic states.

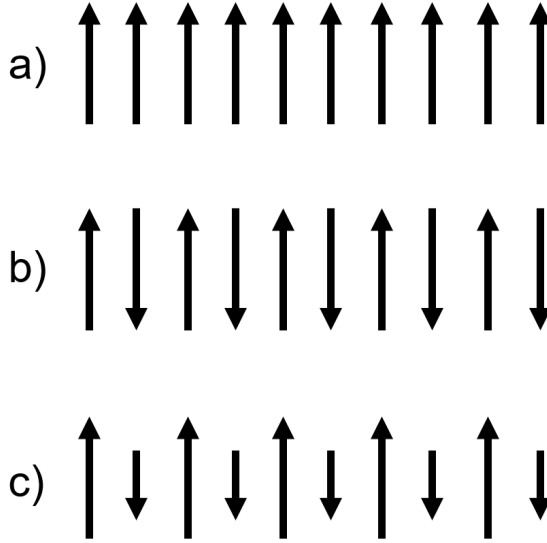


Figure 1.4: Three types of magnetic order, a) ferromagnetic, b) antiferromagnetic, c) ferrimagnetic ordering.

a) Ferromagnetism

Ferromagnetism is the most familiar type of magnetic ordering, found in materials such as iron, cobalt, and nickel. In ferromagnetic materials, atomic magnetic moments align parallel to each other, resulting in a net macroscopic magnetization even in the absence of an external magnetic field (Figure 1.4a) [26]. This alignment arises due to the exchange interaction, a quantum mechanical effect that minimizes the system's energy when moments are parallel. The exchange interaction in ferromagnets is described by the Heisenberg Hamiltonian:

$$H = - \sum_{i,j} J_{ij} \mathbf{S}_i \cdot \mathbf{S}_j \quad (1.9)$$

where J_{ij} is the exchange integral, and \mathbf{S}_i and \mathbf{S}_j are the spin vectors of neighboring atoms. For ferromagnetic materials, $J_{ij} > 0$, favoring parallel alignment of spins. The net magnetization is obtained by summing the contributions of individual spins:

$$\mathbf{M} = \gamma \sum_i \mathbf{S}_i, \quad (1.10)$$

with the gyromagnetic ratio defined as

$$\gamma = \frac{g_S}{2m_e}. \quad (1.11)$$

Here, $g = g_S$ is the spin g-factor, while g_L is the orbital g-factor. As demonstrated in (1.6) or (1.8), their ratio satisfies $g_S/g_L = 2$.

This spontaneous magnetization persists below the material's Curie temperature (T_C). Above T_C , thermal fluctuations overcome the exchange interaction, and the material transitions to a paramagnetic state.

In modern magnetism, however, ferromagnets are rarely described in terms of quantum mechanical spins. Assuming that the exchange interaction is infinitely strong, one can make a transition from individual spins to a macrospin - the net magnetization. This transition forms, in fact, the cornerstone of the thermodynamic approach for the description of magnetic phenomena [27]. Magnets, in this approach, are described in terms of thermodynamic potentials whose terms are expressed in terms of the net magnetization.

For a ferromagnetic thin film with uniaxial perpendicular anisotropy and an external magnetic field applied in the plane (i.e., perpendicular to the easy axis), the simplest thermodynamic potential, including exchange interaction, can be written as

$$\mathcal{F} = A(\nabla\theta)^2 + K_u \sin^2 \theta - \mu_0 M_s H \sin \theta + \frac{1}{2} \mu_0 M_s^2 \cos^2 \theta, \quad (1.12)$$

where A is the exchange constant, K_u is the uniaxial anisotropy constant (with the anisotropy field given by $H_{ani} = [2K_{ani}/M_s]\mathbf{e}_z$, and in our case $K_{ani} = K_u$), θ is the angle between the net magnetization \mathbf{M} and the easy axis, M_s is the saturation magnetization, H is the external magnetic field (applied in-plane, i.e., perpendicular to the easy axis), and μ_0 is the vacuum permeability.

This potential captures the competition between the anisotropy energy, which favors alignment of \mathbf{M} along the easy axis, and the Zeeman energy, which favors alignment with the applied field. The strong and stable magnetization of ferromagnetic materials makes them indispensable in numerous applications, for example, in magnetic data storage devices like hard drives and magnetic tapes, where bits are encoded as magnetized regions [28–30].

As the essence of the net magnetization is angular momentum, spin dynamics in the ferromagnet is described employing the law of conservation of angular momentum [31, 32].

$$\frac{d\mathbf{M}}{dt} = -\gamma \mathbf{M} \times \mathbf{H}_{\text{eff}} + \frac{\alpha}{M_s} \mathbf{M} \times (\mathbf{M} \times \mathbf{H}_{\text{eff}}), \quad (1.13)$$

In this equation, the first term on the right-hand side represents the precessional motion of the magnetization \mathbf{M} around the effective magnetic field \mathbf{H}_{eff} , with the gyromagnetic ratio γ governing the precession frequency. The second term, which

contains the damping parameter α and the saturation magnetization M_s , accounts for the dissipation of energy, ultimately aligning \mathbf{M} with \mathbf{H}_{eff} . This formulation, derived purely from symmetry considerations, captures the essential dynamics of spin systems in ferromagnetic materials. The effective magnetic field \mathbf{H}_{eff} , in this approach, is defined as the derivative of the thermodynamic potential with respect to the magnetization $H_{\text{eff}} = \frac{1}{\mu_0} \partial \mathcal{F} / \partial M$. The equilibrium orientation of the magnetization is defined by minima of the thermodynamic potential, $\partial \mathcal{F} / \partial M = 0$.

b) Antiferromagnetism

Antiferromagnetism is a type of magnetic ordering characterized by the antiparallel alignment of neighboring magnetic moments (Figure 1.4b), resulting in no net macroscopic magnetization. Discovered in the early 20th century [33], antiferromagnetism has since been recognized as a fundamental magnetic state with unique physical properties and applications distinct from those of ferromagnetic and ferrimagnetic materials. In antiferromagnetic materials, the exchange interaction between neighboring spins is negative ($J_{ij} < 0$), favoring antiparallel alignment [26, 34]. This interaction minimizes the system's energy by aligning spins in opposite directions, canceling the net magnetization. Therefore, in order to employ a thermodynamic description of antiferromagnetism and spin dynamics in antiferromagnets, in particular, it is suggested to introduce another order parameter – the antiferromagnetic Néel vector \mathbf{L} . In the simplest case, an antiferromagnet is modeled as two antiferromagnetically coupled ferromagnets with magnetization \mathbf{M}_A and \mathbf{M}_B , respectively. As $\mathbf{M}_A = -\mathbf{M}_B$, the Néel vector, defined as $\mathbf{L} = \mathbf{M}_A - \mathbf{M}_B$, is not zero, while the net magnetization is absent $\mathbf{M}_{\text{net}} = \mathbf{M}_A + \mathbf{M}_B = 0$.

Antiferromagnetic materials exhibit a critical temperature, known as the Néel temperature (T_N), below which the antiparallel spin arrangement is maintained $\mathbf{L} \neq 0$. Above T_N , thermal agitation disrupts the ordering, and the material transitions to a paramagnetic state with $\mathbf{L} = 0$.

c) Ferrimagnetism

Ferrimagnetism is a type of magnetic ordering characterized by the antiparallel alignment of magnetic moments in a material's sublattices, where the magnitudes of these moments are unequal, resulting in a net macroscopic magnetization (Figure 1.4c) [26]. Ferrimagnetic materials combine aspects of both ferromagnetism and antiferromagnetism, making them distinct and versatile in their magnetic properties. The simplest model of two antiferromagnetically coupled ferromagnets with magnetizations \mathbf{M}_A and \mathbf{M}_B , as in the case of pure antiferromagnet described above, can also be applied to ferrimagnets. In this case, $\mathbf{M}_A + \mathbf{M}_B \neq 0$.

The magnetic behavior of ferrimagnets is strongly temperature-dependent, with two critical temperatures:

1. Curie Temperature (T_C): Above this temperature, thermal agitation disrupts the ordered alignment of moments, and the material becomes paramagnetic.
2. Compensation Temperature (T_{comp}): In some ferrimagnets, there exists a temperature at which the magnetizations of the sublattices are exactly equal and opposite, resulting in zero net magnetization.

While ferrimagnetism shares similarities with both ferromagnetism and antiferromagnetism, it is distinct in its net magnetization resulting from unequal opposing moments. Unlike antiferromagnets, which exhibit no macroscopic magnetization, ferrimagnets can be magnetized, and their properties are more easily tunable than those of simple ferromagnets. Far from the compensation temperature, ferrimagnets can be described as ferromagnets with a net magnetization $\mathbf{M}_A + \mathbf{M}_B$.

1.2.3 Magneto-electric effects

The phenomenon of magnetoelectric (ME) coupling, where magnetic and electric properties influence one another, has intrigued scientists for over a century. The concept was first hinted at by Pierre Curie in 1894, who suggested the symmetry constraints required for such coupling in materials [35]. However, it was not until the mid-20th century that these effects were formally predicted by Dzyaloshinskii in 1959 [36] and subsequently observed experimentally by Astrov in Cr_2O_3 [37]. This groundbreaking discovery laid the foundation for a new field of study, merging magnetism and electricity into a unified framework. Early research on magnetoelectricity was largely driven by the pursuit of fundamental physical principles; however, practical applications were initially limited by the intrinsic weakness of the ME coupling in naturally occurring materials. The resurgence of interest in magnetoelectricity in the late 20th century was fueled by advancements in material science and nanotechnology. The discovery of multiferroics, materials exhibiting simultaneous ferroelectricity and magnetism, opened new pathways for realizing stronger ME coupling. Composite materials, combining ferroelectric and magnetic phases, further expanded the possibilities by leveraging interfacial strain and charge effects to enhance coupling efficiency.

a) Linear magnetoelectric effect

The linear ME effect is one of the most important phenomena in the field of magnetoelectricity, representing the simplest and most fundamental form of coupling between electric and magnetic fields in a material. It describes a linear relationship where an applied electric field induces a magnetization, or an applied magnetic field

generates an electric polarization. This coupling can be expressed mathematically as:

$$P_i = \alpha_{ij}H_j \text{ and } M_i = \alpha_{ij}E_j \quad (1.14)$$

where P_i is the electric polarization, H_j is the magnetic field, M_i is the magnetization, E_j is the electric field, and α_{ij} is the linear magnetoelectric tensor. The indices i and j denote the Cartesian components, and the tensor α_{ij} determines the strength and symmetry of the coupling.

The occurrence of the linear ME effect is governed by the symmetry properties of the material. A material must break both inversion symmetry (to permit electric polarization) and time-reversal symmetry (to allow magnetization) to exhibit this effect [38]. As a result, the magnetoelectric tensor α_{ij} is highly anisotropic and constrained by the symmetry group of the studied material. For example, Cr_2O_3 exhibits a diagonal α_{ij} tensor with nonzero components along the principal axes due to its antiferromagnetic structure and specific crystal symmetry. Other materials, such as rare-earth orthoferrites (e.g., DyFeO_3 [39]) and rare-earth iron garnets (e.g., yttrium iron garnet [40]), have also demonstrated linear ME coupling. The linear ME effect is described thermodynamically by adding a cross-term to the free energy:

$$\mathcal{F} = \mathcal{F}_0 - P_i E_i - \mu_0 M_i H_i - \frac{1}{2} \alpha_{ij} E_i H_j, \quad (1.15)$$

where \mathcal{F}_0 is the unperturbed free energy. The last term, α_{ij} , captures the coupling between electric and magnetic fields. For every particular case, polarization and magnetization of a magnetoelectric material can be found by minimization of this free energy. Once the potential is minimized, polarization and magnetization can be found from the relationships $P_i = -\partial\mathcal{F}/\partial E_i$ and $\mu_0 M_i = -\partial\mathcal{F}/\partial H_i$, recovering the linear expressions for P_i and M_i .

b) Quadratic magnetoelectric effect

In addition to the linear ME effect, some materials exhibit a quadratic response, where the induced polarization or magnetization depends on the square of the applied field [18, 41–44]. Unlike the linear case, described by the first-order tensor α_{ij} , the quadratic effect involves higher-order contributions. For example, the induced polarization may include a term

$$P_i^{(2)} = \beta_{ijk} H_j H_k, \quad (1.16)$$

and similarly, the induced magnetization can be written as

$$M_i^{(2)} = \gamma_{ijk} E_j E_k, \quad (1.17)$$

where β_{ijk} and γ_{ijk} are third-rank tensors characterizing the quadratic coupling [41, 42]. This quadratic dependence implies that even in systems where the linear ME effect is symmetry-forbidden, a nonzero ME response can emerge from quadratic interactions. This is particularly important in high-symmetry materials or in those engineered to enhance second-order responses, offering alternative routes for controlling magnetic states via electric fields.

The quadratic ME effect can be incorporated into the thermodynamic potential by extending the free energy expansion to include quadratic field terms. In one approach, the free energy is expressed as

$$\mathcal{F} = \mathcal{F}_0 - P_i E_i - \mu_0 M_i H_i - \frac{1}{2} \alpha_{ij} E_i H_j - \frac{1}{2} \beta_{ijk} E_i H_j H_k, \quad (1.18)$$

or, alternatively, if the quadratic coupling involves two electric fields under a magnetic field,

$$\mathcal{F} = \mathcal{F}_0 - P_i E_i - \mu_0 M_i H_i - \frac{1}{2} \alpha_{ij} E_i H_j - \frac{1}{2} \gamma_{ijk} E_i E_j H_k, \quad (1.19)$$

Minimizing the free energy with respect to E_i and H_i yields additional contributions to the induced polarization and magnetization $P_i = -\partial\mathcal{F}/\partial E_i = P_i^{(\text{linear})} + \frac{1}{2} \beta_{ijk} H_j H_k$ and $M_i = -\partial\mathcal{F}/\partial H_i = M_i^{(\text{linear})} + \frac{1}{2} \gamma_{ijk} E_j E_k$. These quadratic terms represent the nonlinear response of the material and provide a thermodynamic framework for understanding and quantifying the quadratic ME effect.

c) Inhomogeneous magneto-electric effect

Among ME phenomena, the inhomogeneous magnetoelectric (IME) effect stands out as particularly captivating; it was theoretically predicted by Baryakhtar in 1983 [45] and later experimentally observed in 2007 [46].

The IME effect refers to the coupling between electric polarization and the spatial gradients of the magnetization [47]. This interaction is analogous to the flexoelectric effect [48] in dielectrics, where a strain gradient induces polarization, but here the role of the strain gradient is played by a nonuniform magnetic order.

In magnetically ordered media with spatially modulated spin structures (such as cycloids), the local breaking of inversion symmetry allows an electric polarization to be induced directly by the magnetic structure. In the isotropic case, the IME energy can be expressed as

$$\mathcal{F}_{\text{inh. ME}} = \gamma \mathbf{P} \cdot (\mathbf{m} (\nabla \cdot \mathbf{m}) + \mathbf{m} \times (\nabla \times \mathbf{m})), \quad (1.20)$$

where γ is the flexo-magnetoelectric coupling constant and \mathbf{m} is the unit magnetization vector. For crystals with a high symmetry axis (e.g., tetragonal or hexagonal

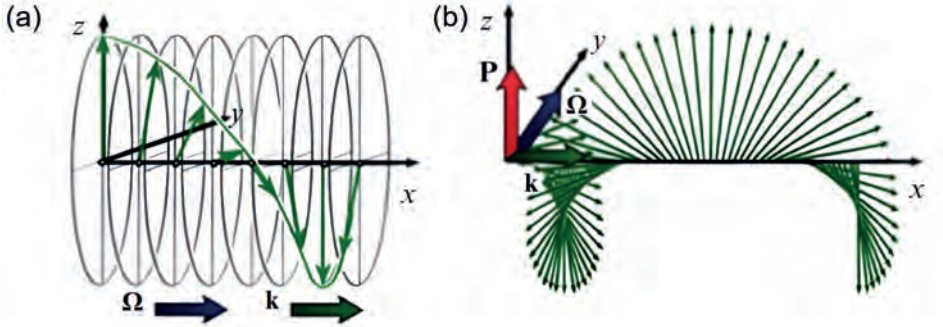


Figure 1.5: Spatially modulated spin structures in magnetic media. (a) Spin helicoide: the magnetization vector \mathbf{m} (green arrows) rotates around the propagation vector \mathbf{k} , yielding no net polarization ($\mathbf{P} = 0$). The rotation takes place in planes parallel to the yz -plane, marked by grey circles. (b) Spin cycloid: \mathbf{m} (green arrows) rotates within the plane defined by \mathbf{k} . Moving along \mathbf{k} , the orientation of \mathbf{m} changes continuously, forming a cycloidal profile and generating a net polarization $\mathbf{P} \propto \mathbf{k} \times \mathbf{\Omega}$, where $\mathbf{\Omega}$ is the normal to the rotation plane (see Eq. 1.25) [47].

systems) with the z -axis as the principal direction, the invariant is often simplified to

$$\mathcal{F}_{\text{inh.ME}} = \gamma P_z \left(m_z \frac{\partial m_x}{\partial x} - m_x \frac{\partial m_z}{\partial x} \right). \quad (1.21)$$

Using the expression from (1.21) and representing the magnetization unit vector in spherical coordinates, we write

$$\mathbf{m} = (\sin \theta \cos \phi, \sin \theta \sin \phi, \cos \theta). \quad (1.22)$$

The IME free energy is then given by

$$\mathcal{F}_{\text{inh.ME}} = \gamma P_z \frac{\partial \theta}{\partial \xi}, \quad (1.23)$$

where ξ is the coordinate along the modulation direction. Alternatively, the free energy can be expressed as

$$\mathcal{F} = \gamma \mathbf{P} \cdot (\mathbf{k} \times \mathbf{\Omega}), \quad (1.24)$$

with \mathbf{k} representing the wave vector of the spatially modulated spin structure and $\mathbf{\Omega}$ the normal to the plane of magnetization rotation. In spatially modulated structures, the electric polarization is determined by the cross product of \mathbf{k} and $\mathbf{\Omega}$ [49]:

$$\mathbf{P} = -\frac{\partial \mathcal{F}_{\text{inh.ME}}}{\partial \mathbf{E}} = \gamma \chi_e \mathbf{k} \times \mathbf{\Omega}, \quad (1.25)$$

where χ_e denotes the electric polarizability. This expression implies that for a helicoïd (see Figure 1.5a), where the normal $\mathbf{\Omega}$ does not define a unique polar direction, the net electric polarization vanishes. In contrast, the polarization is maximized for a spin cycloid (see Figure 1.5b), and reversing the direction of magnetization rotation ($\mathbf{\Omega} \rightarrow -\mathbf{\Omega}$) reverses the polarization ($\mathbf{P} \rightarrow -\mathbf{P}$).

Thus, the IME provides a mechanism whereby nonuniform spin structures directly induce an electric polarization. This coupling not only enriches the phenomenology of multiferroics but also opens new avenues for electric-field control of magnetic textures that we discuss in the following chapters, paving the way for innovative applications in information storage and spintronics.

1.3 Ultrafast control over magnetization

Ultrafast magnetism is a rapidly evolving field at the interface of condensed matter physics and laser-matter interactions, focusing on manipulating magnetic properties on femtosecond (10^{-15} s) to picosecond (10^{-12} s) timescales. Ultrashort laser-induced heating can cause an ultrafast demagnetization [6] or an ultrafast change of magnetic anisotropy [50]. Polarized light can affect the magnetization as an effective magnetic field via the inverse Faraday effect [51] or inverse Cotton-Mouton effect [52]. Pumping specific electronic transitions can also affect interactions experienced by spins of ions in magnets [53, 54], change magnetic anisotropy [55], and even activate magnetoelectricity [56]. Ultrafast laser excitation can even trigger a switching of magnetization between stable states and thus write magnetic information [7]. Various mechanisms of magnetic writing with the help of light have so far been demonstrated, but the heat-assisted precessional mechanism seems to be the most universal of them and could be realized in a large class of metallic [7], semiconducting [57] or dielectric ferro- [58] and ferrimagnets [59, 60].

In this approach, a focused ultrashort laser pulse delivers a controlled thermal load to a dielectric magnetic medium, transiently modifying its magnetocrystalline anisotropy due to temperature changes. The laser pulse raises the material temperature to near (or even above) a threshold at which the anisotropy field $H_{\text{ani}}(T)$ is significantly reduced, while the magnetization $M(T)$ remains relatively stable. For example, in the iron garnet studied in Ref. [59], raising the temperature from 300 K to 330 K reduces H_{ani} by roughly 45%, while M decreases by only about 10% (see Figure 1.6). This pronounced difference in thermal sensitivity creates

a transient effective torque on the magnetization vector when an in-plane bias magnetic field H_B is applied.

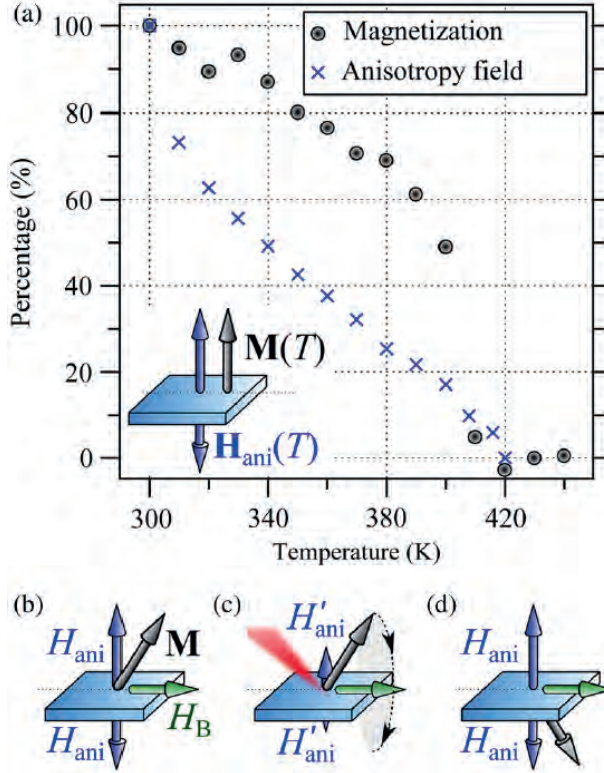


Figure 1.6: (a) Static temperature dependence of the out-of-plane magnetocrystalline anisotropy field H_{ani} and magnetization M for bismuth-substituted yttrium iron garnet. (b) In the ground state, M aligns parallel to the effective magnetic field – a combination of H_{ani} and the in-plane bias field H_B . (c) A thermal load transiently reduces the anisotropy field to H'_{ani} , triggering large-amplitude precession of M about a new effective field primarily determined by H_B . (d) After thermal dissipation and precession, H_{ani} recovers, stabilizing the switched magnetization state [59].

Experimental pump-probe measurements corroborate this mechanism: when the laser fluence is sufficiently high to transiently quench the anisotropy field, the magnetization reverses deterministically-independent of the optical polarization

state of the pulse. These observations confirm that the ultrafast thermal modification of the anisotropy field alone can drive magnetization reversal, thereby paving the way for heat-assisted magnetic recording in dielectric media.

This heat-assisted precessional mechanism, enabled solely by the thermal energy delivered by ultrashort optical pulses, offers a promising pathway to sub-nanosecond/picosecond switching [9, 61] – an essential requirement for next-generation spintronic and magnetic memory devices. This switching speed is about three orders of magnitude faster than information writing in conventional data storage devices working at nanosecond timescales. The obvious drawback of the optical control of magnetism is the spatial resolution of the technique, which is limited by the size of the focused laser beam and thus cannot be much smaller than the laser wavelength. Aiming to combine the advantages of the nanoscalable electric field control of magnetization via the magneto-electric effect and the ultrafast writing with the help of light, it is interesting to explore peculiarities of light-matter interaction in magneto-electric materials. This is exactly the focus of this thesis.

1.4 Scope of the thesis

This thesis investigates ultrafast magnetism and magnetoelectric phenomena in complex oxide materials using advanced optical, electrical, and magneto-optical techniques. The goal of this work is to explore novel pathways for controlling spin dynamics and magnetic states on ultrafast timescales, with potential applications in energy-efficient spintronic and magnetic memory devices. In particular, the work focuses on:

- **Experimental Methodologies:** (Chapter 2) A comprehensive suite of techniques is developed and applied, including optical pump–probe spectroscopy, spatially resolved magneto–optical imaging, electrical gating, and second harmonic generation. These methods enable probing of ultrafast lattice and spin dynamics as well as magnetoelectric interactions with femtosecond to picosecond resolution.
- **Inhomogeneous Spin Dynamics in Iron Garnets:** (Chapter 3) Using ultrafast imaging, the work reveals strongly inhomogeneous spin dynamics in epitaxial films of iron garnet excited by laser pulses with Gaussian intensity profiles. This study highlights how local variations in thermal load and anisotropy lead to complex spatial patterns in magnetization, a phenomenon that could be overlooked in conventional pump–probe experiments.
- **Electrical Control of Ultrafast Spin Dynamics:** (Chapter 4) The chapter demonstrates that an externally applied electric field can significantly modulate the efficiency of light–spin coupling in magnetoelectric iron garnet at room temperature. By integrating electrical gating with ultrafast optical excitation, coherent spin waves are launched and their dynamics controlled with electric fields orders of magnitude lower than those required in 2D magnetic semiconductors.
- **Electric Field Manipulation of Antiferromagnetic Domain Walls:** (Chapter 5) The study explores electric-field-driven motion of antiferromagnetic domain walls in Cr_2O_3 thin films. The experiments reveal that a localized electric field can attract or repel domain walls via robust linear magnetoelectric coupling, providing insights into potential low-energy approaches for controlling magnetic domain structures in antiferromagnets.
- **Resonant Optical Excitation in Rare-Earth Perovskites:** (Chapter 6) The chapter examines the optical excitation of coherent THz lattice dynamics in a complex perovskite (DyFeO_3). The material is known for its record-strong magneto-electric effect [39]. Resonant pumping of f – f electronic transitions in Dy^{3+} ions is employed to drive Raman-active phonon

modes selectively, elucidating the coupling between electronic and lattice degrees of freedom in rare-earth orthoferrites.

- This thesis concludes with a summary of the findings and a discussion of potential directions for future research.

References

- [1] IBM. Ramac. <https://www.ibm.com/history/ramac>, n.d. Accessed: 26 March 2025.
- [2] Statista. Worldwide data created. <https://www.statista.com/statistics/871513/worldwide-data-created/>, n.d. Accessed: 26 March 2025.
- [3] T Zalewski, A Maziewski, AV Kimel, and A Stupakiewicz. Ultrafast all-optical toggle writing of magnetic bits without relying on heat. *Nature Communications*, 15(1):4451, 2024.
- [4] Laith Alzubaidi, Jinglan Zhang, Amjad J Humaidi, Ayad Al-Dujaili, Ye Duan, Omran Al-Shamma, José Santamaría, Mohammed A Fadhel, Muthana Al-Amidie, and Laith Farhan. Review of deep learning: concepts, cnn architectures, challenges, applications, future directions. *Journal of big Data*, 8:1–74, 2021.
- [5] Abhishek Bhattacharjee and Ajay Kumar Badhan. Convergence of data analytics, big data, and machine learning: applications, challenges, and future direction. In *Data analytics and machine learning: navigating the big data landscape*, pages 317–334. Springer, 2024.
- [6] Eric Beaurepaire, J-C Merle, A Daunois, and J-Y Bigot. Ultrafast spin dynamics in ferromagnetic nickel. *Physical review letters*, 76(22):4250, 1996.
- [7] Claudiu D Stanciu, Fredrik Hansteen, Alexey V Kimel, Andrei Kirilyuk, Arata Tsukamoto, Achioshi Itoh, and Th Rasing. All-optical magnetic recording with circularly polarized light. *Physical review letters*, 99(4):047601, 2007.
- [8] Alexey V Kimel and Mo Li. Writing magnetic memory with ultrashort light pulses. *Nature Reviews Materials*, 4(3):189–200, 2019.
- [9] A Stupakiewicz, K Szerenos, D Afanasiev, A Kirilyuk, and AV Kimel. Ultrafast nonthermal photo-magnetic recording in a transparent medium. *Nature*, 542(7639):71–74, 2017.
- [10] Ernst Abbe. Beiträge zur theorie des mikroskops und der mikroskopischen wahrnehmung. *Archiv für mikroskopische Anatomie*, 9(1):413–468, 1873.
- [11] Ernst HK Stelzer and S Grill. The uncertainty principle applied to estimate focal spot dimensions. *Optics communications*, 173(1-6):51–56, 2000.
- [12] Joel KW Yang, Yunjie Chen, Tianli Huang, Huigao Duan, Naganivetha Thiagarajah, Hui Kim Hui, Siang Huei Leong, and Vivian Ng. Fabrication and characterization of bit-patterned media beyond 1.5 tbit/in². *Nanotechnology*, 22(38):385301, 2011.

-
- [13] RM Vakhitov, RV Solonetsky, VR Gurjanova, AR Nizjamova, DA Sechin, TT Gareev, and AP Pyatakov. Magnetic-field tuning of domain-wall multiferroicity. *Physical Review B*, 104(14):144407, 2021.
 - [14] TH O’dell. An induced magneto-electric effect in yttrium iron garnet. *Philosophical Magazine*, 16(141):487–494, 1967.
 - [15] Manfred Fiebig. Revival of the magnetoelectric effect. *Journal of physics D: applied physics*, 38(8):R123, 2005.
 - [16] Nicola A Spaldin and Manfred Fiebig. The renaissance of magnetoelectric multiferroics. *Science*, 309(5733):391–392, 2005.
 - [17] Maxim Mostovoy. Multiferroics: Different routes to magnetoelectric coupling. *npj Spintronics*, 2(1):18, 2024.
 - [18] Anatolii K Zvezdin and Aleksandr P Pyatakov. Phase transitions and the giant magnetoelectric effect in multiferroics. *Physics-Uspekhi*, 47(4):416, 2004.
 - [19] Nikolai E Khokhlov, Anastasiya E Khramova, Elena P Nikolaeva, Tatyana B Kosykh, Alexey V Nikolaev, Anatoly K Zvezdin, Alexander P Pyatakov, and Vladimir I Belotelov. Electric-field-driven magnetic domain wall as a microscale magneto-optical shutter. *Scientific Reports*, 7(1):264, 2017.
 - [20] AP Pyatakov, TT Gareev, AS Kaminskiy, KS Antipin, EP Nikolaeva, DP Kulikova, AS Sergeev, and AV Nikolaev. Magnetoelectricity of chiral micromagnetic structures. *Chirality, Magnetism and Magnetoelectricity: Separate Phenomena and Joint Effects in Metamaterial Structures*, pages 127–146, 2021.
 - [21] David J Griffiths. *Introduction to electrodynamics*. Cambridge University Press, 2023.
 - [22] Lalitha Sirdeshmukh, K Krishna Kumar, S Bal Laxman, A Rama Krishna, and G Sathaiah. Dielectric properties and electrical conduction in yttrium iron garnet (yig). *Bulletin of Materials Science*, 21:219–226, 1998.
 - [23] J Ping Liu, Eric Fullerton, Oliver Gutfleisch, and David J Sellmyer. *Nanoscale magnetic materials and applications*. Springer, 2009.
 - [24] Anthony Hylick, Ripduman Sohan, Andrew Rice, and Brian Jones. An analysis of hard drive energy consumption. In *2008 IEEE International Symposium on Modeling, Analysis and Simulation of Computers and Telecommunication Systems*, pages 1–10. IEEE, 2008.
 - [25] Seagate Technology LLC. Heat-assisted magnetic recording (hamr) technology paper. Technical Paper TP707.1-1712US, Seagate Technology LLC, 2017. Accessed: 2025-05-23.

- [26] John MD Coey. *Magnetism and magnetic materials*. Cambridge university press, 2010.
- [27] Lev Davidovich Landau, John Stewart Bell, MJ Kearsley, LP Pitaevskii, EM Lifshitz, and JB Sykes. *Electrodynamics of continuous media*, volume 8. elsevier, 2013.
- [28] R Lawrence Comstock. Review modern magnetic materials in data storage. *Journal of Materials Science: Materials in Electronics*, 13:509–523, 2002.
- [29] Bharat Bhushan. *Tribology and mechanics of magnetic storage devices*. Springer Science & Business Media, 2012.
- [30] Bharat Bhushan. Current status and outlook of magnetic data storage devices. *Microsystem Technologies*, 29(11):1529–1546, 2023.
- [31] LALE Landau and Evgeny Lifshitz. On the theory of the dispersion of magnetic permeability in ferromagnetic bodies. *Phys. Z. Sowjetunion*, 8(153):101–114, 1935.
- [32] Thomas L Gilbert. A lagrangian formulation of the gyromagnetic equation of the magnetization field. *Phys. Rev.*, 100:1243, 1955.
- [33] Louis Néel. Influence des fluctuations du champ moléculaire sur les propriétés magnétiques des corps. In *Annales de physique*, volume 17, pages 5–105, 1932.
- [34] Louis Néel. Some new results on antiferromagnetism and ferromagnetism. *Reviews of Modern Physics*, 25(1):58, 1953.
- [35] Pierre Curie. Sur la symétrie dans les phénomènes physiques, symétrie d’un champ électrique et d’un champ magnétique. *Journal de physique théorique et appliquée*, 3(1):393–415, 1894.
- [36] IE Dzyaloshinskii. On the magneto-electrical effect in antiferromagnets. *J. Exp. Theor. Phys*, 37:881–882, 1959.
- [37] DN Astrov. The magnetoelectric effect in antiferromagnetics. *Sov. Phys. JETP*, 11(3):708–709, 1960.
- [38] Robert R Birss. Symmetry and magnetism. 1964.
- [39] Y Tokunaga, S Iguchi, T-h Arima, and Y Tokura. Magnetic-field-induced ferroelectric state in dyfe0 3. *Physical review letters*, 101(9):097205, 2008.
- [40] BB Krichevtsov, VV Pavlov, RV Pisarev, and AG Selitsky. Linear magnetoelectric effect in magnetic garnet thin films. *Ferroelectrics*, 161(1):65–71, 1994.

- [41] Edgar Ascher. Higher-order magneto-electric effects. *The Philosophical Magazine: A Journal of Theoretical Experimental and Applied Physics*, 17(145):149–157, 1968.
- [42] Hans Schmid. On a magnetoelectric classification of materials. *Int. J. Magn*, 4(337-361):2, 1973.
- [43] Cristobal Tabares-Munoz, J-P Rivera, A Bezinges, Alain Monnier, and Hans Schmid. Measurement of the quadratic magnetoelectric effect on single crystalline bifeo₃. *Japanese Journal of Applied Physics*, 24(S2):1051, 1985.
- [44] J-P Rivera. A short review of the magnetoelectric effect and related experimental techniques on single phase (multi-) ferroics. *The European Physical Journal B*, 71:299–313, 2009.
- [45] VG Bar’Yakhtar, VA L’vov, and DA Yablonskiĭ. Inhomogeneous magneto-electric effect. *ZhETF Pisma Redaktsiiu*, 37:565, 1983.
- [46] Aleksandr Sergeevich Logginov, Georgy Aleksandrovich Meshkov, Alexey Vladimirovich Nikolaev, and Aleksandr Pavlovich Pyatakov. Magnetoelectric control of domain walls in a ferrite garnet film. *JETP Letters*, 86:115–118, 2007.
- [47] Aleksandr P Pyatakov and Anatolii K Zvezdin. Magnetoelectric and multi-ferroic media. *Physics-Uspekhi*, 55(6):557, 2012.
- [48] AK Tagantsev. Pyroelectricity, piezoelectricity, flexoelectricity and thermopolarization effects in ionic-crystals. *Uspekhi Fizicheskikh Nauk*, 152(3):423–448, 1987.
- [49] Maxim Mostovoy. Ferroelectricity in spiral magnets. *Physical review letters*, 96(6):067601, 2006.
- [50] J-Y Bigot, M Vomir, LHF Andrade, and E Beaurepaire. Ultrafast magnetization dynamics in ferromagnetic cobalt: The role of the anisotropy. *Chemical physics*, 318(1-2):137–146, 2005.
- [51] AV Kimel, A Kirilyuk, PA Usachev, RV Pisarev, AM Balbashov, and Th Rasing. Ultrafast non-thermal control of magnetization by instantaneous photomagnetic pulses. *Nature*, 435(7042):655–657, 2005.
- [52] Aleksandra Mikhailovna Kalashnikova, A Vol’demarovich Kimel, and Roman Vasilievich Pisarev. Ultrafast opto-magnetism. *Physics-Uspekhi*, 58(10):969, 2015.
- [53] TT Gareev, Alireza Sasani, DI Khusyainov, Eric Bousquet, ZV Gareeva, AV Kimel, and D Afanasiev. Optical excitation of coherent thz dynamics of the rare-earth lattice through resonant pumping of f-f electronic transition

- in a complex perovskite dyfeo 3. *Physical Review Letters*, 133(24):246901, 2024.
- [54] Dinar Khusyainov, Timur Gareev, Viktoriia Radovskaia, Krishna Sampathkumar, Swagata Acharya, Makars Šiškins, Samuel Mañas-Valero, Boris A Ivanov, E Coronado, Th Rasing, et al. Ultrafast laser-induced spin-lattice dynamics in the van der waals antiferromagnet cops3. *APL Materials*, 11(7), 2023.
 - [55] Dmytro Afanasiev, Jorrit R Hortensius, Mattias Matthiesen, Samuel Mañas-Valero, Makars Šiškins, Martin Lee, Edouard Lesne, Herre SJ van Der Zant, Peter G Steeneken, Boris A Ivanov, et al. Controlling the anisotropy of a van der waals antiferromagnet with light. *Science advances*, 7(23):eabf3096, 2021.
 - [56] Davide Bossini, Kuniaki Konishi, Singo Toyoda, Taka-hisa Arima, Junji Yumoto, and Makoto Kuwata-Gonokami. Femtosecond activation of magneto-electricity. *Nature Physics*, 14(4):370–374, 2018.
 - [57] Freddie Hendriks, Rafael R Rojas-Lopez, Bert Koopmans, and Marcos HD Guimarães. Electric control of optically-induced magnetization dynamics in a van der waals ferromagnetic semiconductor. *Nature Communications*, 15(1):1298, 2024.
 - [58] Charles-Henri Lambert, Stéphane Mangin, BSD Ch S Varaprasad, YK Takahashi, Michel Hehn, M Cinchetti, Grégory Malinowski, K Hono, Y Fainman, M Aeschlimann, et al. All-optical control of ferromagnetic thin films and nanostructures. *Science*, 345(6202):1337–1340, 2014.
 - [59] CS Davies, KH Prabhakara, MD Davydova, KA Zvezdin, TB Shapaeva, Sicong Wang, AK Zvezdin, Andrei Kirilyuk, Th Rasing, and AV Kimel. Anomalous damped heat-assisted route for precessional magnetization reversal in an iron garnet. *Physical review letters*, 122(2):027202, 2019.
 - [60] A Dolgikh, D Afanasiev, VV Yurlov, MV Logunov, AK Zvezdin, and AV Kimel. Ultrafast heat-assisted magnetization dynamics in a ferrimagnetic insulator. *Physical Review B*, 107(9):094424, 2023.
 - [61] Th Gerrits, HAM Van Den Berg, J Hohlfeld, L Bär, and Th Rasing. Ultrafast precessional magnetization reversal by picosecond magnetic field pulse shaping. *Nature*, 418(6897):509–512, 2002.

Chapter 2

Experimental Methods

This chapter presents an overview of the experimental methods used to investigate the magnetization and phonon dynamics initiated in media by ultrashort laser pulses, electric fields, and combinations thereof. The techniques include optical pump–probe spectroscopy, spatially resolved magneto-optical imaging of domains in ferro- and ferrimagnets, electrical gating, and second harmonic generation (SHG) for imaging antiferromagnetic domains.

2.1 Introduction

This chapter outlines the experimental setups and methodologies employed to probe ultrafast dynamics in complex materials. The chapter is organized as follows. First, we review the fundamentals of light-matter interaction. It is shown how light can be sensitive to the lattice dynamics in crystals and spin dynamics in ferro-, ferri-, and antiferromagnets. More particularly, using phenomenological theory, we show how optical properties depend on the magnetization of a magnet, leading to the magneto-optical Faraday effect, in particular. We further expand the topic by showing that even in the case of an antiferromagnet with no net magnetization, the magnetic order parameter – the antiferromagnetic Néel vector – can be visualized using nonlinear optical techniques and the method of the Second Harmonic Generation (SHG), in particular. Finally, we provide the details of the configurations of the setups used in the experiments.

2.2 Light–matter interaction

Understanding how light interacts with matter is fundamental to modern optics. In this section, we describe a unified approach that includes both linear and nonlinear responses of a material.

2.2.1 Linear optical response from a thermodynamic perspective

Under the electric dipole and continuous medium approximations, the interaction of light with matter is dominated by the coupling between the oscillating electric field and the induced electric dipoles. In the linear optical regime, the specific thermodynamic potential (i.e., the internal energy per unit volume) in the presence of light can be written as

$$U = U_0 + \frac{1}{2} \varepsilon_0 \varepsilon_{ij} E_i^* E_j, \quad (2.1)$$

where U_0 is the field-independent energy, ε_0 the vacuum permittivity, $E_{i,j}$ the components of the electric field, and ε_{ij} the dielectric permittivity tensor.

Since the medium's response is linear, the dielectric permittivity is obtained from the second derivative of U with respect to the electric field:

$$\varepsilon_{ij} = \frac{2}{\varepsilon_0} \frac{\partial^2 U}{\partial E_i^* \partial E_j}. \quad (2.2)$$

For a non-dissipative system, ε_{ij} is Hermitian [1] (i.e., $\varepsilon_{ij} = \varepsilon_{ji}^*$), and we can represent it as a sum of symmetric (s) and antisymmetric (a) matrices:

$$\varepsilon_{ij} = \varepsilon_{ij}^{(s)} + \varepsilon_{ij}^{(a)}, \quad (2.3)$$

with

$$\varepsilon_{ij}^{(s)} = \varepsilon_{ji}^{(s)} \quad \text{and} \quad \varepsilon_{ij}^{(a)} = -\varepsilon_{ji}^{(a)}. \quad (2.4)$$

The antisymmetric component is responsible for circular birefringence and magneto-optical effects such as the Faraday rotation [2].

In magnetically ordered materials, the optical response may also depend on internal magnetic variables. For example, in ferromagnets the antisymmetric part may depend linearly on the magnetization \mathbf{M} [3]:

$$\varepsilon_{ij}^{(a)}(M) = \chi_{ijl}^{(M)} M_l + \dots, \quad (2.5)$$

where $\chi_{ijl}^{(M)}$ is a phenomenological tensor. In antiferromagnets the Néel vector \mathbf{L} enters the dielectric response quadratically [3]:

$$\varepsilon_{ij}^{(s)}(L) = \varepsilon_{ij}^{(0)} + \chi_{ijln}^{(L)} L_l L_n + \dots \quad (2.6)$$

where $\varepsilon_{ij}^{(0)}$ is the part of dielectric permittivity that does not depend on \mathbf{M} or \mathbf{L} , $\chi_{ijln}^{(L)}$ is a phenomenological tensor.

The quadratic dependence in antiferromagnets suggests that their optical response cannot be fully captured by a linear framework. To probe the inherent nonlinearities arising from the quadratic dependence on \mathbf{L} , higher-order generation processes, such as second harmonic generation, become essential. We will discuss these processes and how they can be used, e.g., for antiferromagnetic domains visualization, in detail in the following sections.

2.2.2 Second harmonic generation fundamentals

Second harmonic generation (SHG) is a nonlinear optical process where two photons at a fundamental frequency ω are effectively combined within a non-centrosymmetric medium to produce a photon at twice the frequency (2ω). To understand this process, one can model the interaction using an ensemble of oscillators with a resonant frequency ω_0 . In the electric-dipole approximation, the motion of an oscillator under the influence of an electric field $E(t)$ is governed by

$$m \frac{d^2 x}{dt^2} + m \omega_0^2 x = q E(t), \quad (2.7)$$

with the driving field typically expressed as

$$E(t) = E(\omega)e^{i\omega t} + E^*(\omega)e^{-i\omega t}. \quad (2.8)$$

Under linear conditions, where the restoring force is simply $F(x) = kx$ (with $k = m\omega_0^2$), the oscillator responds at the same frequency as the excitation. However, if an anharmonic term is introduced into the potential energy, such as

$$W(x) = \frac{1}{2}kx^2 + \frac{\eta}{3}x^3, \quad (2.9)$$

the equation of motion is modified to

$$m \frac{d^2x}{dt^2} + m\omega_0^2x + \eta x^2 = qE(t). \quad (2.10)$$

The anharmonic coefficient η drives a nonlinear response, which, when the system is excited by a monochromatic wave, results in additional oscillatory components. Specifically, the nonlinear displacement can be expressed as

$$x_{\text{nl}}(t) = x(0) + x(2\omega)e^{i2\omega t}, \quad (2.11)$$

indicating that, besides the linear response at ω , the system also oscillates at 2ω . This behavior manifests itself in the induced nonlinear polarization:

$$P_{\text{nl}}(t) = P(0) + P(2\omega)e^{i2\omega t}. \quad (2.12)$$

Thus, a medium excited at frequency ω not only re-emits light at the same frequency but also generates light at 2ω .

A thermodynamic approach further clarifies this interaction. The internal energy of the medium in the presence of light can be expressed as

$$U = U_0 + \frac{1}{2}\varepsilon_0\varepsilon_{ij}E_i^*(\omega)E_j(\omega) + \chi_{ijk}E_i^*(2\omega)E_j(\omega)E_k(\omega), \quad (2.13)$$

where U_0 is the internal energy without light, and χ_{ijk} is a polar third-rank tensor representing the nonlinear susceptibility. The nonlinear polarization is then defined thermodynamically by

$$P_i(2\omega) = \frac{\partial U}{\partial E_i^*(2\omega)} = \chi_{ijk}E_j(\omega)E_k(\omega). \quad (2.14)$$

This approach shows that SHG arises as a direct consequence of the anharmonic response of the medium to an applied electric field. Moreover, in works [4–6], it has been shown that magnetic order can also be probed by SHG, which arises from both electric and magnetic dipole polarizations $P(2\omega)$ and $M(2\omega)$, respectively, making SHG a highly sensitive probe of local symmetry breaking, particularly useful for imaging antiferromagnetic domains, where such symmetry reductions are induced by magnetic ordering.

2.2.3 SHG-based approach of antiferromagnetic order imaging in Cr_2O_3

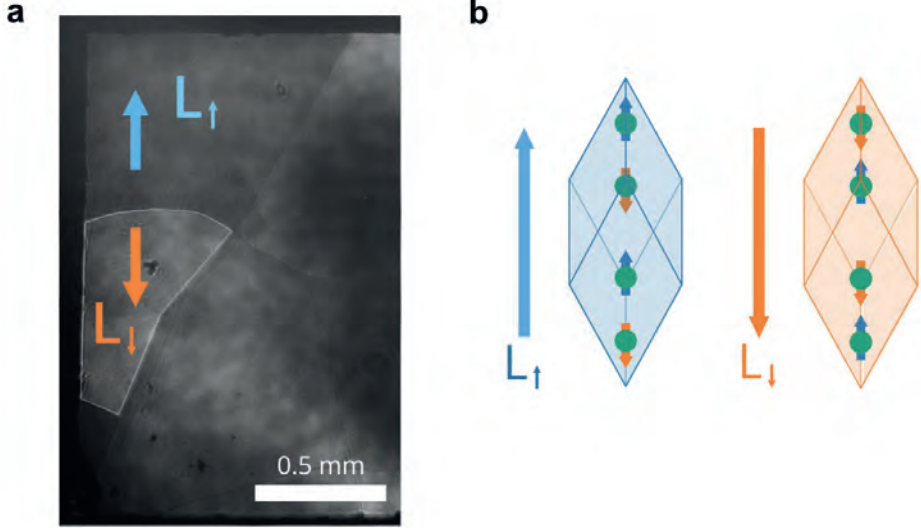


Figure 2.1: (a) Antiferromagnetic domain pattern of the Cr_2O_3 sample visualized by the technique of SHG. The domains with mutually opposite antiferromagnetic Néel vectors \mathbf{L}_\uparrow (blue) and \mathbf{L}_\downarrow (orange) are marked accordingly. (b) The rhombohedral unit cell of Cr_2O_3 (only magnetic Cr^{3+} ions are shown), illustrating antiferromagnetic domains with opposite spin arrangements and corresponding Néel vectors: $\leftarrow\rightarrow\leftarrow\rightarrow$ for \mathbf{L}_\uparrow , and $\rightarrow\leftarrow\rightarrow\leftarrow$ for \mathbf{L}_\downarrow , respectively [7, 8]. The image is taken from Ref. [9].

SHG provides a powerful method for mapping antiferromagnetic domains by leveraging its sensitivity to symmetry breaking. In centrosymmetric Cr_2O_3 above the Néel temperature (T_N), only the magnetic-dipole contribution is allowed:

$$M(2\omega) = \frac{\chi^m}{\mu_0} E(\omega)E(\omega), \quad (2.15)$$

while below T_N , the antiferromagnetic ordering breaks inversion symmetry, permitting an additional electric-dipole contribution:

$$P(2\omega) = \varepsilon_0\mu_0\chi^e E(\omega)E(\omega)\mathbf{L}. \quad (2.16)$$

Because the Néel vector \mathbf{L} reverses under inversion, the SHG intensity using circularly polarized light ($\sigma = \pm 1$) depends on both \mathbf{L} and the polarization state.

This interference between the magnetic- and electric-dipole contributions can be described as

$$I(2\omega) \sim E^4(\omega) \left(\frac{|\chi^m|^2}{\mu_0^2} + \varepsilon_0^2 \mu_0^2 |\chi^e|^2 \mathbf{L}^2 - 2 \frac{\varepsilon_0}{\mu_0} \left(\chi^{m'} \chi^{e''} - \chi^{m''} \chi^{e'} \right) \mathbf{L} \sigma \right), \quad (2.17)$$

where χ^m and χ^e are complex tensors ($\chi = \chi' + i\chi''$) [6, 10].

By illuminating the sample with circularly polarized light and recording the SHG signal (according to 2.17) with a CCD camera, antiferromagnetic domains can be resolved with high spatial resolution and short exposure times (Figure 2.2.3). This nonlinear optical approach thus offers a direct and efficient means for visualizing 180° antiferromagnetic domains, revealing subtle differences in domain orientation through changes in the SHG signal [6, 9, 10].

2.3 Optical pump–probe spectroscopy for ultrafast lattice and spin dynamics

Optical pump–probe spectroscopy is a powerful tool for probing ultrafast dynamics in solids, enabling the investigation of transient lattice vibrations and spin processes on femtosecond to picosecond timescales. By using two laser pulses, one to initiate non-equilibrium states in the material and another to monitor its relaxation, this technique provides a dynamic “movie” of the evolving optical properties. The following sections describe the ultrafast laser system, pulse characterization, and the pump–probe methodology employed in our experiments.

2.3.1 Ultrafast laser systems and pulse characterization

The ultrafast laser system is based on a Ti:Sapphire regenerative amplifier that delivers linearly polarized femtosecond pulses at 1 kHz with a fundamental wavelength of 800 nm (approximately 1.55 eV) [11, 12]. Pulse width characterization is performed using a standard autocorrelation technique [13] to ensure the pulse duration is maintained within the desired range of 40–50 fs. The femtosecond pulses have a Gaussian spatial shape profile, with the highest intensity at the center that tapers off toward the edges. This non-uniform profile leads to spatially inhomogeneous excitation across the sample. CCD imaging of the focused pump beam is used to capture the beam profile, and fitting the intensity distribution to a Gaussian function yields key parameters such as the full width at half maximum (FWHM) (Figure 2.2). For example, our pump spot in imaging experiments typically appears elliptical, tilted about 13°, with dimensions along the x - and y -axes of approximately 119 μm and 23.5 μm , respectively. This information is critical for correlating local laser fluence with the subsequent magneto-optical response.

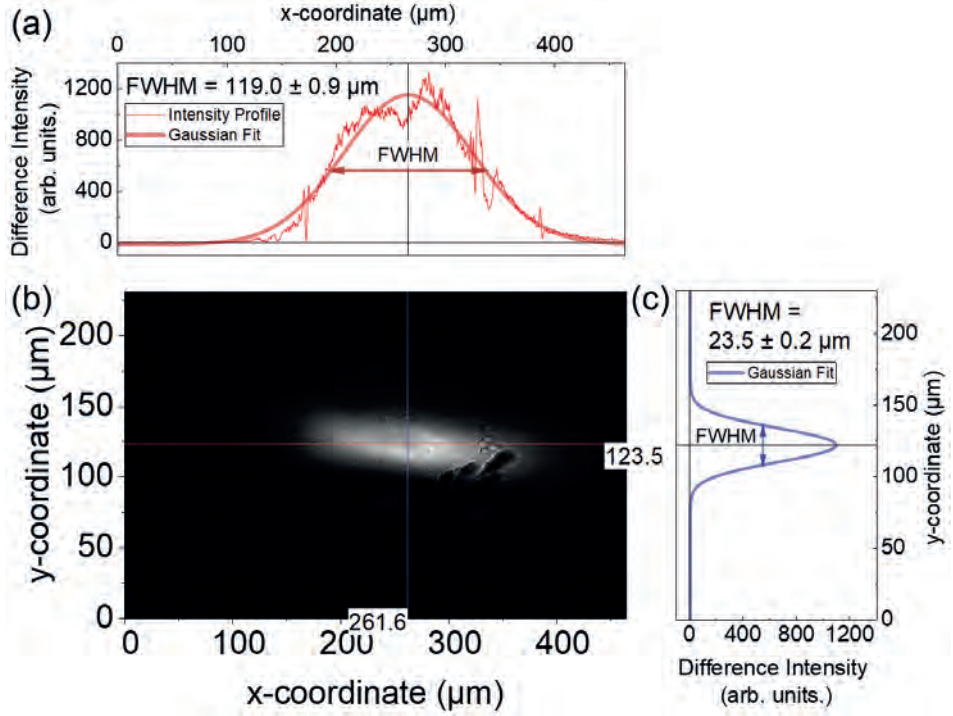


Figure 2.2: The spatial profile of the laser beam at the central wavelength of 800 nm. Panel (b) displays the CCD image of the laser spot after subtracting the background captured without the laser illumination. Panel (a) and (c) show the intensity profiles obtained by taking cross-sections of the image along the x - and the y -axis, respectively. Red and blue solid lines show Gaussian fits to the corresponding data, where full-width at half maximum (FWHM) was used as a fit parameter. The estimated FWHMs are given on the corresponding panels.

An optical parametric amplifier (OPA) is integrated to allow continuous tuning of the pump photon energy between 0.5 and 1.3 eV [14], which is essential for selectively exciting specific resonant transitions or converting the pulse wavelength to optimize the generation of nonlinear signals. Because the efficiency of wavelength conversion in the OPA varies with the output wavelength [14], it is crucial to account for these differences during power calibration. Moreover, changes in the optical path due to wavelength conversion also can alter the laser spot size. Such

variations are critical for wavelength-dependent measurements (e.g., in Chapter 3) and require additional alignment, calibration, and normalization.

2.3.2 Introduction to the pump-probe technique

The pump-probe technique is a powerful method for studying ultrafast transient processes in solids [15]. Its underlying principles resemble those used in early motion photography, where rapid movement was captured as a sequence of still images. A classic example is Eadweard Muybridge’s 1878 “Horse in Movement,” which captured the fleeting motion of a galloping horse through successive snapshots [16].

In a similar way, a typical pump-probe experiment is designed. Each ultra-short laser pulse is split into two parts: a more intense pulse is used as a pump, and a weaker pulse is used as a probe. The pump pulse excites the sample, driving it into a non-equilibrium state with altered optical properties, while the probe pulse, delayed by a precisely controlled optical path difference, monitors the excited dynamics. The time delay between the pump and probe is determined by the additional path length δl of the probe, with a delay given by $\delta l/c$, where c is the speed of light. For example, a 1 μm difference corresponds to a delay of approximately 3.3 fs. By systematically varying this delay, one can capture a “movie” of the evolving optical properties on timescales ranging from femtoseconds to picoseconds, thus revealing details of electronic and atomic motions.

The flexibility of the pump-probe method allows the probe wavelength to be chosen from different spectral regions, such as far-infrared [17], optical [18, 19], ultraviolet [20], or X-ray [21]. This multi-spectral approach provides various sensitivities to spin and orbital degrees of freedom, with even atomic specificity, offering a comprehensive view of the ultrafast dynamics. Early experiments, for instance by Knox et al. [22], demonstrated the power of this technique to monitor transient absorption and elucidate exciton lifetimes in semiconductors. The ultimate temporal resolution is governed by the pulse duration and the precision of the delay line, making modern ultrafast lasers and precise mechanical delay systems essential tools in this field.

The typical scheme of our two-colored pump-probe setup (e.g., used in Chapter 6) is illustrated in Figure 2.3. In our experiments, 800 nm (1.55 eV) pulse generated by the Ti:Sapphire amplifier is used as the pump, while the probe is provided by the OPA output, which is tunable from 950 to 2400 nm (0.5–1.3 eV). This two-color approach permits a collinear geometry, as a bandpass filter can effectively block the pump light from being detected by the balance detector. By contrast, one-color pump-probe schemes (e.g., as used in Ref. [23]) require a non-collinear geometry to avoid pump interference with the probe detection.

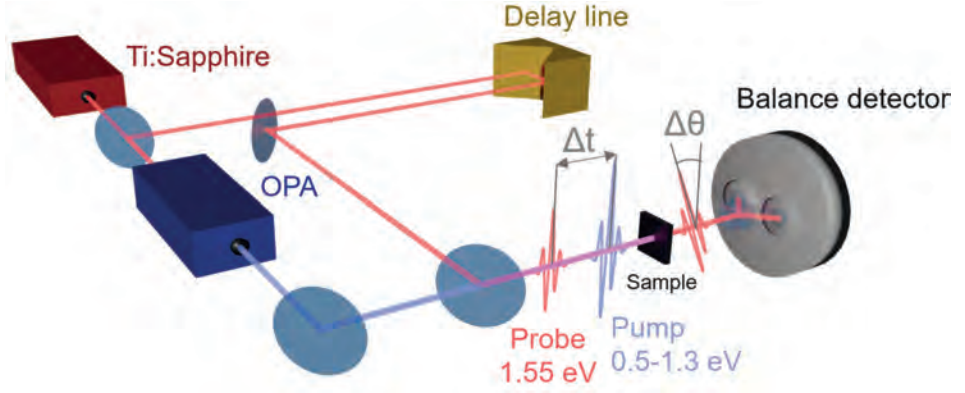


Figure 2.3: A schematic of the time-resolved pump-probe experiment in which pump-induced rotation $\Delta\theta$ of the probe polarization plane is tracked as a function of the pump-probe delay (Δt) using a Wollaston prism and balanced Si detector. The pump pulses with tunable pump photon energy (0.5 – 1.3 eV) are generated using an OPA.

2.4 Magneto-optical imaging of spin dynamics

The pump-probe imaging technique extends the traditional pump-probe method by capturing both temporal and spatial dynamics. Instead of simply measuring an averaged signal over the entire sample, pump-probe imaging records high-resolution images at various delay times. This spatial information enables the visualization of inhomogeneities, localized excitations, and propagating phenomena, such as spin waves, domain movement, and the formation of micromagnetic structures, that are often overlooked by conventional photodiode-based techniques [20, 24–27].

2.4.1 Experimental setup for spatially resolved measurements

Ultrafast magneto-optical imaging is performed using a monochrome CCD camera (Photometrics CoolSNAP HQ). In our pump-probe configuration, an unfocused, linearly polarized probe beam transmits through the sample, and a Glan–Taylor polarizer placed between the sample and the CCD camera detects polarization changes due to the Faraday effect (see Figure 2.4 for the geometry of the experiment). The rotation angle, $\Delta\theta$, is given by

$$\Delta\theta = VBL, \quad (2.18)$$

where V is the Verdet constant, B is the magnetic field along the light path, and L is the effective optical path length. The Faraday effect arises from differences in the dielectric response (ϵ) to right-handed (σ^+) and left-handed (σ^-) circularly polarized light, caused by electronic level splitting in an external field or the intrinsic magnetization M . To first order, this yields

$$\Delta\theta \propto M. \quad (2.19)$$

This measurement relies on Malus' law, which states that the transmitted intensity through the polarizer follows $I = I_0 \cos^2 \theta$. Even a small Faraday rotation thus produces a measurable change in intensity, enabling sensitive detection of magnetization variations.

2.5 Integration of electric fields with optical measurements

2.5.1 Electrical gating in ultrafast spin dynamics

Electrical gating is implemented by integrating a robust electrode configuration with the sample mounting. An epitaxial film of magneto-electric iron garnet, $(\text{BiLu})_3(\text{FeGa})_5\text{O}_{12}$, grown on a $\text{Gd}_3\text{Ga}_5\text{O}_{12}$ (GGG) substrate with a (110) orientation, is mounted on a plastic holder to avoid short circuits. Two stripe electrodes are applied using silver paste – one on the top surface and one on the bottom (with the backside electrode connected to the neutral “0” terminal via a wire). This electrode geometry was also chosen to avoid short circuits. A BeCu non-magnetic tip, connected to an ORTEC NIM high-voltage power supply (model 456), applies voltage to the front-side electrode. Although the power supply's working range is 0–3 kV, it was operated up to 0.5 kV in experiments with iron garnets (and up to 1.15 kV in experiments with Cr_2O_3). Voltage control is achieved either manually or externally via a BNC cable, where a small voltage (0–6 V) is linearly scaled to produce an output in the range of 0–1.5 kV. The output of the power supply is routed to a custom-designed controller box, which enables simultaneous application and measurement of the high voltage on the sample, providing real-time feedback. For the mounting geometry of the sample, see Figure 2.5.

For the iron-garnet experiments, the in-plane distance between the electrodes is 1 mm. These electrodes in such a configuration produce a uniform in-plane electric field across the pumped area, with a small out-of-plane component. By applying up to 500 V to the BiLu:IG electrode, an in-plane electric field of approximately 0.5 MV/m is achieved. Electrostatic simulations confirm that this field is both

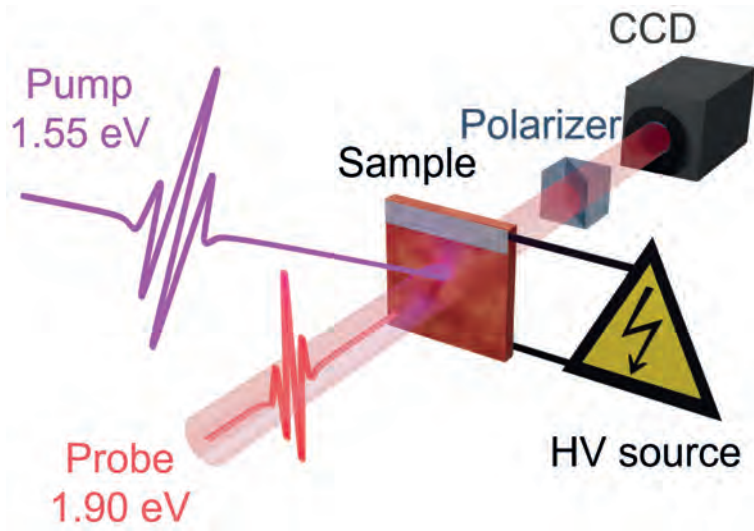


Figure 2.4: Scheme of the pump-probe imaging setup. The pump pulse, with a photon energy of 1.55 eV (800 nm wavelength), is focused into a small spot on the sample. The probe pulse, with a photon energy of 1.90 eV (650 nm wavelength), is unfocused and propagates through the delay line. A Glan-Taylor polarizer is mounted behind the sample before the camera, enabling the detection of the Faraday effect for micromagnetic structure visualization. For high-voltage experiments, an electric field is applied using two electrodes (fabricated with silver paste) positioned on opposite sides of the sample.

oriented in-plane and spatially homogeneous within the pumped area (see Figure 2.6). The sample is oriented so that the electric field lies along the desired in-plane direction, while an external magnetic field is applied perpendicular to it. This orthogonal arrangement is essential for probing the coupled dynamics of the system. With the pump initiating spin dynamics and the probe monitoring the response, the concurrent application of an electric field allows the capture of time-resolved changes directly influenced by electrical gating.

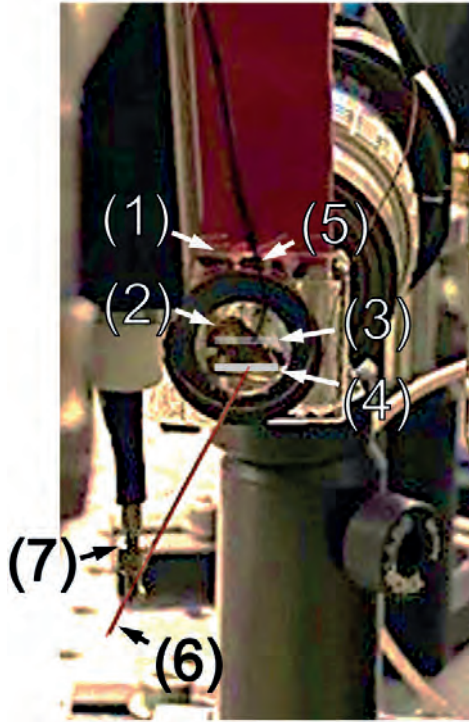


Figure 2.5: Photo of the mounted sample in the imaging setup.

- (1) Plastic holder for the sample to avoid short circuits.
- (2) Dielectric iron garnet sample.
- (3) Electrode (backside).
- (4) Electrode (front side).
- (5) Wire connected to the backside electrode (neutral “0” terminal).
- (6) BeCu $5\text{ }\mu\text{m}$ non-magnetic tip of the scanning probe station – BC-20-50 [28]
- (7) Screw nut tip holder with a coaxial connection, connected to a high-voltage power supply output. [29].

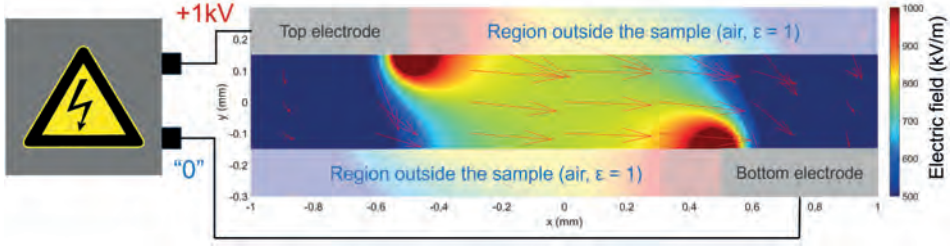


Figure 2.6: Calculated electric field distribution within the iron garnet film on a GGG substrate (central region between the regions “outside the sample” and “Top” and “Bottom” electrodes). A voltage of 1 kV was applied to the top electrode, while the bottom electrode was grounded. Color represents the magnitude of the electric field in kV/m (see color bar). Red arrows indicate the direction of the electric field. The calculation was performed using the actual spatial dimensions of the sample and substrate.

2.5.2 SHG imaging of antiferromagnetic domains under a locally applied electric field in Cr_2O_3

The SHG setup for Cr_2O_3 for imaging antiferromagnetic domains includes a Ti:Sapphire regenerative amplifier providing 40 fs linearly polarized pulses at 1.55 eV (800 nm) with a 1 kHz repetition rate. The setup is optimized for SHG measurements and control of antiferromagnetic domains in Cr_2O_3 . To increase the SHG response, these pulses are converted to 1.03 eV (approximately 1200 nm) using an OPA, and a quarter-wave plate adjusts the polarization to circular, enhancing the SHG signal’s sensitivity to the antiferromagnetic domains [10]. The setup allows us to apply electric and magnetic fields to the studied sample.

The beam is focused onto a Cr_2O_3 single crystal with a (0001) surface orientation. The generated second harmonic signal, at roughly 600 nm, is separated from the fundamental with a bandpass filter and imaged with a high-resolution CCD camera fitted with a micro-objective lens, achieving a spatial resolution of about 0.6 μm .

A BeCu non-magnetic tip [28] (Figure 2.9), connected to a high-voltage source (ranging from -1.15 kV to $+1.15$ kV), is used to apply a localized in-plane electric field with an inhomogeneous distribution (Figure 2.8). The connection scheme is similar to that presented in Section 2.4.1, except that the BeCu tip now makes direct contact with the sample.

Simultaneously, a permanent magnet supplies a uniform magnetic field of approximately 40 mT, oriented normal to the sample plane. This combined electric

(**E**) and magnetic (**B**) field configuration modulates the magnetoelectric coupling at the sample surface [30] and stabilizes the domain structure, facilitating detailed studies of domain wall movement. The experimental scheme is shown in Figure 2.7, and Figure 2.9 shows a microscopic image of the tip used to apply an electric field to the sample.

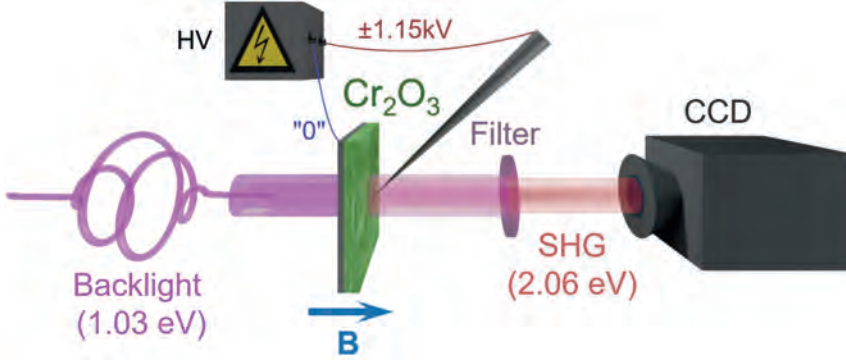


Figure 2.7: Schematic of the experimental SHG imaging setup. Circularly polarized probe pulses at 1.03 eV (1200 nm) generate a second harmonic signal at 600 nm, which is filtered and imaged with a high-resolution CCD camera. A BeCu non-magnetic tip in direct contact with the sample applies a localized electric field, while a permanent magnet provides an external magnetic field **B** (40 mT). HV indicates the high-voltage source, and “0” the neutral terminal.

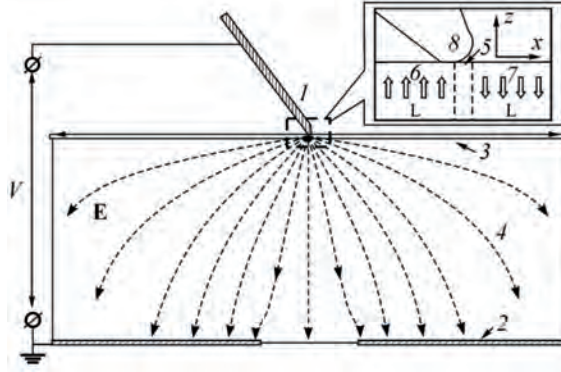


Figure 2.8: Schematic representation of the inhomogeneous distribution of the applied electric field in a similar experiment from Ref. [31] (figure is adapted). The electric field (dashed lines) is generated in the dielectric region of the sample between (1) the non-magnetic tip and (2) the metal diaphragm, which serves as the grounded electrode. The maximum field strength occurs in (3) the surface of the film near the needle tip and rapidly decreases within the bulk of the (4) substrate, falling near the (2) grounding electrode. The inset illustrates the magnetization distribution in the film: (5) an antiferromagnetic domain wall separates (6, 7) two domains with opposite antiferromagnetic vectors \mathbf{L} . (8) The needle contacts the sample surface close to the domain wall.

2.6 Conclusion

The standard and slightly modified experimental techniques provide a broad selection of tools to study ultrafast laser-induced dynamics in magnetoelectric media, writing of magnetic domains with electric field and light, as well as by combinations thereof. The methods can provide access to magnetic dynamics in ferro-, ferri-, and antiferromagnets. In particular, optical pump-probe spectroscopy provides femtosecond time resolution for capturing rapid lattice and spin dynamics, while magneto-optical imaging yields high spatial resolution of the spin dynamics in ferro- and ferrimagnets, where the net magnetization is not zero. Electrical gating techniques enable us to leverage magnetoelectricity and thus realize control of magnetism with the help of electric fields. The nonlinear optical technique of Second Harmonic Generation (SHG) is shown to provide a sensitive probe for imaging antiferromagnetic domains. All these methods form a sufficiently powerful toolbox

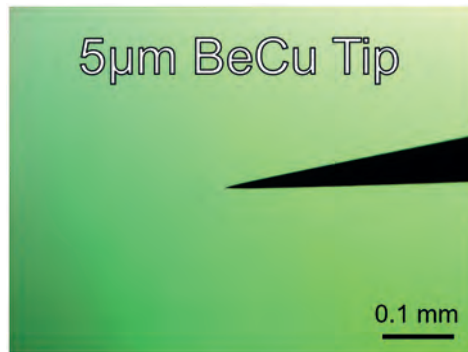


Figure 2.9: Image of the BeCu tip with a $5\text{ }\mu\text{m}$ end, used to apply an E -field locally to the sample. The image was captured using an optical microscope.

for the experimental research targeted in this thesis.

References

- [1] Lev Davidovich Landau, John Stewart Bell, MJ Kearsley, LP Pitaevskii, EM Lifshitz, and JB Sykes. *Electrodynamics of continuous media*, volume 8. elsevier, 2013.
- [2] Anatolii Zvezdin. *Modern magneto-optics and magneto-optical materials*.
- [3] AV Kimel, Th Rasing, and BA Ivanov. Optical read-out and control of antiferromagnetic neel vector in altermagnets and beyond. *Journal of Magnetism and Magnetic Materials*, page 172039, 2024.
- [4] Manfred Fiebig, Dietmar Fröhlich, BB Krichevstov, and Roman V Pisarev. Second harmonic generation and magnetic-dipole-electric-dipole interference in antiferromagnetic Cr_2O_3 . *Physical Review Letters*, 73(15):2127, 1994.
- [5] Manfred Fiebig, Victor V Pavlov, and Roman V Pisarev. Second-harmonic generation as a tool for studying electronic and magnetic structures of crystals. *Journal of the Optical Society of America B*, 22(1):96–118, 2005.
- [6] Vladislav Bilyk, Elena Mishina, Theo Rasing, and Alexey Kimel. Terahertz-induced second harmonic generation dynamics in antiferromagnetic Cr_2O_3 . *Physical Review B*, 110(17):174449, 2024.
- [7] Bo No Brockhouse. Antiferromagnetic structure in Cr_2O_3 . *The Journal of Chemical Physics*, 21(5):961–962, 1953.
- [8] LM Corliss, JM Hastings, R Nathans, and G Shirane. Magnetic structure of Cr_2O_3 . *Journal of Applied Physics*, 36(3):1099–1100, 1965.
- [9] VR Bilyk, RM Dubrovinn, AK Zvezdin, AI Kirilyuk, and AV Kimel. THz electric field control of spins in collinear antiferromagnet Cr_2O_3 . *arXiv preprint arXiv:2502.10181*, 2025.
- [10] Manfred Fiebig, D Fröhlich, G Sluyterman v. L, and RV Pisarev. Domain topography of antiferromagnetic Cr_2O_3 by second-harmonic generation. *Applied Physics Letters*, 66(21):2906–2908, 1995.
- [11] Spectra-Physics. Spitfire ace regenerative amplifier. <https://www.spectra-physics.com/en/f/spitfire-ace-regenerative-amplifier>. Accessed: 2025-03-19.
- [12] Spectra-Physics. Solstice ace ultrafast amplifier. <https://www.spectra-physics.com/en/f/solstice-ace-ultrafast-amplifier>. Accessed: 2025-03-19.
- [13] Rick Trebino and Erik Zeek. *The Autocorrelation, the Spectrum, and Phase Retrieval*, pages 61–99. Springer US, Boston, MA, 2000.

- [14] Light Conversion. Topas prime opa. <https://lightcon.com/products/topas-prime-opa/>. 2025-03-19.
- [15] KH Bennemann. Ultrafast dynamics in solids. *Journal of Physics: Condensed Matter*, 16(30):R995, 2004.
- [16] photographer Muybridge, Eadweard. The horse in motion. "sallie gardner," owned by leland stanford; running at a 1:40 gait over the palo alto track, 19th june/ muybridge. California: Palo Alto, CA. Photograph., 1878. Retrieved from the Library of Congress, <https://www.loc.gov/item/97502309/>.
- [17] RD Averitt and Antoinette Jane Taylor. Ultrafast optical and far-infrared quasiparticle dynamics in correlated electronmaterials. *Journal of Physics: Condensed Matter*, 14(50):R1357, 2002.
- [18] AV Kimel, A Kirilyuk, PA Usachev, RV Pisarev, AM Balbashov, and Th Rasing. Ultrafast non-thermal control of magnetization by instantaneous photo-magnetic pulses. *Nature*, 435(7042):655–657, 2005.
- [19] B Koopmans, Grégory Malinowski, F Dalla Longa, D Steiauf, M Fähnle, T Roth, M Cinchetti, and M Aeschlimann. Explaining the paradoxical diversity of ultrafast laser-induced demagnetization. *Nature materials*, 9(3):259–265, 2010.
- [20] Peter R Miedaner, Nadia Berndt, Jude Deschamps, Sergei Urazhdin, Nupur Khatu, Danny Fainozzi, Marta Brioschi, Pietro Carrara, Riccardo Cucini, Giorgio Rossi, et al. Excitation and detection of coherent nanoscale spin waves via extreme ultraviolet transient gratings. *Science Advances*, 10(36):eadp6015, 2024.
- [21] Michele Buzzi, Michael Först, Roman Mankowsky, and Andrea Cavalleri. Probing dynamics in quantum materials with femtosecond x-rays. *Nature Reviews Materials*, 3(9):299–311, 2018.
- [22] WH Knox, RL Fork, MC Downer, DAB Miller, DS Chemla, CV Shank, AC Gossard, and W Wiegmann. Femtosecond dynamics of resonantly excited excitons in room-temperature gaas quantum wells. *Physical review letters*, 54(12):1306, 1985.
- [23] F Formisano, RM Dubrovin, RV Pisarev, AM Kalashnikova, and AV Kimel. Laser-induced thz magnetism of antiferromagnetic cof2. *Journal of Physics: Condensed Matter*, 34(22):225801, 2022.
- [24] M Vomir, LHF Andrade, L Guidoni, E Beaurepaire, and J-Y Bigot. Real space trajectory of the ultrafast magnetization dynamics in ferromagnetic metals. *Physical review letters*, 94(23):237601, 2005.

-
- [25] Andrei Kirilyuk, Alexey V Kimel, and Theo Rasing. Ultrafast optical manipulation of magnetic order. *Reviews of Modern Physics*, 82(3):2731–2784, 2010.
 - [26] Paul Steven Keatley, VV Kruglyak, Prim Gangmei, and RJ Hicken. Ultrafast magnetization dynamics of spintronic nanostructures. *Philosophical Transactions of the Royal Society A: Mathematical, Physical and Engineering Sciences*, 369(1948):3115–3135, 2011.
 - [27] AJ Schellekens, KC Kuiper, RRJC De Wit, and B Koopmans. Ultrafast spin-transfer torque driven by femtosecond pulsed-laser excitation. *Nature communications*, 5(1):4333, 2014.
 - [28] Everbeing Prober. Probing tips. <https://everbeingprober.com/products/probing-tips/>. Accessed: 2025-03-19.
 - [29] Everbeing Prober. Tip holders. <https://everbeingprober.com/products/tip-holders/>. Accessed: 2025-03-19.
 - [30] Robert R Birss. Symmetry and magnetism. 1964.
 - [31] Aleksandr Sergeevich Logginov, Georgy Aleksandrovich Meshkov, Alexey Vladimirovich Nikolaev, and Aleksandr Pavlovich Pyatakov. Magnetoelectric control of domain walls in a ferrite garnet film. *JETP Letters*, 86:115–118, 2007.

Chapter 3

Strongly inhomogeneous spin dynamics induced by ultrashort laser pulses with a gradient intensity profile in magnetoelectric iron garnet

Using ultrafast imaging of an epitaxial film of magnetoelectric iron garnet, we show that a femtosecond laser pulse with a Gaussian light intensity distribution in the beam efficiently excites a strongly inhomogeneous spin dynamics in the magnet. We argue that the mechanism responsible for excitation is general for the systems with competitive magnetic anisotropies. Overlooking this effect in pump-probe experiments may result in a dramatic underestimation of the amplitude of the laser-induced spin dynamics, suggesting that in these experiments the latter is substantially larger than it has been believed until now.

Adapted from: [T.T. Gareev](#), N.E. Khokhlov, L. Körber, A. V. Kimel, “Strongly inhomogeneous spin dynamics induced by ultrashort laser pulses with a gradient intensity profile”, *Physical Review Letters*, **135**, 156701 (2025).

3.1 Introduction

The field of ultrafast magnetism aims to understand spin dynamics in magnetically ordered media excited by ultrashort (sub-100 ps) stimuli. The ability to generate and control spin waves in magnetic materials using femtosecond laser pulses [1–8] opened up exciting opportunities for merging spintronic or magnonic technologies with photonics [9–14]. As progress in the field of ultrafast magnetism is predominantly driven by experimental discoveries, the pump-probe technique has practically become the main tool in this field of research. Here we report that using ultrafast imaging, we discovered a counterintuitive, and therefore often overlooked, strongly inhomogeneous spin dynamics. We argue that such a dynamic can be excited even if the laser beam has a relatively large diameter and a Gaussian light intensity distribution. In particular, we find that the strongly inhomogeneous magnetization oscillations on spatial scales much smaller than the pump spot originate from the different ultrafast dynamics of competing magneto-crystalline and shape anisotropies.

3.2 Experiment

The sample is an epitaxial $1.72\text{ }\mu\text{m}$ thick film of iron garnet $(\text{BiLu})_3(\text{FeGa})_5\text{O}_{12}$, grown on a $\text{Gd}_3\text{Ga}_5\text{O}_{12}$ (GGG) substrate with a (110) crystallographic orientation. The saturation magnetization of the sample is 13.5 kA/m , and its out-of-plane uniaxial anisotropy has a parameter of 194 J/m . In the experiments, an external magnetic field \mathbf{B} is applied in the sample plane using an electromagnet (Figure 3.1a). We studied magnetization dynamics launched by femtosecond laser pulses using a time-resolved pump-probe imaging technique as described in detail elsewhere [15]. A Ti:Sapphire regenerative amplifier provides linearly polarized 45-fs laser pulses at a photon energy of 1.55 eV and a 1 kHz repetition rate. The initial pulse is divided into pump and probe parts. The pump was focused on the sample at an incidence angle of 10° , forming an elliptical spot with minor and major axes of $30\text{ }\mu\text{m}$ and $130\text{ }\mu\text{m}$, respectively. The intensity distribution along the axes of the ellipse had a Gaussian shape. An optical parametric amplifier converted the photon energy of the probe pulses to 1.9 eV . The linearly polarized probe is directed through a mechanical delay stage equipped with a retroreflector to enable time resolution. The probe beam remained unfocused on the sample. A Glan–Taylor polarizer placed between the sample and a CCD camera enabled the detection of the out-of-plane magnetization component m_z via the magneto-optical (MO) Faraday effect. The resulting MO images were recorded at different pump-probe time delays. All experiments were carried out at room temperature.

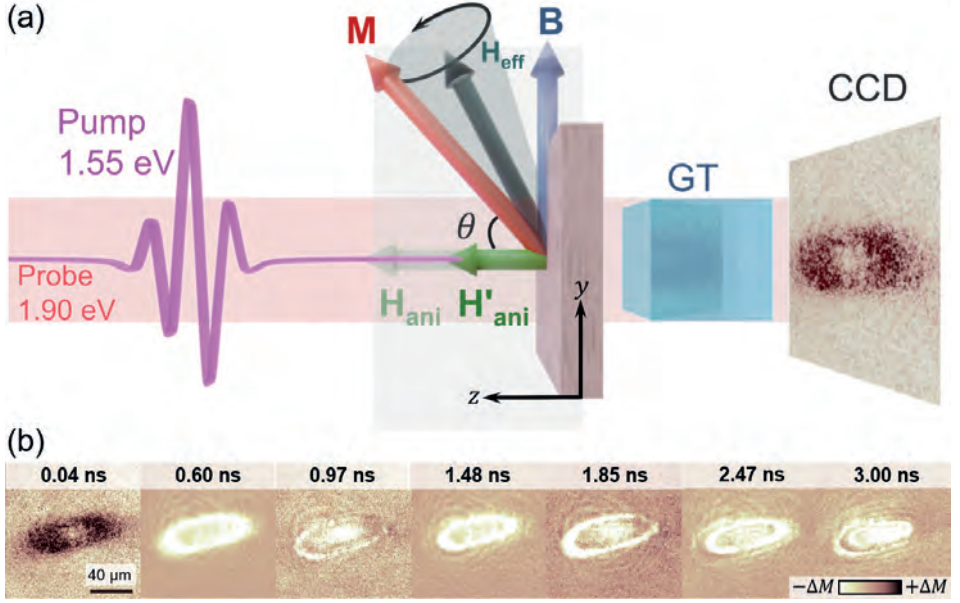


Figure 3.1: (a) Schematics of the experimental geometry. GT - Glan-Taylor polarizer. (b) MO snapshots of the spin dynamics at different time moments. The contrast scale was adjusted for each snapshot individually. The colorbar ($\pm\Delta M$) indicates the relative deviation of the magnetization vector with respect to the equilibrium state. The images were obtained at a magnetic field $B = 45$ mT.

3.3 Results and discussion

The used geometry, with non-collinear orientation of \mathbf{B} and anisotropy axis, provides the excitation of magnetization dynamics due to ultrafast reduction of the magnetocrystalline anisotropy [3, 16]. Here, we measured the excited dynamics in a standard stroboscopic pump-probe experiment except that the detector was a camera, not a photodiode or balanced pair of the two. As a result, a clear ring pattern is detected at the pump-probe delay $t = 0.04$ ns for a pump fluence of 85 mJ/cm^2 (Figure 3.1b). In the central area, the intensity of the MO signal is higher, while at the edges it is lower, indicating that the m_z -component has opposite signs in these areas. At 0.6 ns the contrast is the opposite, and at 0.97 ns the contrast is reversed again with a brighter central area. This alternating behavior continues for longer times within the pumped area. Moreover, the number of rings in the pattern increases progressively up to 3 ns. At the same time, the dynamics stay within the pumped area and do not propagate outside in the form of spin waves, as typically observed for tightly focused pumps [17–19].

To analyze the spatial-temporal evolution of the spin dynamics, we plotted the cross section of the MO snapshots (Figure 3.2a). The resulting spatial-temporal map demonstrates how the dynamics vary across the pump spot with the gradient of the laser fluence. It is clearly seen that the phase shift between the central and outer areas increases over time. To quantify the changes, we extracted the average intensity from the central area of the spot R_1 with minor and major axes of $17 \text{ }\mu\text{m}$ and $42 \text{ }\mu\text{m}$, respectively, and from the surrounding radial area R_2 with minor and major axes of $33 \text{ }\mu\text{m}$ and $75 \text{ }\mu\text{m}$, respectively (excluding the R_1 region). As a result, the oscillations in R_1 and R_2 exhibit opposite initial phases from the very beginning of the dynamics (Figure 3.2b). Importantly, the rings extend over tens of micrometers within a picosecond, which suggests that the dynamics are not driven by any propagation of magnons whose group velocities are typically three orders of magnitude lower [20, 21]. This suggests that the magnetization experiences initial torques acting in mutually opposite directions in different regions of the pumped area, probably due to the inhomogeneous temperature profile of the laser pulse.

To explain the initial torque distribution, we modeled the system as an ensemble of non-interacting macrospins, neglecting any interactions between them, such as exchange or dipolar coupling. In this approximation, the equilibrium orientation of each macrospin is then determined by minimizing its magnetic energy density, which is given by

$$\mathcal{F} = K_u \sin^2 \theta + \frac{1}{2} \mu_0 M_s^2 \cos^2 \theta - \mu_0 M_s H \sin \theta, \quad (3.1)$$

where θ is the polar angle of the unit magnetization vector, and K_u and M_s are temperature-dependent uniaxial anisotropy parameter and saturation magnetiza-

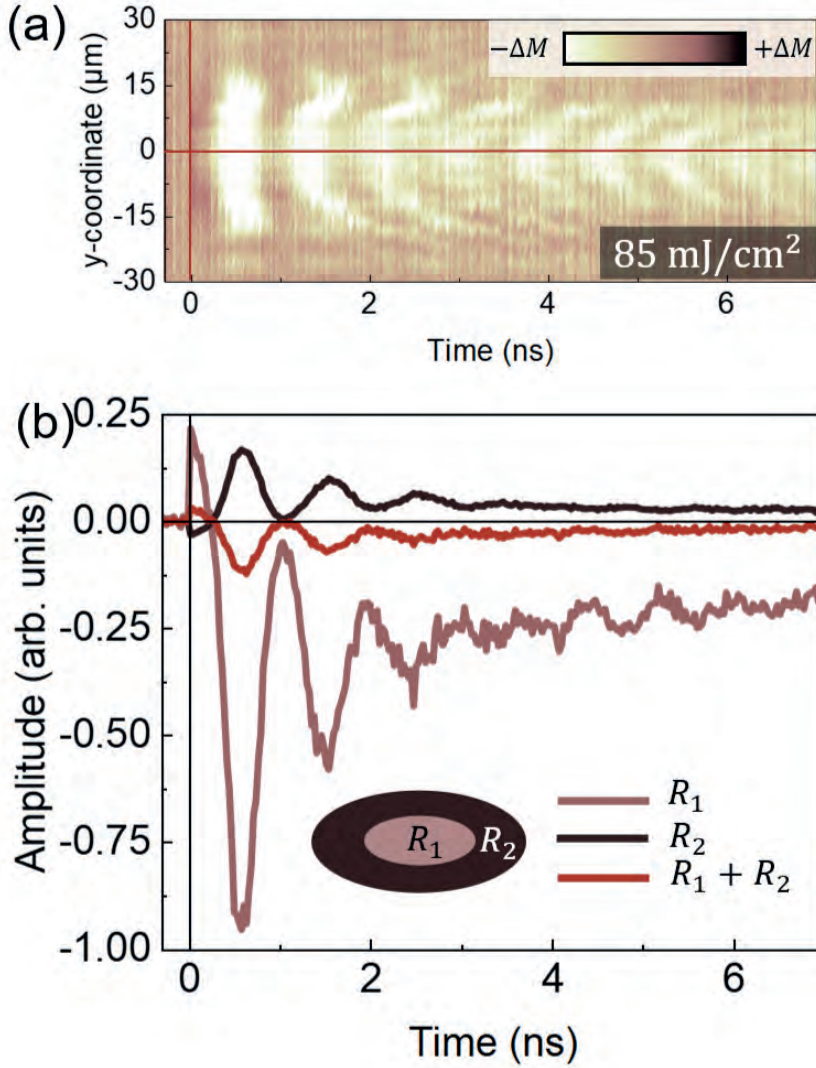


Figure 3.2: (a) Spatial-temporal evolution of the magneto-optical contrast in the central cross-section of the laser-excited area. (b) Magnetization dynamics integrated over the central area of the spot R_1 (ellipsis with $17\ \mu\text{m}$ and $42\ \mu\text{m}$ axes), over the edge area R_2 (ellipsis with $33\ \mu\text{m}$ and $75\ \mu\text{m}$ axes, excluding R_1), and over the full pumped area $R_1 + R_2$. The laser fluence is $85\ \text{mJ}/\text{cm}^2$, and $B = 45\ \text{mT}$.

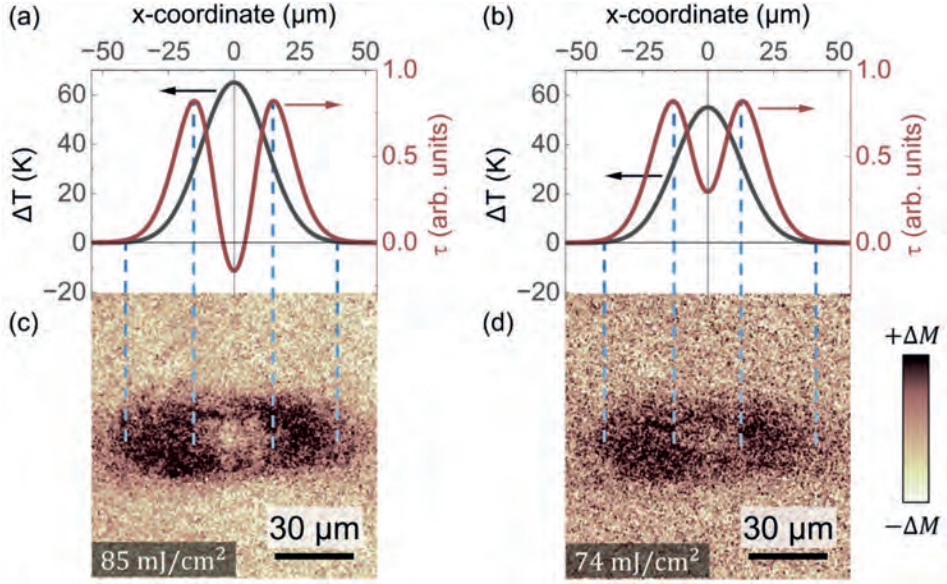


Figure 3.3: (a) Gaussian pump temperature profile with $\Delta T = 65 \text{ K}$ (black line) and corresponding spatial distribution of the laser-induced torque $\tau(x)$ (red line). (b) Gaussian pump temperature profile with $\Delta T = 55 \text{ K}$ (black line) and corresponding spatial distribution of $\tau(x)$ (red line). (c) Ring pattern observed at $t = 0.04 \text{ ns}$ with a laser fluence of 85 mJ/cm^2 and $B = 45 \text{ mT}$. (d) Ring pattern observed at $t = 0.04 \text{ ns}$ with a laser fluence of 74 mJ/cm^2 and $B = 45 \text{ mT}$.

tion, respectively, and $H = B\mu_0$ is the magnetic field strength (for the geometry of the model, see Figure 3.1a). Here, we assume that the temperature dependencies $M_s(T)$ and $K_u(T)$ follow an adapted Akulov–Zener approach [22, 23]:

$$M_s(T) = M_s(0) \left[1 - \left(\frac{T}{T_C} \right)^{3/2} \right] \quad (3.2)$$

$$K_u(T) = K_u(0) \left[1 - \left(\frac{T}{T_C} \right)^\beta \right]^3, \quad (3.3)$$

where $\beta = 12$ following Ref. [24]. Equations (3.1)–(3.3) give the spatial distribution of the initial torque $\tau = -\partial\mathcal{F}/\partial\theta$ for the Gaussian intensity profile of the pump (Figure 3.3a, b). In fact, ring formation occurs if τ changes the sign (Figure 3.3a). However, a more detailed analysis shows that the rings also appear in the MO snapshots when τ does not change sign, but there is a change in sign of its derivative $\partial\tau/\partial T$ (Figure 3.3b, d). Thus, there should be a threshold value for pump-induced temperature changes ΔT for ring formation. Indeed, in the experiment, $M_z(r)$ forms a ring if the laser fluence exceeds 60 mJ/cm^2 (Figure 3.4a), and this is well reproduced in the simulations (Figure 3.4b). Moreover, the deviation of the equilibrium angle $\Delta\theta$ also varies with temperature, and the threshold for ring formation is also defined by the sign of the derivative $\partial\theta/\partial T$ (Figure 3.4c). This also means that the gradient of ΔT is responsible for the inhomogeneous, slow-varying background in the detected signal (Figure 3.2b). As the model is based on laser-induced heating as well as different temperature dependencies of the magnetization and the magnetic anisotropy constant, which are all quite common in many pump-probe experiments, we argue that such strongly inhomogeneous spin dynamics should also be commonly appearing in many pump-probe experiments.

Despite the similarity of the ring-like pattern reported here and the final magnetization state after single-pulse magnetization switching observed before [24–26], our observations reveal a markedly different mechanism at the early stage of the dynamics. In particular, the ring pattern in Figure 3.1b is formed already within 0.04 ns after laser excitation, and we also see it clearly for the integrated area results in Figure 3.2b, while in Refs. [24, 26] laser excitation first led to a homogeneous in sign laser-induced torque, and the rings formed only afterward on the timescale of a precession period. Thus, our finding shows an additional inhomogeneous torque-based mechanism behind the ring-like pattern. We note that the observed magnetization precession and its switching in Refs. [24, 26] are two fundamentally different processes: linear and nonlinear. To compare their amplitudes, we used the MO contrast in Figure 3.1b and the value of the static MO Faraday effect to estimate the amplitude of the local magnetization deviation from equilibrium. For the case in Figure 3.1b, this amplitude is about 1.5° . In contrast,

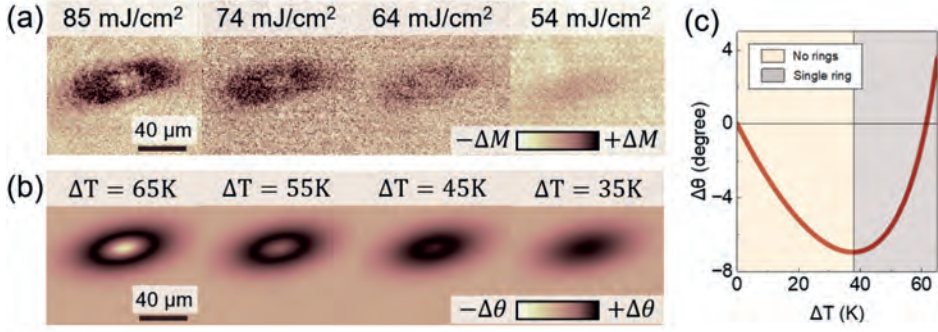


Figure 3.4: Pump fluence dependence. (a) Experimental snapshots of the spatial distribution of the out-of-plane magnetization component m_z for different pump fluences taken at $t = 0.04$ ns. (b) Spatial distributions of the variation of polar angle $\Delta\theta$ calculated as direct minimization of (3.1) for different peak values of pump-induced temperature increase ΔT . (c) Calculated variation $\Delta\theta$ versus ΔT . Ring formation is observed if derivative $\partial\theta/\partial T$ changes its sign.

the strong anharmonic spin dynamics reported in Ref. [24] implied amplitudes well above 10° .

3.4 Conclusion

In conclusion, we show that spin dynamics excited in a typical pump-probe experiment can be strongly inhomogeneous due to the Gaussian temperature distribution in the laser-excited area and the resulting inhomogeneous initial torque, and this inhomogeneity takes place on spatial scales much smaller than the pump spot size. The inhomogeneous torque-based mechanism is also very general and could be expected in a wide variety of pump-probe experiments on magnetic materials. It leads to a situation where probing of the whole pumped area gives a decrease in amplitude of the detected magnetization oscillations with lifetimes smaller than those observed in the center of the pump. Overlooking this effect in pump-probe experiments may result in a dramatic underestimation of the spin precession parameters.

References

- [1] M Van Kampen, C Jozsa, JT Kohlhepp, P LeClair, Lieven Lagae, WJM De Jonge, and B Koopmans. All-optical probe of coherent spin waves. *Physical review letters*, 88(22):227201, 2002.
- [2] M Vomir, LHF Andrade, L Guidoni, E Beaupaire, and J-Y Bigot. Real space trajectory of the ultrafast magnetization dynamics in ferromagnetic metals. *Physical review letters*, 94(23):237601, 2005.
- [3] Andrei Kirilyuk, Alexey V Kimel, and Theo Rasing. Ultrafast optical manipulation of magnetic order. *Reviews of Modern Physics*, 82(3):2731–2784, 2010.
- [4] Paul Steven Keatley, VV Kruglyak, Prim Gangmei, and RJ Hicken. Ultrafast magnetization dynamics of spintronic nanostructures. *Philosophical Transactions of the Royal Society A: Mathematical, Physical and Engineering Sciences*, 369(1948):3115–3135, 2011.
- [5] AJ Schellekens, KC Kuiper, RRJC De Wit, and B Koopmans. Ultrafast spin-transfer torque driven by femtosecond pulsed-laser excitation. *Nature communications*, 5(1):4333, 2014.
- [6] Ivan S Maksymov. Magneto-plasmonics and resonant interaction of light with dynamic magnetisation in metallic and all-magneto-dielectric nanostructures. *Nanomaterials*, 5(2):577–613, 2015.
- [7] Tim Titze, Sabri Koraltan, Timo Schmidt, Dieter Suess, Manfred Albrecht, Stefan Mathias, and Daniel Steil. All-optical control of bubble and skyrmion breathing. *Physical review letters*, 133(15):156701, 2024.
- [8] Peter R Miedaner, Nadia Berndt, Jude Deschamps, Sergei Urzhudin, Nupur Khatu, Danny Fainozzi, Marta Brioschi, Pietro Carrara, Riccardo Cucini, Giorgio Rossi, et al. Excitation and detection of coherent nanoscale spin waves via extreme ultraviolet transient gratings. *Science Advances*, 10(36):eadp6015, 2024.
- [9] Tianyu Liu, Xufeng Zhang, Hong X Tang, and Michael E Flatté. Optomagnonics in magnetic solids. *Physical Review B*, 94(6):060405, 2016.
- [10] Puja Dey, Jitendra Nath Roy, Puja Dey, and Jitendra Nath Roy. Optospintronics. *Spintronics: Fundamentals and Applications*, pages 163–184, 2021.
- [11] Kai Wang, Yong-Pan Gao, Rongzhen Jiao, and Chuan Wang. Recent progress on optomagnetic coupling and optical manipulation based on cavity-optomagnonics. *Frontiers of Physics*, 17(4):42201, 2022.

- [12] Figen Ece Demirer, Yngwie Baron, Sander Reniers, Dzmitry Pustakhod, Reinoud Lavrijsen, Jos van der Tol, and Bert Koopmans. An integrated photonic device for on-chip magneto-optical memory reading. *Nanophotonics*, 11(14):3319–3329, 2022.
- [13] Luding Wang, Houyi Cheng, Pingzhi Li, Youri LW Van Hees, Yang Liu, Kaihua Cao, Reinoud Lavrijsen, Xiaoyang Lin, Bert Koopmans, and Weisheng Zhao. Picosecond optospintronic tunnel junctions. *Proceedings of the National Academy of Sciences*, 119(24):e2204732119, 2022.
- [14] Hamed Pezeshki, Pingzhi Li, Reinoud Lavrijsen, Martijn Heck, Erwin Bente, Jos van der Tol, and Bert Koopmans. Integrated hybrid plasmonic-photonic device for all-optical switching and reading of spintronic memory. *Physical Review Applied*, 19(5):054036, 2023.
- [15] A. Dolgikh, D. Afanasiev, V. V. Yurlov, M. V. Logunov, A. K. Zvezdin, and A. V. Kimel. Ultrafast heat-assisted magnetization dynamics in a ferrimagnetic insulator. *Phys. Rev. B*, 107:094424, Mar 2023.
- [16] AM Kalashnikova, NE Khokhlov, LA Shelukhin, and AV Scherbakov. Ultrafast laser-induced control of magnetic anisotropy in nanostructures. *Technical Physics*, 68(12):574–601, 2023.
- [17] Takuya Satoh, Yuki Terui, Rai Moriya, Boris A Ivanov, Kazuya Ando, Eiji Saitoh, Tsutomu Shimura, and Kazuo Kuroda. Directional control of spin-wave emission by spatially shaped light. *Nature Photonics*, 6(10):662–666, 2012.
- [18] Y Au, Mykola Dvornik, T Davison, E Ahmad, Paul Steven Keatley, Arne Vansteenkiste, Bartel Van Waeyenberge, and VV Kruglyak. Direct excitation of propagating spin waves by focused ultrashort optical pulses. *Physical review letters*, 110(9):097201, 2013.
- [19] Nikolai E Khokhlov, Petr I Gerevenkov, Leonid A Shelukhin, Andrei V Azovtsev, Nikolay A Pertsev, Mu Wang, Andrew W Rushforth, Alexey V Scherbakov, and Alexandra M Kalashnikova. Optical excitation of propagating magnetostatic waves in an epitaxial gallenol film by ultrafast magnetic anisotropy change. *Physical Review Applied*, 12(4):044044, 2019.
- [20] AV Chumak, AA Serga, and B Hillebrands. Magnonic crystals for data processing. *Journal of Physics D: Applied Physics*, 50(24):244001, 2017.
- [21] Abdulqader Mahmoud, Florin Ciubotaru, Frederic Vanderveken, Andrii V Chumak, Said Hamdioui, Christoph Adelmann, and Sorin Cotofana. Introduction to spin wave computing. *Journal of Applied Physics*, 128(16), 2020.

- [22] N Akulov. Zur quantentheorie der temperaturabhängigkeit der magnetisierungskurve. *Zeitschrift für Physik*, 100(3):197–202, 1936.
- [23] C Zener. Classical theory of the temperature dependence of magnetic anisotropy energy. *Physical Review*, 96(5):1335, 1954.
- [24] CS Davies, KH Prabhakara, MD Davydova, KA Zvezdin, TB Shapaeva, S Wang, AK Zvezdin, A Kirilyuk, Th Rasing, and AV Kimel. Anomalously damped heat-assisted route for precessional magnetization reversal in an iron garnet. *Physical review letters*, 122(2):027202, 2019.
- [25] Y Peng, D Salomoni, G Malinowski, W Zhang, Julius Hohlfeld, LD Buda-Prejbeanu, J Gorchon, M Vergès, JX Lin, D Lacour, et al. In-plane reorientation induced single laser pulse magnetization reversal. *Nature Communications*, 14(1):5000, 2023.
- [26] K. Mishra, T. G. H. Blank, C. S. Davies, L. Avilés-Félix, D. Salomoni, L. D. Buda-Prejbeanu, R. C. Sousa, I. L. Prejbeanu, B. Koopmans, Th. Rasing, A. V. Kimel, and A. Kirilyuk. Dynamics of all-optical single-shot switching of magnetization in tb/co multilayers. *Phys. Rev. Res.*, 5:023163, Jun 2023.

Chapter 4

Electrically-gated laser-induced spin dynamics in magneto-electric iron garnet at room temperature

Ultrafast pump-probe imaging reveals that the efficiency of optical excitation of coherent spin waves in epitaxial iron garnet films can be effectively controlled by an external electric field at room temperature. While a femtosecond laser pulse alone does not excite any pronounced coherent spin oscillations, an electrical gating with the field of 0.5 MV/m dramatically changes the outcome in a laser-induced launching of spin waves. The effect, demonstrated under room temperature conditions, is estimated to be orders of magnitude larger than in magnetic van der Waals semiconductors observed at 10 K. This electrical gating of laser-induced spin dynamics enriches opto-magnonics with a new tool and thus opens up a new avenue in fundamental and applied magnonics research.

Adapted from: [T.T. Gareev](#), N.E. Khokhlov, L. Körber, A. P. Pyatakov, A. V. Kimel “Ultrafast electrically-gated laser-induced spin dynamics in magneto-electric iron garnet at room temperature”, arXiv preprint arXiv:2506.20366 (2025).

4.1 Introduction

The ability to excite and control spin waves in magnets with the help of light opens up opportunities for the integration of spintronic or magnonic technologies with photonics and thus stimulates the development of novel opto-spintronic and opto-magnonic devices [1]. One of the main challenges in the field is a mismatch between the length-scales of a targeted device in spintronics or magnonics with bit sizes on the order of ~ 100 nm and the telecom wavelength of ~ 1 μm . For instance, using light in these technologies for controlling spins would require to focus light into a spot much smaller than the wavelength of light, which is quite challenging [2, 3], though in principle achievable, e.g., in HAMR (Heat-Assisted Magnetic Recording) devices [4] or by using plasmonic antennas [5]. Another possible approach to overcome this limitation is electric gating of optically induced spin excitations, which facilitates optical control of spins with spatial resolution defined by the area of the applied electric field [6]. Finding a material with the strongest effect of the electric field on light-spin coupling has become one of the challenges in modern magneto-electric research. Recently, it was argued that 2D magnetic semiconductors provide an ideal platform for electric manipulation of magnetization [7]. It was shown that at low-temperature conditions ($T = 10$ K), applying an electric field on the order of GV/m can control an optically excited spin wave. Here, using ultrafast imaging, we show that in an iron garnet epitaxial film, similar effects can be achieved at room temperature while applying electric fields 10^3 times lower.

4.2 Sample and experimental setup

An epitaxial film of iron garnet $(\text{BiLu})_3(\text{FeGa})_5\text{O}_{12}$ (BiLu:IG) with a thickness of 1.72 μm was grown on a $\text{Gd}_3\text{Ga}_5\text{O}_{12}$ (GGG) substrate with (110)-crystallographic orientation. The sample's magnetic parameters are $M_s = 13.5$ kA/m and $K_u = 194$ J/m³.

In the experiments, an external magnetic field \mathbf{B} is applied in the sample plane with an electromagnet (top inset of Figure 4.1). The sample becomes in a monodomain state at $B = \pm 10$ mT (Figure 4.1). To apply the in-plane electric field \mathbf{E} , we placed two stripe electrodes: one on top of the garnet film and the second on the bottom of the GGG substrate. The electrodes were created with silver paste and oriented in a way that the applied fields \mathbf{E} and \mathbf{B} are orthogonal. The distance between the electrodes is 0.5 mm. Applying a voltage in the range of 0 - 500 V, we generated an electric field with a strength up to 0.5 MV/m. In the model we also consider that because of the electrode mounting geometry, a small electric field component along the z -axis is present. Its impact is assumed to be

about two orders of magnitude lower than that along the y -axis. All experiments are performed at an ambient temperature of 295K.

Magneto-optical static measurements of the Faraday rotation angle ψ with E -field reveal changes in the hysteresis loop (bottom inset in Figure 4.1). Upon application of the field, the hysteresis loop shrinks. The measurements reveal that the E -field works as an effective magnetic field with in-plane orientation.

To investigate magnetization dynamics, we performed time-resolved pump-probe imaging experiments [8, 9]. A Ti:Sapphire regenerative amplifier was a source of linearly polarized 45 fs laser pulses at a photon energy of 1.55 eV with the repetition rate of the pulses of 1 kHz. The pulses are split into two parts – pump and probe. The most intense pulse was used to pump, and the less intense pulse was used to probe the spin dynamics. The linearly polarized pump is focused on the sample at an incidence angle of 10° in an elliptical spot having minor and major axes of $30\text{ }\mu\text{m}$ and $130\text{ }\mu\text{m}$, respectively. The probe pulse is converted to 1.9 eV with an optical parametric amplifier. Then, the unfocused linearly polarized probe is used for visualization of magnetization dynamics with a mechanical delay stage. The Glan-Taylor polarizer is placed behind the sample in front of the CCD camera, which is used to visualize the changes in the out-of-plane magnetization component m_z via the Faraday effect (for a detailed scheme of the experiment, see Ref. [9]).

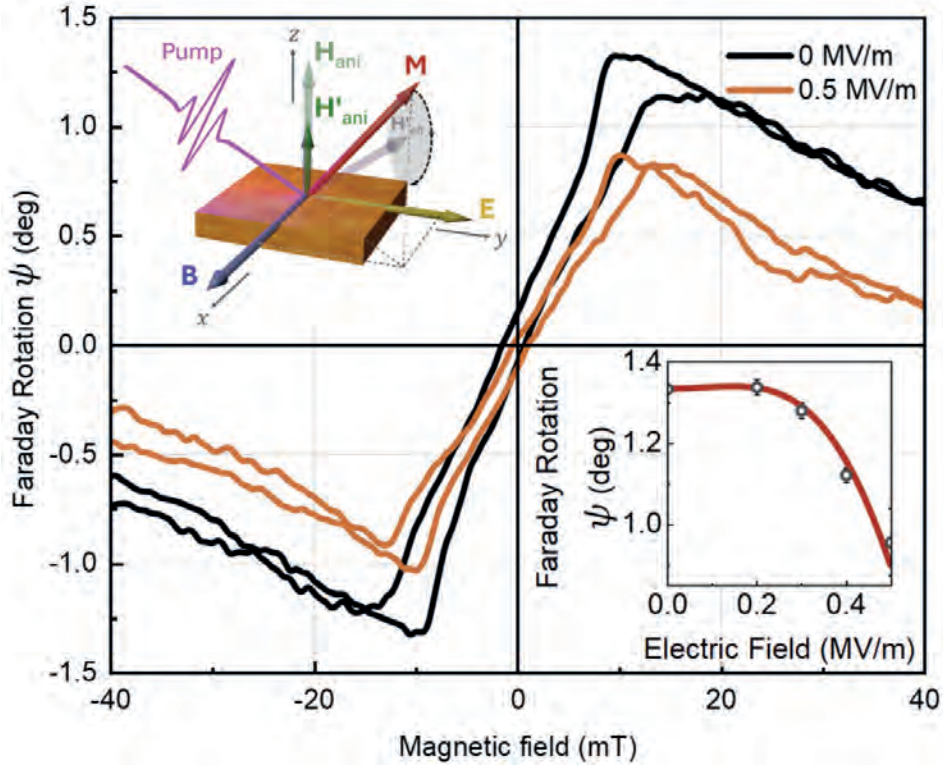


Figure 4.1: Magneto-optical measurements of Faraday rotation angle ψ of the probe showing the hysteresis loop without (black curve) and with an applied electric field to the sample (orange curve). Top left: scheme of the experiment. Bottom right: The maximum amplitude of the Faraday rotation angle as a function of the applied electric field. The red curve is a guideline to the eyes.

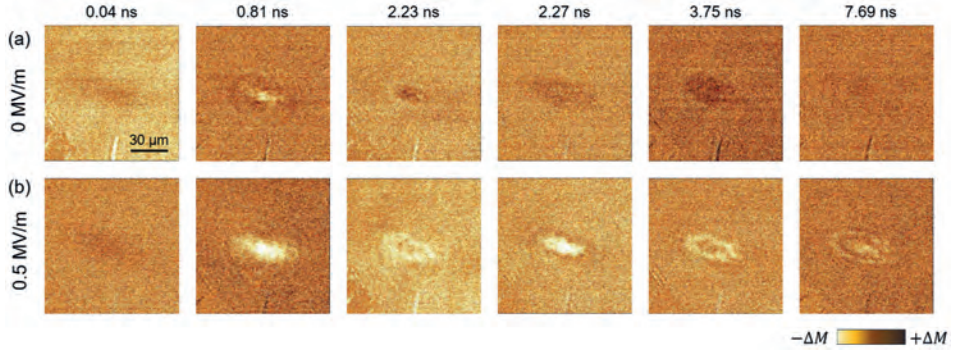


Figure 4.2: (a, b) Time-resolved magneto-optical images of electric field-controlled laser-induced spin dynamics. The images were captured at different moments in time without (a) and with (b) an applied electric field. A magnetic field of $B = 30$ mT was applied in all experiments. The laser fluence was 36 mJ/cm^2 .

4.3 Results and discussion

In the pump-probe experiments, we capture magneto-optical images at different moments in time, both without and with an applied E -field, as shown in Figure 4.2a and Figure 4.2b, respectively. No pronounced spin dynamics is observed at $E = 0$ (Figure 4.2a): after the initial overlap at 0.04 ns, a decrease in magneto-optical contrast is observed in the pumped area. At 0.81 ns, a change in phase is clearly observed. At 2.23 ns, the formation of a ring-like pattern is detected. However, this feature disappeared at 2.27 ns. Finally, at 7.69 ns, no m_z dynamics is detected. In contrast, pronounced oscillations appear when an E -field is applied (Figure 4.2b): at 0.04 ns, the magneto-optical snapshot closely resembles the picture at $E = 0$. At 0.81 ns, m_z changes sign, similar to the case of $E = 0$, but with a significantly larger amplitude. At 2.23 ns, the formation of the ring-like pattern is more pronounced, with the opposite variation of m_z in the central region and at the edges of the area exposed to the laser. At 7.69 ns, multiple rings are present. To gain more insights into the E -dependent spin dynamics, we quantify the dynamics of the averaged intensity in the central area of the spot and plot the deduced numbers as a function of time delay (Figure 4.3). These data clearly demonstrate that the application of an electric field enables to trigger magnetization oscillations at 0.6 GHz. At the same time, no pronounced signal is observed with no electric field, i.e., when $E = 0$.

To explain the experimental observation of the effect of the E -field on the

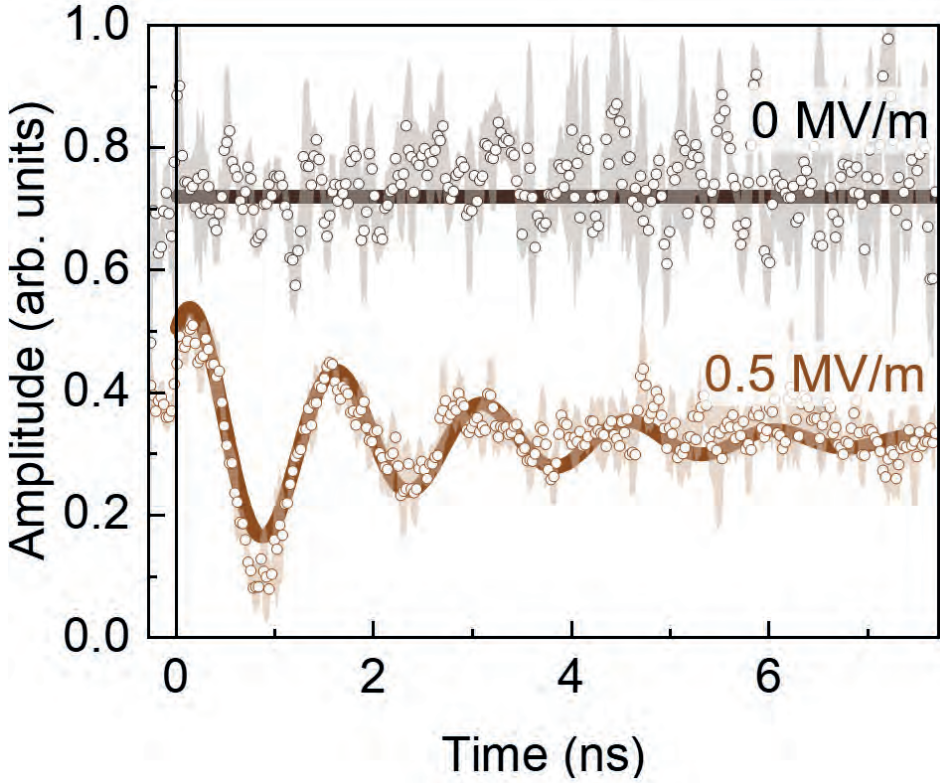


Figure 4.3: Magnetization dynamics extracted from the time-resolved magneto-optical images without (black) and with applied electric field $E = 0.5$ MV/m (orange). A magnetic field was applied in the plane of the sample ($B = 30$ mT). The laser fluence was 36 mJ/cm². Note that the two sets of traces are offset relative to each other.

spin dynamics we solve the Landau-Lifshitz-Gilbert (LLG) equation [10, 11]. The geometry of the model is present in Figure 4.1 (top left).

$$\frac{d\mathbf{m}}{dt} = -\frac{\gamma}{1+\alpha^2} \mathbf{m} \times \mathbf{B}_{\text{eff}} - \frac{\alpha\gamma}{1+\alpha^2} \mathbf{m} \times (\mathbf{m} \times \mathbf{B}_{\text{eff}}), \quad (4.1)$$

where $|\mathbf{m}| = 1$ is the unit magnetization vector, γ is the gyromagnetic ratio, and α is the (dimensionless) Gilbert damping parameter. The effective field

$$\mathbf{B}_{\text{eff}} = B_{\text{ext}} \mathbf{e}_x + \frac{2\gamma|\mathbf{E}|^2}{M_s} (\mathbf{m} \cdot \mathbf{e}_y) \mathbf{m}_y + \frac{2K_{\text{eff}}}{M_s} (\mathbf{m} \cdot \mathbf{e}_z) \mathbf{m}_z \quad (4.2)$$

includes the external magnetic field B_{ext} , the magnetization saturation M_s , the magneto-electric coefficient γ , and the effective anisotropy $K_{\text{eff}} = K_{\text{uni}} - \mu_0 M_s/2$, where the uniaxial perpendicular magnetic anisotropy (K_{uni}) is combined with the shape anisotropy (treated in the local dipole-dipole approximation). The E -field is introduced as a quadratic ME term in a similar way as in [12]. We assume that the laser-induced spin dynamics arises from heating by the laser pulse, which changes the magneto-crystalline anisotropy and the magnetization saturation parameter according to the Akulov-Zener law [9, 13–15].

For LLG modeling, we select parameters close to the magnetic parameters of the sample: $M_s(0 \text{ K}) = 24 \text{ kA/m}$, $K_u(0 \text{ K}) = 290 \text{ J/m}^{-1}$, and $T_C = 400 \text{ K}$. The magnetic parameter $\beta = 12$ for the adapted Akulov-Zener law [13, 14] was taken from [15]. The temperature change in the model is set to $\Delta T = 20 \text{ K}$. The magnetoelectric constant was set to $\gamma = 5 \cdot 10^{-14} \text{ J/(m}\cdot\text{V}^2)$, which is of the same order as the values reported in the literature [12].

We present numerical simulations of the time-resolved magnetization component m_z under E -fields ranging from 0 to 1.5 MV/m, as shown in Figure 4.4a. While at zero applied electric field, the oscillations have a very small amplitude; an increase of the field results in first an increase and then a decrease of the amplitude with a maximum approaching 1 MV/m. From the comparison of the calculated magnetization trajectories (Figure 4.4b), it is evident that the oscillation amplitude increases, reaching a maximum with the applied field up to $E \approx 1.07 \text{ MV/m}$ (dark orange curve in Figure 4.4c). In Figure 4.4a, b, we also observe that the oscillation frequency gradually decreases as the applied electric field increases from 0 to 1 MV/m. Upon reaching a minimum, the frequency starts to increase again ($E = 1.15 \text{ MV/m}$). At this point, the equilibrium m_z component decreases as the system approaches saturation (black curve in Figure 4.4c). Beyond this threshold, further increases in the E -field lead to a rapid collapse of m_z , causing the spin dynamics to vanish.

The simulations show good agreement with the experimental results, although the range of electric fields accessible in the experiments was limited by the constraints of the setup [Experiment: Figure 4.1 (bottom right – static), Figure 4.3 (dynamics); Theory: Figure 4.4c (black curve – static), Figure 4.4a (dynamics)].

The modeling parameters differ slightly from the experimental values because the exact temperature dependence of the magnetic parameters is unknown. Therefore, we use zero-temperature estimates extrapolated via the adapted Akulov-Zener law [13–15], which yield values representative for $T \approx 0 \text{ K}$. These values provide a reasonable approximation for modeling the magnetization dynamics triggered by ultrafast laser heating. Additionally, real materials like iron garnet films often exhibit more complex anisotropy contributions (e.g., orthorhombic and cubic terms), which are also temperature-dependent, that are not included in the simplified uniaxial model used here. The chosen parameters capture the key qualitative features of the magnetization dynamics and allow us to describe and predict the effect of the electric field on it.

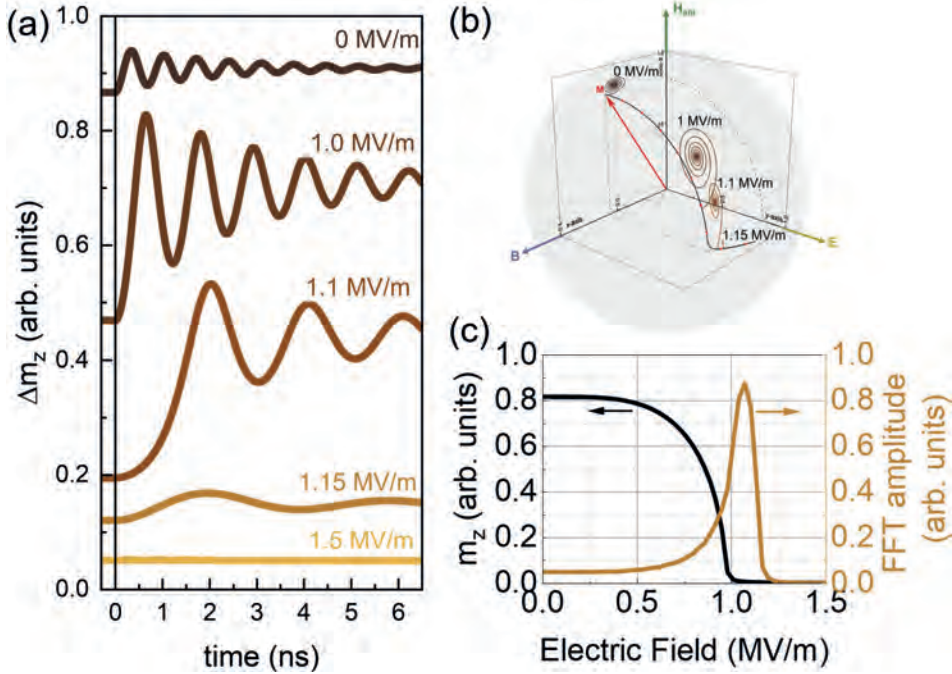


Figure 4.4: (a) Numerically calculated dynamics of the normal component of the magnetization m_z with and without an applied electric field. The dynamics are triggered as a result of ultrafast heating leading to different dynamics of magneto-crystalline anisotropy and magnetization, as explained in Ref. [9]. (b) 3D-trajectory of the magnetization vector \mathbf{M} at equilibrium position under applied electric field (black curve). The E -field was applied in the range 0 – 1.5 MV/m. Trajectories of the magnetization vector \mathbf{M} after pump excitation under applied electric fields (0 MV/m, 1 MV/m, 1.1 MV/m, and 1.15 MV/m) are shown as spirals on the unit sphere, with colors ranging from dark gold to gold. Red arrows show the direction of the changes \mathbf{M} under applied electric field in the equilibrium position. (c) Calculated normal component of the equilibrium magnetization m_z (black curve) and the amplitude of the laser-induced spin oscillations as a function of applied electric field (dark yellow curve).

4.4 Conclusion

We demonstrate a mechanism allowing an effective control of the efficiency of light-spin coupling in magnets. Applying an electric field of the order of MV/m, we enable an optical excitation of coherent spin waves in an epitaxial film of iron garnet. Such an electrical gating facilitates a spatial control of optically excited spin dynamics with a spatial resolution well-below the diffraction limit when coherent spin waves are excited by light only in the areas where the electric field is applied. We argue that this effect relies on a universal mechanism, which must be present in many other materials where electric-field-induced magnetic anisotropy is strong. The finding practically shows that electric field is a new degree of freedom for fundamental and applied research in the fields of ultrafast magnetism, opto-spintronics, and opto-magnonics. We demonstrate that electric-field control in iron garnets is substantially more efficient and flexible than in 2D van der Waals magnets and similar systems [7]. In contrast, achieving comparable effects in $\text{Cr}_2\text{Ge}_2\text{Te}_6$ requires electric fields several orders of magnitude higher and cryogenic conditions ($T = 10$ K) [7].

In addition, apart from the dominant quadratic response, engineered asymmetry in iron garnets may yield a linear ME contribution [16, 17], while naturally occurring inhomogeneous ME effects could be exploited [18–20]. These effects open new possibilities for enhancing electric control of spin dynamics in magnetic materials with magnetoelectric properties, making them promising systems for continued study of magnetoelectric phenomena and laser-induced spin dynamics.

References

- [1] Bert Koopmans, Pingzhi Li, Hamed Pezeshki, Ece Demirer, Gijs Simons, Yuqing Jiao, Jos van der To, and Reinoud Lavrijsen. Towards on-chip spintronic-photonic integration. In *2024 IEEE International Magnetic Conference-Short papers*, pages 1–2. IEEE, 2024.
- [2] Ernst Abbe. Beiträge zur theorie des mikroskops und der mikroskopischen wahrnehmung. *Archiv für mikroskopische Anatomie*, 9(1):413–468, 1873.
- [3] Ernst HK Stelzer and S Grill. The uncertainty principle applied to estimate focal spot dimensions. *Optics communications*, 173(1-6):51–56, 2000.
- [4] Seagate Technology LLC. Heat-assisted magnetic recording (hamr) technology paper. Technical Paper TP707.1-1712US, Seagate Technology LLC, 2017. Accessed: 2025-05-23.
- [5] Tian-Min Liu, Tianhan Wang, Alexander H Reid, Matteo Savoini, Xiaofei Wu, Benny Koene, Patrick Granitzka, Catherine E Graves, Daniel J Higley, Zhao Chen, et al. Nanoscale confinement of all-optical magnetic switching in tbefco-competition with nanoscale heterogeneity. *Nano letters*, 15(10):6862–6868, 2015.
- [6] Alexey V Kimel and Mo Li. Writing magnetic memory with ultrashort light pulses. *Nature Reviews Materials*, 4(3):189–200, 2019.
- [7] Freddie Hendriks, Rafael R Rojas-Lopez, Bert Koopmans, and Marcos HD Guimarães. Electric control of optically-induced magnetization dynamics in a van der waals ferromagnetic semiconductor. *Nature Communications*, 15(1):1298, 2024.
- [8] A. Dolgikh, D. Afanasiev, V. V. Yurlov, M. V. Logunov, A. K. Zvezdin, and A. V. Kimel. Ultrafast heat-assisted magnetization dynamics in a ferrimagnetic insulator. *Phys. Rev. B*, 107:094424, Mar 2023.
- [9] TT Gareev, NE Khokhlov, L Körber, and AV Kimel. Strongly inhomogeneous spin dynamics induced by ultrashort laser pulses with a gradient intensity profile. *arXiv preprint arXiv:2504.16500*, 2025.
- [10] LALE Landau and Evgeny Lifshitz. On the theory of the dispersion of magnetic permeability in ferromagnetic bodies. *Phys. Z. Sowjetunion*, 8(153):101–114, 1935.
- [11] Thomas L Gilbert. A phenomenological theory of damping in ferromagnetic materials. *IEEE transactions on magnetics*, 40(6):3443–3449, 2004.

- [12] BB Krichevtsov, RV Pisarev, and AG Selitskii. Effect of an electric field on the magnetization processes in the yttrium iron garnet $\text{Y}_3\text{Fe}_5\text{O}_{12}$. *Sov. Phys. JETP*, 74:565–573, 1992.
- [13] N Akulov. Zur quantentheorie der temperaturabhängigkeit der magnetisierungskurve. *Zeitschrift für Physik*, 100(3):197–202, 1936.
- [14] C Zener. Classical theory of the temperature dependence of magnetic anisotropy energy. *Physical Review*, 96(5):1335, 1954.
- [15] CS Davies, KH Prabhakara, MD Davydova, KA Zvezdin, TB Shapaeva, S Wang, AK Zvezdin, A Kirilyuk, Th Rasing, and AV Kimel. Anomalous damped heat-assisted route for precessional magnetization reversal in an iron garnet. *Physical review letters*, 122(2):027202, 2019.
- [16] TH O’dell. An induced magneto-electric effect in yttrium iron garnet. *Philosophical Magazine*, 16(141):487–494, 1967.
- [17] BB Krichevtsov, VV Pavlov, RV Pisarev, and AG Selitsky. Linear magnetoelectric effect in magnetic garnet thin films. *Ferroelectrics*, 161(1):65–71, 1994.
- [18] AP Pyatakov and AK Zvezdin. Flexomagnetoelectric interaction in multiferroics. *The European Physical Journal B*, 71:419–427, 2009.
- [19] Aleksandr P Pyatakov, Alexander Sergeevich Sergeev, Elena Petrovna Nikolaeva, Tatiana Borisovna Kosykh, Alexey Vladimirovich Nikolaev, Konstantin Anatol’evich Zvezdin, and Anatolii K Zvezdin. Micromagnetism and topological defects in magnetoelectric media. *Physics-Uspekhi*, 58(10):981, 2015.
- [20] AP Pyatakov, TT Gareev, AS Kaminskiy, KS Antipin, EP Nikolaeva, DP Kulikova, AS Sergeev, and AV Nikolaev. Magnetoelectricity of chiral micromagnetic structures. *Chirality, Magnetism and Magnetoelectricity: Separate Phenomena and Joint Effects in Metamaterial Structures*, pages 127–146, 2021.

Chapter 5

Electric field control of an antiferromagnetic domain wall in Cr_2O_3

In this chapter we investigate the electric-field-driven motion of antiferromagnetic domain walls in thin Cr_2O_3 films. By positioning a localized tip within a single domain, we observe that applying electric fields of opposite polarities attracts or repels the domain wall, respectively. This behavior, significantly stronger than similar effects in yttrium iron garnet, demonstrates the robust magneto-electric coupling in Cr_2O_3 . Measurements of the magneto-electric response at various temperatures reveal domain-wall hysteresis loops, providing insights into the dynamics and control mechanisms of antiferromagnetic domain walls for energy-efficient spintronics applications.

5.1 Introduction

Magnetoelectric (ME) materials, where magnetization can be induced by applying an electric field or an electric voltage can be generated by an applied magnetic field, are pivotal in the advancement of low-energy spintronic devices and information storage technologies. This coupling between magnetism and electricity in media allows, in particular, nanoscale control of magnetic domains and topological spin textures [1, 2].

Antiferromagnetic (AFM) materials, particularly those exhibiting the ME effect, are of significant interest due to their potential for ultrafast spin dynamics and rapid domain wall (DW) motion. Developing methods to control and detect domain patterns in AFMs and eventually learn how to build an AFM memory has been among the main topics in the booming field of AFM spintronics [3, 4].

Chromium(III) oxide (Cr_2O_3) is a prototypical ME AFM with a Néel temperature $T_N = 307.6$ K [5]. Its crystal structure belongs to the $R\bar{3}c$ space group, featuring spins aligned along the c -axis. The linear ME effect in Cr_2O_3 was first predicted by Dzyaloshinskii [6] and experimentally confirmed by Astrov [5]. Recent advancements have demonstrated the ability to control AFM domains in Cr_2O_3 thin films using electric fields [7]. This control is achieved through the ME effect, where an applied electric field induces a magnetic response, leading to DW motion. Such manipulation is crucial for developing AFM spintronic devices, where information is recorded by applying electric fields [8, 9]. Despite decades of fundamental studies of magnetoelectricity in Cr_2O_3 , the regimes allowing writing information on the AFM by applying an electric field have not been discussed yet.

In this chapter, we investigate the ME response of AFM DWs in Cr_2O_3 . By applying electric fields via a localized tip, we observed either attraction or repulsion of DWs, demonstrating a robust ME coupling. Tuning the temperature of the AFM, we have found a regime allowing us to write AFM bits with an electric field.

5.2 Sample and experimental setup

We used a single crystal of Cr_2O_3 commercially available from MaTecK with a (0001) surface orientation. The crystal has dimensions $5 \times 5 \times 0.5 \text{ mm}^3$. The (0001) surfaces of the crystal were polished with roughness $< 0.01 \mu\text{m}$. The sample was in DC electric E - and magnetic B -fields, applied with a tip and permanent magnet, respectively (for details, see Chapter 2, Experimental Methods). A B -field of magnitude 40 mT is applied along the normal to the sample plane. An E -field is applied with a BeCu non-magnetic tip, wired to a high-voltage (HV) source with an output voltage U in the range of -1.15 kV to $+1.15 \text{ kV}$. The sample is glued onto a copper plate with a 2 mm hole in the center using silver paste. The plate is connected to the neutral terminal of the HV source and placed on the heater to tune the sample's temperature T in the range from 298 K to 306.5 K.

The AFM domain structure of Cr_2O_3 is visualized using the Second Harmonic Generation (SHG) technique, following the method as described by Fiebig *et al.* [10, 11] and in Chapter 2. The pulse spot on the sample has a diameter of about 1 mm. The second harmonic of the probe generated on the sample surface passes the band-pass filter and is captured by a CCD camera with a micro-objective lens. As a result, the AFM domains are visualized with a spatial resolution of $0.6 \mu\text{m}$ [Figure 5.1(a, b)]. We found the sample in a stable two-domain state with a single DW at room temperature.

The hysteresis loop measurement protocol is the following:

1. The high voltage is set to $+1150 \text{ V}$, ensuring that the DW is attached to the tip at 298 K.
2. The voltage is lowered to 0 V and the polarity of the HV source is reversed.
3. The voltage is swept from -50 V to -1150 V and back with steps of 50 V .
4. The polarity is switched to positive and is swept from $+50 \text{ V}$ to $+1150 \text{ V}$ and back.

SHG images are taken on steps 3-4 with a voltage step of 50 V .

5.3 Results and discussion

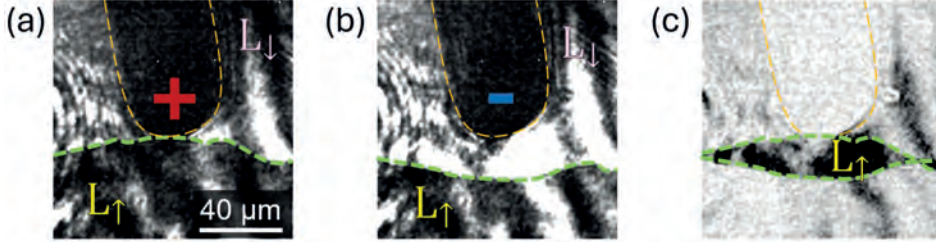


Figure 5.1: AFM domains in Cr_2O_3 visualized with the help of SHG. The black stripe in the upper part of the images is the tip (marked by the orange long-dashed line) with positive + (panel a) and negative – (panel b) electric potential. The domain wall is highlighted with a green dashed line for better visibility. The darker AFM domain corresponds to one orientation of the AFM vector \mathbf{L} and is labeled as L_{\uparrow} . The brighter AFM domain corresponds to the opposite orientation of \mathbf{L} and is labeled as L_{\downarrow} . The positive potential attracts the DW (see panel a), while the negative potential repels it (see panel b). The difference image between panel a and panel b, shown in panel c, shows AFM domain wall displacement under opposite electric field polarities. The measurements were done at room temperature $T = 298$ K, in a magnetic field $B = +40$ mT and with an applied electric field $E = \pm 1.15$ kV.

The simultaneous application of E and B fields sets the DW in motion. In particular, the applied positive E -field ($U > 0$) attracts the DW toward the tip, while a negative E -field ($U < 0$) repels it, when the tip is placed within the bright domain and $B > 0$ [Figure 5.1(a, b)]. Applying electric fields of opposite polarities in different parts of the sample, we found, for instance, a regime shown in Figure 5.2, where the DW is quite obviously pinned, presumably by the two defects indicated by two arrows in the image. The DW under the electric field can be thus modeled as a string stretched between these two defects [Figure 5.1(a, b)]. In this regime, we managed to achieve DW displacement up to $40 \mu\text{m}$. The displacement strongly depends on T .

To evaluate this temperature dependence, we measured the tip-DW distance D as a function of the voltage between the sample and the tip U at different temperatures T . As a result, the function $D(U)$ shows a hysteresis-like behavior (Figure 5.3). The measured loops have several features in the attraction and

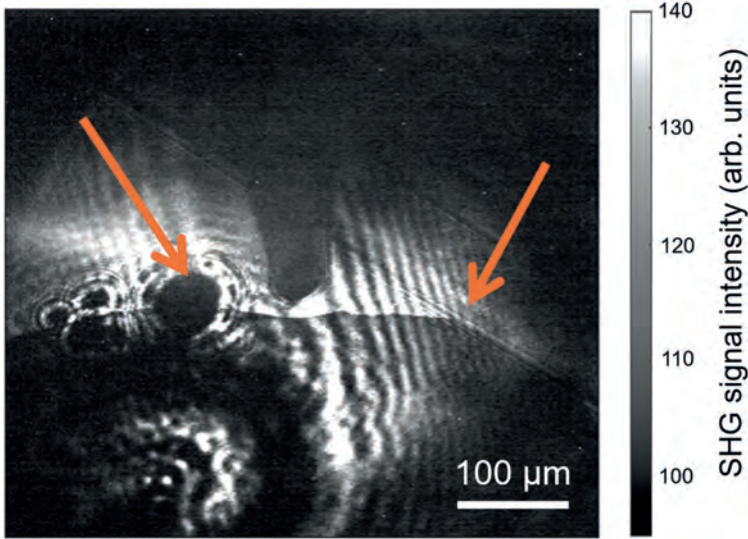


Figure 5.2: Full-sized SHG snapshot. Arrows indicate two defects pinning a DW: a spot burned with a femtosecond laser pulse and a natural crack in the crystal.

repulsion regimes, with a strong dependence on temperature. First, the attraction part of the loops has two steps close to the voltage $U = +1.15$ kV at $298 \text{ K} \leq T \leq 303 \text{ K}$. Next, the second step vanishes for $303 \text{ K} \leq T \leq 306 \text{ K}$, and the loop span tends to zero in this temperature range. However, at $T = 306.5 \text{ K}$ and $U = +1.1$ kV, the DW jumps to the tip, forming a “bulb” and losing the features of a stretched string (see snapshots in Figure 5.5). Finally, in the repulsion part of the loops, D monotonically increases and eventually reaches its maximum with U . At the same time, the displacement D decreases as the sample temperature T approaches the Néel point T_N .

Such an AFM writing is explained as a result of ME coupling in Cr_2O_3 . Due to the coupling, the scalar product $\mathbf{E} \cdot \mathbf{B}$ breaks the degeneracy between two AFM domains with opposite Néel vectors. In fact, it makes one of the AFM more energetically preferable. Changing the polarity of \mathbf{B} and thus the sign of $\mathbf{E} \cdot \mathbf{B}$ can lead to attraction-repulsion behavior of the DW while the voltage U stays the same. It is worth noting that for a ferrimagnetic Néel-type DW in similar experiments with a non-homogeneous E -field [12–15], attraction or repulsion to the tip is also demonstrated. But in this case the DW should be attracted by the tip at $\mathbf{E} \cdot \mathbf{B} > 0$, regardless on which side of the DW the tip is placed (see

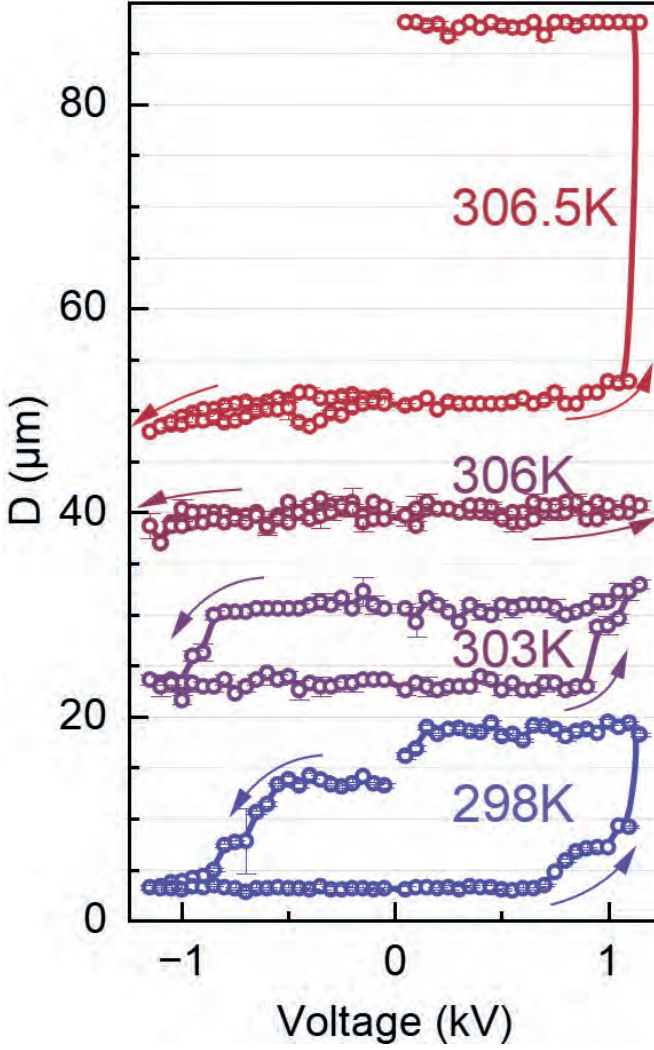


Figure 5.3: Tip-DW distance D as a function of voltage for different temperatures. $\mathbf{B} = +40$ mT.

also Figure 1.3). To exclude this inhomogeneous ME effect, also called the flexo-ME effect [16], we rotated the sample by 180° around the normal of the sample and repeated the experiments when the tip is placed in the dark domain. This set of experiments demonstrates the same behavior of the DW as in the previous

experiment: $\mathbf{E} \cdot \mathbf{B} > 0$ leads to expansion of the dark domain, and $\mathbf{E} \cdot \mathbf{B} < 0$ leads to expansion of the bright domain, regardless on which side of the DW the tip is. Thus, the motion of AFM DWs in Cr_2O_3 very much agrees with the behavior expected for the linear ME, while the flexo-ME can be excluded.

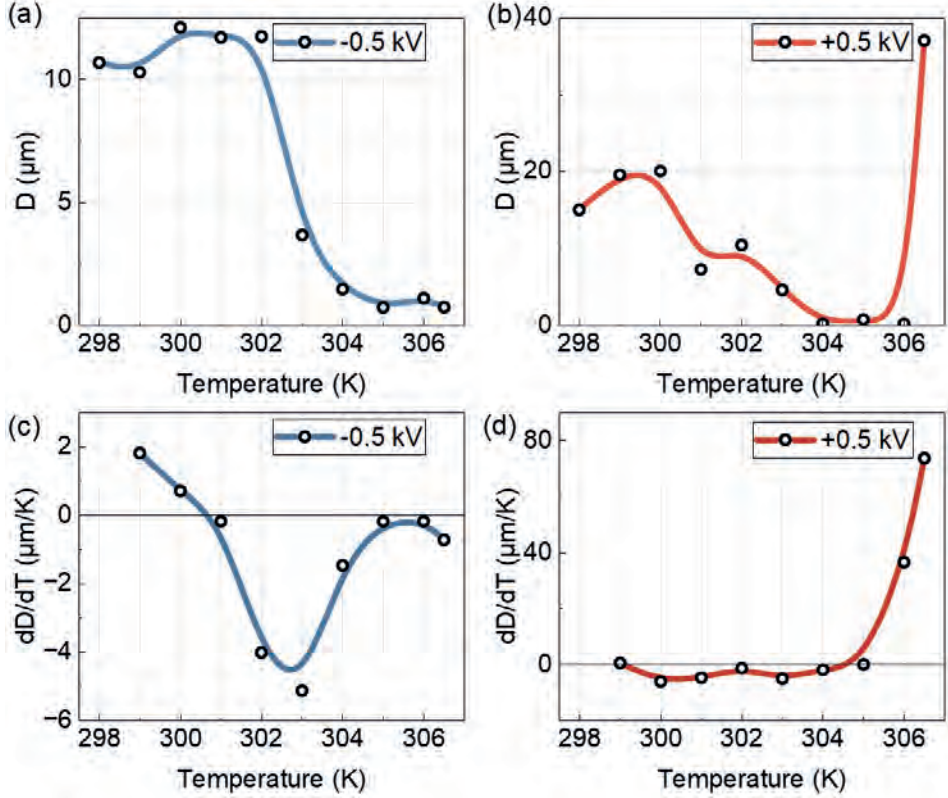


Figure 5.4: Temperature dependence of the hysteresis loop amplitude at a fixed voltage: (a) blue at $U = -0.5$ kV, (b) red at $U = +0.5$ kV. (c) Derivative of the hysteresis loop amplitude with respect to temperature for (c) blue at $U = -0.5$ kV, (d) red at $U = +0.5$ kV. $B = +40$ mT.

To gain deeper insights into the temperature-dependent data, we analyzed the asymmetry in the left and right sections of the $D(U)$ hysteresis loops across all temperature regimes. Specifically, we plotted the hysteresis loop height, $D(T)$, as a function of temperature when the voltage was fixed (± 0.5 kV), and examined the temperature derivative dD/dT to highlight anomalies in the temperature behavior

of the loop (Figure 5.4).

As shown in Figure 5.4a, applying a voltage of -0.5 kV (blue curve), the hysteresis loop height increases in the first regime ($298 \text{ K} \leq T \leq 303 \text{ K}$), as indicated by a positive temperature derivative dD/dT (Figure 5.4b). In the second regime ($303 \text{ K} \leq T \leq 306 \text{ K}$), the height of the hysteresis loop begins to shrink, and this trend continues up to the third regime ($T \approx 306.5 \text{ K}$).

For positive applied voltage of $+0.5$ kV (red curve, Figure 5.4), the behavior is more complex. In the first regime ($298 \text{ K} \leq T \leq 300 \text{ K}$), the loop height also increases. During the second regime ($301 \text{ K} \leq T \leq 306 \text{ K}$), similar to the case of the negative voltage $U < 0$, the loop begins to shrink. However, in the third regime ($T = 306.5 \text{ K}$), e.g., near T_N , the hysteresis loop height increases dramatically, differing sharply from the behavior observed under negative polarity.

To phenomenologically explain the observed DW behavior in the third regime (close to the Néel temperature), we introduce the concept of DW surface tension [17, 18]. The surface tension of a magnetic DW is one of the primary forces governing micromagnetism and acts to suppress the spontaneous nucleation of magnetic structures. In its simplest form, the surface tension of the DW can be expressed as $\sigma \sim \sqrt{AK}$, where A is the exchange stiffness and K is the magnetic anisotropy parameter [18]. As the temperature approaches the Néel point ($T \rightarrow T_N$), the material undergoes a transition to the paramagnetic state, and both A and K tend to zero. Consequently, the surface tension σ also vanishes ($\sigma = 0$). The behavior of the DW near T_N in the experiment (Figure 5.5) indicates that its surface tension drastically decreases near the critical point. The signature of it is the shape of the DW: at $T \geq 306.4 \text{ K}$ the DW represents a bulb shape at $|U| > 0$ [Figure 5.5(a,c)], not a “string”-shape (Figure 5.1).

To explore the AFM DW behavior in more detail, we performed experiments with a moving tip while applying an electric field. At $T = 306.4 \text{ K}$, moving the tip under an applied voltage ($U = -1.15 \text{ kV}$) results in a clear displacement of the DW [Figure 5.5(a)]. However, once the electric field is switched off ($U = 0 \text{ V}$), the DW returns to its initial position [Figure 5.5(b)], indicating that the surface tension is still nonzero ($\sigma \neq 0$). When the temperature is increased by only 0.1 K to $T = 306.5 \text{ K}$, closer to the Néel temperature, the DW behaves differently. In this case, the DW surface tension vanishes ($\sigma = 0$), allowing the tip to “draw” a stable domain pattern with reversed orientation of the Néel vector under the same electric field conditions [Figure 5.5(c)]. Even after turning off the electric field, the drawn pattern remains preserved [Figure 5.5(d)]. These observations indicate that AFM bits can potentially be written by locally applying an electric field near the Néel temperature, where the domain wall surface tension vanishes.

We also investigated how changes in the polarity of the magnetic field affect DW motion. When both the electric field and the magnetic field have positive polarity, the DW is attracted, resulting in the growth of the dark domain. When the polarity of the electric field is reversed (negative) while the magnetic field

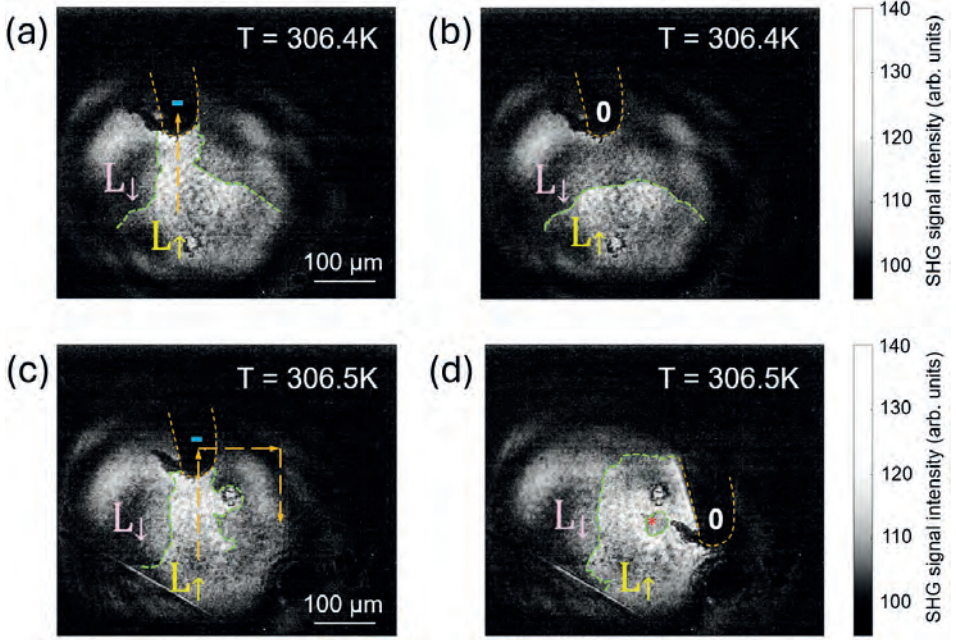


Figure 5.5: AFM domains imaged via SHG under applied electric fields at 306.4 K (a, b) and 306.5 K (c, d). The orange dashed line indicates the tip position; orange arrows (a, c) show its movement. The green dashed line marks the AFM DW. Domains with opposite orientations of the AFM vector \mathbf{L} are labeled as L_{\uparrow} and L_{\downarrow} . DW shape during ($U = -1.15$ kV) (a) and after ($U = 0$ V) (b) E-field-induced displacement. (c) DW configuration after tip movement at 306.5 K with $U = -1.15$ kV. (d) After switching off the field, the drawn L_{\uparrow} pattern remains. In the region marked “*”, L_{\downarrow} persists, while the surrounding area has switched to L_{\uparrow} . A magnetic field of $B = +40$ mT is applied in-plane of the sample.

remains positive, the DW is repelled, leading to the growth of the bright domain. Conversely, when the polarity of the magnetic field is switched to negative, the AFM DW exhibits the opposite behavior. Specifically, with a positive electric field and a negative magnetic field, the DW is repelled, and the bright domain grows. For a negative electric field and a negative magnetic field, the DW is attracted, resulting in the growth of the dark domain. No displacement of the DW is observed in the absence of a magnetic field. A summary of these results is provided in Table

5.1. This behavior is consistent with the expectations of the linear ME mechanism, which predicts domain wall displacement proportional to the scalar product $\mathbf{E} \cdot \mathbf{B}$.

	$E > 0$	$E = 0$	$E < 0$
$B > 0$	Dark domain grows	No movement	Bright domain grows
$B = 0$	No movement	No movement	No movement
$B < 0$	Bright domain grows	No movement	Dark domain grows

Table 5.1: Behavior of AFM domains in a combination of E and B fields.

This effect is significantly stronger compared to similar effects observed in yttrium iron garnet (YIG), where DW motion is driven by the inhomogeneous ME effect [12, 13, 19, 20].

5.4 Conclusion

In this chapter, we demonstrated that AFM DWs in Cr_2O_3 can be effectively controlled by a localized electric field in the presence of a magnetic field. We observed that the sign of the scalar product $\mathbf{E} \cdot \mathbf{B}$ determines whether the DW is attracted or repelled by the tip. This displacement behavior is fully consistent with the predictions of the linear ME effect.

Temperature-dependent measurements revealed three distinct regimes of domain wall dynamics, with the most remarkable behavior occurring close to the Néel temperature T_N . In this regime, the domain wall is no longer restored to its initial position after switching off the electric field. Instead, stable writing of anti-ferromagnetic domains becomes possible by moving the tip – effectively enabling direct patterning of AFM bits with high spatial resolution.

The demonstrated mechanism operates without relying on current-driven processes, making it a potentially highly energy-efficient approach for manipulating AFM domains in next-generation spintronic devices.

References

- [1] Manfred Fiebig. Revival of the magnetoelectric effect. *Journal of Physics D: Applied Physics*, 38(8):R123–R152, 2005.
- [2] Nicola A Spaldin and Ramamoorthy Ramesh. Advances in magnetoelectric multiferroics. *Nature Materials*, 18(3):203–212, 2019.
- [3] Tomas Jungwirth, Xavier Marti, Peter Wadley, and Jairo Wunderlich. Antiferromagnetic spintronics. *Nature Nanotechnology*, 11(3):231–241, 2016.
- [4] Vincent Baltz, Aurelien Manchon, Maxim Tsoi, Takahiro Moriyama, Teruo Ono, and Yaroslav Tserkovnyak. Antiferromagnetic spintronics. *Reviews of Modern Physics*, 90(1):015005, 2018.
- [5] D. N. Astrov. Sov. phys. jexp. 13:729, 1961.
- [6] IE Dzyaloshinskii. On the magneto-electrical effect in antiferromagnets. *Soviet Physics JETP*, 10(3):628–629, 1959.
- [7] Yu Shiratsuchi, Kentaro Toyoki, and Ryoichi Nakatani. Magnetoelectric control of antiferromagnetic domain state in Cr_2O_3 thin film. *Journal of Physics: Condensed Matter*, 33(24):243001, 2021.
- [8] Pavel Borisov, Andreas Hochstrat, Xiaoli Chen, and Wolfgang Kleemann. Spin valve effect in Cr_2O_3 -based heterostructures. *Physical Review Letters*, 94(11):117203, 2005.
- [9] KD Belashchenko, SI Andreev, and M van Schilfgaarde. First-principles analysis of the magnetoelectric effect in Cr_2O_3 . *Physical Review B*, 94(14):144403, 2016.
- [10] M. Fiebig, D. Fröhlich, B. B. Krichevstov, and R. V. Pisarev. Second harmonic generation and magnetic-dipole-electric-dipole interference in antiferromagnetic Cr_2O_3 . *Phys. Rev. Lett.*, 73:2127–2130, Oct 1994.
- [11] Manfred Fiebig, D Fröhlich, G Sluyterman v. L, and RV Pisarev. Domain topography of antiferromagnetic Cr_2O_3 by second-harmonic generation. *Applied Physics Letters*, 66(21):2906–2908, 1995.
- [12] RM Vakhitov, RV Solonetsky, VR Gurjanova, AR Nizjamova, DA Sechin, TT Gareev, and AP Pyatakov. Magnetic-field tuning of domain-wall multiferroicity. *Physical Review B*, 104(14):144407, 2021.
- [13] Nikolai E Khokhlov, Anastasiya E Khramova, Elena P Nikolaeva, Tatyana B Kosykh, Alexey V Nikolaev, Anatoly K Zvezdin, Alexander P Pyatakov, and Vladimir I Belotelov. Electric-field-driven magnetic domain wall as a microscale magneto-optical shutter. *Scientific reports*, 7(1):264, 2017.

- [14] A.P. Pyatakov, V.I. Belotelov, D.P. Kulikova, N.E. Khokhlov, Z.A. Pyatakova, and A.V. Nikolaev. Magnetoelectricity in topological magnetic textures. *Journal of Magnetism and Magnetic Materials*, 440:60–62, 2017. Selected papers from the sixth Euro-Asian Symposium “Trends in Magnetism” (EASTMAG-2016).
- [15] DI Khomskii. Multiferroics and beyond: electric properties of different magnetic textures. *Journal of Experimental and Theoretical Physics*, 132:482–492, 2021.
- [16] AP Pyatakov and AK Zvezdin. Flexomagnetoelectric interaction in multiferroics. *The European Physical Journal B*, 71:419–427, 2009.
- [17] Lev Davidovich Landau, John Stewart Bell, MJ Kearsley, LP Pitaevskii, EM Lifshitz, and JB Sykes. *Electrodynamics of continuous media*, volume 8. elsevier, 2013.
- [18] Daria P Kulikova, Timur T Gareev, Elena P Nikolaeva, Tatyana B Kosykh, Alexey V Nikolaev, Zoya A Pyatakova, Anatoly K Zvezdin, and Alexander P Pyatakov. The mechanisms of electric field-induced magnetic bubble domain blowing. *physica status solidi (RRL)–Rapid Research Letters*, 12(6):1800066, 2018.
- [19] AS Logginov, GA Meshkov, AV Nikolaev, EP Nikolaeva, AP Pyatakov, and AK Zvezdin. Room temperature magnetoelectric control of micromagnetic structure in iron garnet films. *Applied Physics Letters*, 93(18), 2008.
- [20] Aleksandr P Pyatakov and Anatolii K Zvezdin. Magnetoelectric and multiferroic media. *Physics-Uspeski*, 55(6):557, 2012.

Chapter 6

Optical excitation of coherent THz dynamics of the rare-earth lattice through resonant pumping of an $f - f$ electronic transition in the complex perovskite DyFeO_3

Resonant pumping of the electronic $f - f$ transitions in the orbital multiplet of Dy^{3+} ions in the complex perovskite DyFeO_3 is shown to impulsively launch THz lattice dynamics corresponding to the B_{2g} phonon mode, which is dominated by the motion of Dy^{3+} -ions. The findings, supported by symmetry analysis and DFT calculations, not only provide a novel route for highly selective excitation of the RE crystal lattices but also establish important relationships between the symmetry of the electronic and lattice excitations in complex oxides.

Adapted from: [T.T. Gareev](#), A. Sasani, D.I. Khusyainov, E. Bousquet, Z.V. Gareeva, A.V. Kimel, and D. Afanasiev, “Optical Excitation of Coherent THz Dynamics of the Rare-Earth Lattice through Resonant Pumping of $f - f$ Electronic Transition in a Complex Perovskite DyFeO_3 ”, *Physical Review Letters*, **133**, 246901 (2024).

6.1 Introduction

Optical control of crystal lattices using femtosecond pulses of light has gained significant attention as an efficient way for controlling and probing functional properties of various macroscopic ordered phases of matter on an ultrafast timescale. Various mechanisms for optical driving of ultrafast lattice excitations, both in the form of acoustic and optical phonons, have been recently proposed and implemented. These mechanisms include excitation of phonons through laser-induced heating [1–3], impulsive stimulated Raman scattering (ISRS) [4–6], displacive excitations facilitated by the electronic deformation potential [7], photostriction [8], direct driving in multiferroics [9], as well as recently discovered resonant ionic Raman scattering [10]. Application of optically generated lattice distortions to ordered phases has recently led to such spectacular phenomena as ultrafast demagnetization [11, 12], lattice-driven switching of spins [13] and ferroelectric polarizations [14, 15], metal-insulator phase transitions [16, 17] as well as the generation of transient ferroelectricity [18–20], magnetism [21, 22], and even superconductivity up to room temperature [23]. Furthermore, recent theory anticipates that the optical driving of phonons can lead to the emergence of magnetization even in materials with no existing spin structure, an effect called dynamic multiferroicity [24–26].

Rare-earth (RE) perovskites (RMO_3 , R^{3+} =rare-earth, M^{3+} =transition metal ion) offer a remarkable opportunity to explore the relationships between structural, transport, and magnetic properties [27–29]. In these compounds, the size and interionic spacing of the RE ions are crucial in determining key properties such as metallicity and Jahn-Teller orbital ordering as well as overall stability of the perovskite unit cell [30]. Many magnetic properties of RMO_3 are primarily controlled by an electronic structure of the R^{3+} ion and its interaction with the local crystalline environment. This is particularly evident in RE orthoferrites (RFeO_3), where the anisotropic exchange interaction between R^{3+} and Fe^{3+} spins not only sets up the magnetic single-ion anisotropy of the latter but also triggers spontaneous spin-reorientation phase transitions and, in some cases, a surge of the magnetoelectric coupling [26–29, 31].

Among all the RE orthoferrites, DyFeO_3 stands out as a multiferroic [21, 32–36] in which, at temperatures below the magnetic ordering of the Dy^{3+} spins (<4 K), the electronic configuration of the Dy^{3+} ions promotes lattice distortions, leading to the emergence of a multiferroic state hosting exotic hybridized spin-lattice excitations named electromagnons [37]. Here we explore how resonant pumping of electronic transitions in the Dy^{3+} ions, and thus effective changes of the electronic configuration of the ions, can impulsively excite lattice dynamics on the picosecond time scale. Continuously varying the pump photon energy across various electronic excitations of the Dy^{3+} ions [38], we identify one electronic excitation responsible

for the excitation of a pair of THz frequency phonons that are dominated by the Dy^{3+} ions. Our findings, supported by a theoretical description, suggest that optical perturbation of the electronic states of the RE ion is considered as a primary source of the light-driven coherent dynamics of the RE lattice.

6.2 Sample and scheme of the experiment

DyFeO_3 crystallizes in a distorted perovskite structure having orthorhombic space group $Pnma$ with four formulae and therefore twenty atoms per unit cell, see Figure 6.1a. The structure is characterized by rotations and tilts of the FeO_6 octahedra and the location of Dy^{3+} ions in sites of low point group symmetry Cs. Two independent sets of phonons, Raman- and infrared-active, represent the elementary excitations of the centrosymmetric DyFeO_3 lattice. The Raman-active optical phonons of the DyFeO_3 have A_g , B_{1g} , B_{2g} , and B_{3g} symmetries and frequencies spread over the 3.40 – 19.17 THz range [39]. The infrared-active phonons have B_{1u} , B_{2u} , and B_{3u} symmetries and frequencies spread over the 2.54 – 19.55 THz range [40]. While the high-frequency phonons (>9 THz) are dominated by the vibrations of the light mass O^{2-} ions, the low-frequency phonons (<6 THz) are dominated by vibrations of the heavy mass Dy^{3+} ions [38].

The interaction between near-infrared and visible light and DyFeO_3 is governed by electronic excitations of Fe^{3+} and Dy^{3+} ions, known as $d-d$ and $f-f$ transitions, respectively. When these transitions are optically stimulated, electrons undergo shifts within their respective d - and f -orbitals. The optical absorption spectrum of DyFeO_3 , depicted in Figure 6.1b, reveals that Fe^{3+} ions exhibit two weak and broad absorption $d-d$ bands at photon energies of 1.2 and 1.8 eV [30, 32, 41]. These absorptions are accompanied by many significantly narrower spectral lines, corresponding to localized atomic-like $f-f$ orbital transitions of the Dy^{3+} ions [38].

The studied sample is a c -cut of DyFeO_3 single crystal having a thickness of about 100 μm . To study the effect of the optical excitation on the lattice dynamics, we carried out a time-resolved pump-probe experiment in which the sample was excited using a strong pump pulse and the subsequent lattice dynamics were tracked using a time-delayed weak probe pulse, see Figure 2.3 in Chapter 2. Our light source was a Ti:Sapphire regenerative amplifier, producing linearly polarized ultrashort ($\Delta t \sim 50$ fs) laser pulses at a photon energy of 1.55 eV and a repetition rate of 1 kHz. To acquire the possibility of tuning the photon energy of the pump pulses and thus to be able to selectively address both $f-f$ resonances of Dy^{3+} ions and $d-d$ resonances of Fe^{3+} ions, we employed a commercially available (TOPAS, Light Conversion) optical parametric amplifier (OPA). This allowed continuous tuning of the pump photon energy in the range of 0.5 – 1.3 eV. To track the dynamics of the crystalline lattice, we used linearly polarized probe

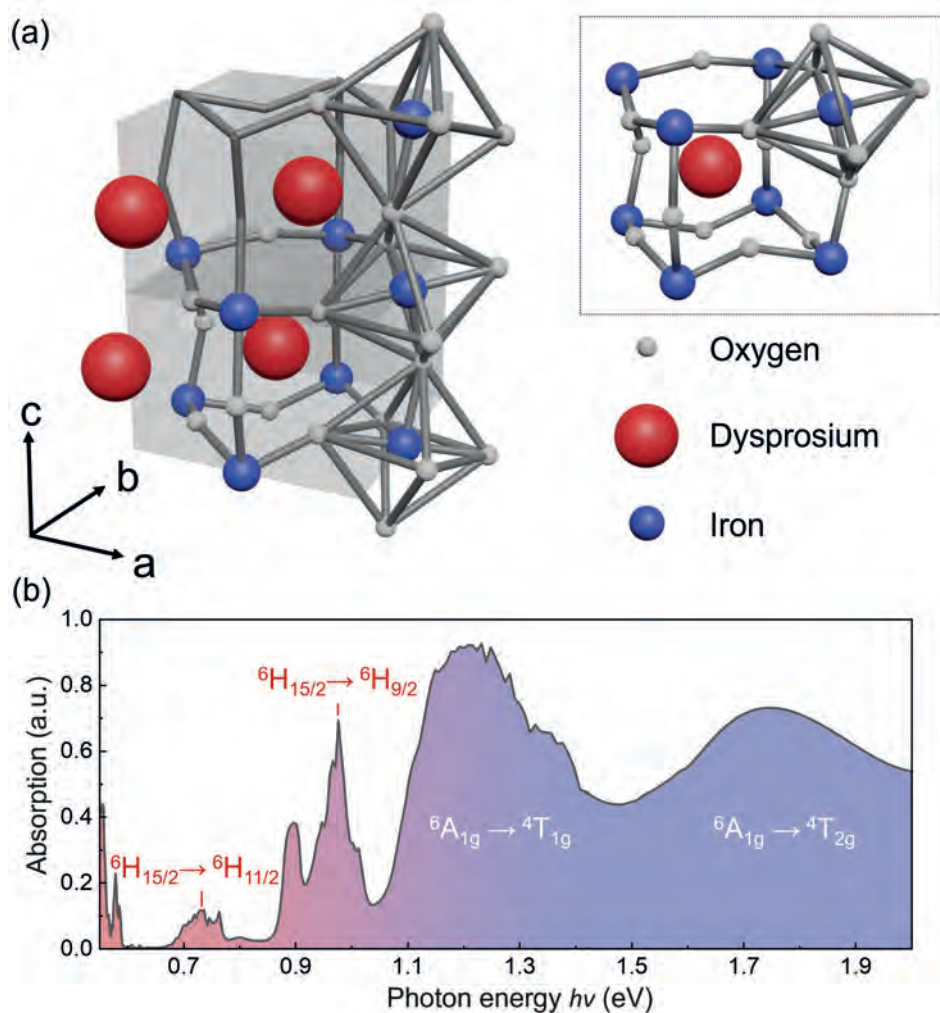


Figure 6.1: (a) A schematic showing an orthorhombic unit cell of DyFeO_3 . The grey, red, and blue spheres represent oxygen, dysprosium, and iron atoms, respectively. The inset exemplifies a pseudocubic unit cell of DyFeO_3 . Crystallographic axes and their directions are indicated by arrows a , b , and c . (b) Absorption spectrum of DyFeO_3 in the near-infrared and visible spectral ranges. The relevant absorption lines corresponding to the $d-d$ (${}^6\text{A}_{1g} \rightarrow {}^4\text{T}_{1g}$ and ${}^6\text{A}_{1g} \rightarrow {}^4\text{T}_{2g}$) and $f-f$ (${}^6\text{H}_{15/2} \rightarrow {}^6\text{H}_{11/2}$ and ${}^6\text{H}_{15/2} \rightarrow {}^6\text{H}_{9/2}$) transitions of the Fe^{3+} and Dy^{3+} ions, respectively, are marked on the graph.

pulses at the photon energy of 1.55 eV. These pulses are time-delayed with the help of a mechanical delay line and enable measurements of the rotation of the probe polarization plane $\Delta\theta$ as a function of the pump-probe time delay. The rotation reflects the pump-induced changes to the linear birefringence and was shown to be sensitive to the intrinsically anisotropic dynamics of phonons [42–44].

6.3 Results and discussion

Figure 6.2a shows the time-resolved traces of the ultrafast coherent dynamics of the pump-induced polarization rotation $\Delta\theta$ measured in DyFeO₃ for a broad range of temperatures T from 10 K to 300 K. It is seen that the waveforms in Figure 6.2a have a rather complex form with a clear beating pattern. To reveal the spectral content of the measured signals, we performed a Fast Fourier Transform (FFT) which exposes two distinct spectral modes at frequencies of $f_1 = 4.27$ THz and $f_2 = 4.93$ THz and comparable amplitudes at low $T = 10$ K. Figure 6.2b shows that the frequencies of these modes do not change significantly with T . In contrast, their amplitudes, while remain measurable up to the room temperature, demonstrate a significant and mode dependent suppression upon temperature increase. We also observed pump-induced coherent spin dynamics at a much lower frequency of 0.19 THz, corresponding to one of the spin precession modes, see Figure 6.3. This frequency aligns well with previously reported values [45].

To establish the origin of the observed modes we performed *ab-initio* density-functional theory (DFT) calculations of the lattice dynamics in DyFeO₃ (for details see [46]). The results show that the frequencies of the observed oscillations f_1 and f_2 closely match those corresponding to the Raman active phonons having A_g and B_{2g} symmetries, respectively (Appendix A.1, Table A.1). Their eigenmodes are shown in Figure 6.4, where one can see that both are dominated by the antiphase dynamics of the adjacent Dy³⁺ ions. The orthorhombic *Pnma* structure exhibits 24 Raman-active vibrational modes [39, 47], including A_g and B_{2g} , as observed in our experiments. The optical pump pulse, with a bandwidth $\Delta f = (\Delta t)^{-1} \sim 20$ THz, can induce coherent dynamics of these modes through the Impulsive Stimulated Raman Scattering (ISRS) process [4–6]. To investigate whether this Raman-type generation mechanism is responsible for exciting coherent lattice dynamics, we carried out a pump polarization study [4]. Such approach allows to access the efficiency of the optical phonon excitation and can be directly compared to the selection rules provided by the Raman polarizability tensors. In Figure 6.5, we demonstrate that the orientation of the pump polarization plane significantly influences the amplitudes of the phonon modes. The A_g mode reaches its maximum amplitude when the pump angle aligns with the crystallographic a and b axes (Figure 6.5a). In contrast, the B_{2g} mode exhibits maximum amplitude when the pump polarization angle α is approximately at 45 degrees relative to the

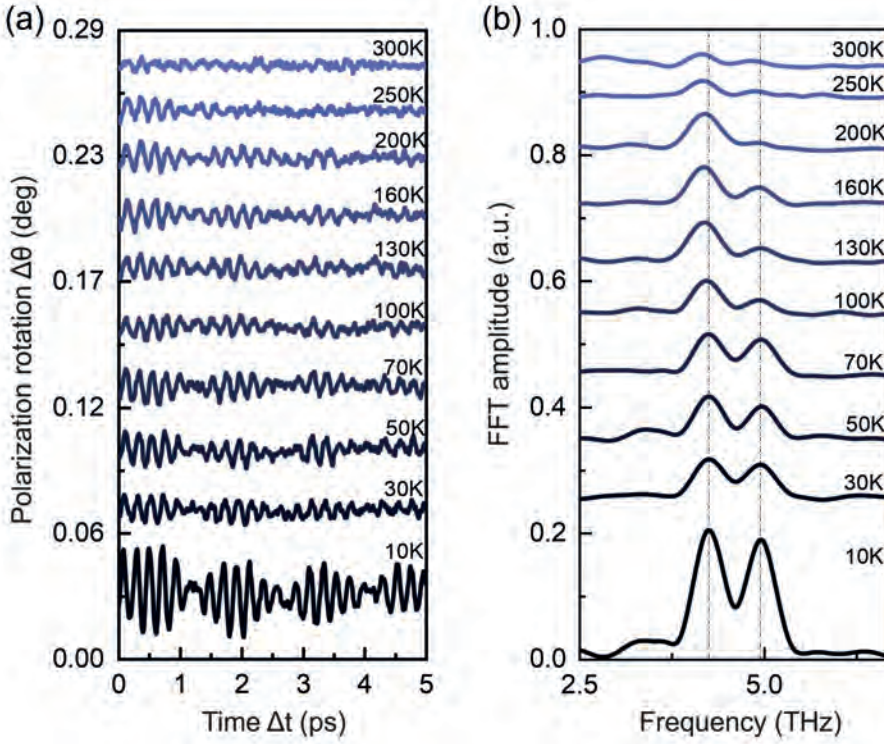


Figure 6.2: (a) Time-resolved rotation of the probe polarization plane $\Delta\theta$ showing dynamics of coherent phonons excited by an ultrashort laser pump pulse across a broad range of temperatures from 10 K to 300 K. The pump is linearly polarized with a phonon energy $h\nu = 0.9$ eV and fluence of about 1 mJ/cm^2 . (b) Fast Fourier Transforms (FFTs) of the corresponding time traces that reveal two distinct peaks at frequencies $f_1 = 4.27$ THz and $f_2 = 4.93$ THz.

crystallographic axes (Figure 6.5b).

Femtosecond pulses of light are known to drive coherent dynamics of optical phonons through a process known as Impulsive Stimulated Raman Scattering (ISRS) [44]. This excitation mechanism does not necessarily rely on specific optical resonances. Consequently, it is largely independent of the energy of the driving phonon, enabling excitation to occur even within the optical transparency region of a medium. The only condition is that the pulse duration is short compared to

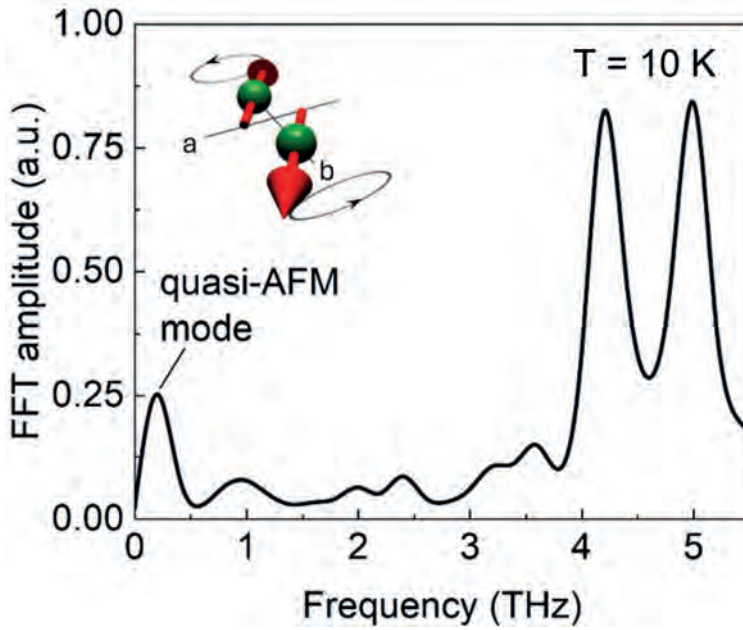


Figure 6.3: Fast Fourier Transform (FFT) of the time trace from the pump-probe experiment from Figure 6.1a at the temperature 10 K, including the quasi-AFM mode at approximately 0.19 THz. The amplitude of the quasi-AFM mode is about 70 % lower compared to the amplitudes of the 4.27 THz and 4.93 THz modes. The pump photon energy is 0.71 eV, and the probe photon energy is 1.55 eV. The fluence of the pump is approximately 1 mJ/cm². Top inset: schematic representation of the corresponding spin precession.

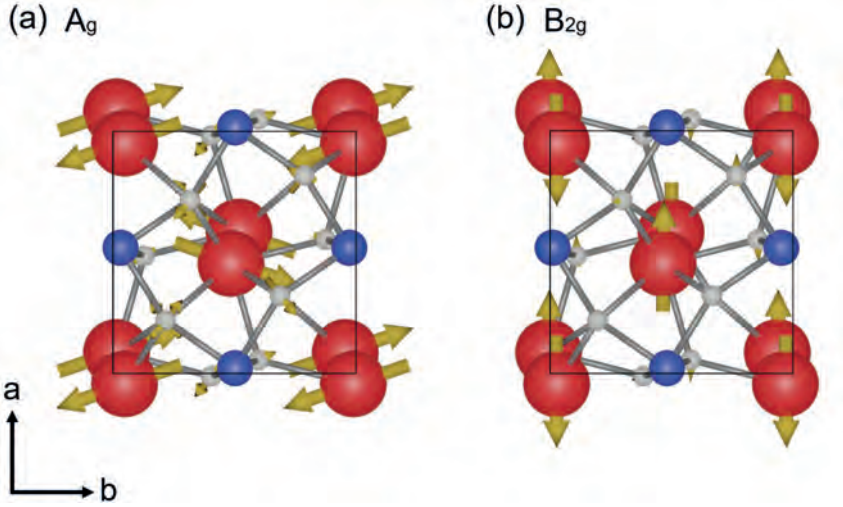


Figure 6.4: Eigenvectors of the (a) A_g and (b) B_{2g} phonon modes excited by the pump pulse. The magnitude of the atomic displacements is qualitatively described by the length of the yellow arrows. a and b are crystallographic axes of DyFeO_3 .

the characteristic periods of the lattice vibrations.

Following the approach similar to the one in Ref. [4], the equation of motion for the lattice reads:

$$\ddot{Q} + \Omega^2 Q = F(t), \quad (6.1)$$

where Q is a generalized coordinate of a phonon mode oscillating at angular frequency Ω , and F is a driving force that can be expressed as:

$$F = E_i R_{ij} E_j \quad (6.2)$$

$E_{i,j}$ are the electric field components of the pump pulse along the i - and j - crystal axes, and R_{ij} is a Raman polarizability tensor of the considered phonon mode.

The first A_g phonon mode observed in our experiments is characterized by the Raman polarizability tensor, that reads [48]:

$$R(A_g) = \begin{pmatrix} a & 0 & 0 \\ 0 & b & 0 \\ 0 & 0 & c \end{pmatrix}, \quad (6.3)$$

where a , b , and c are phenomenological parameters.

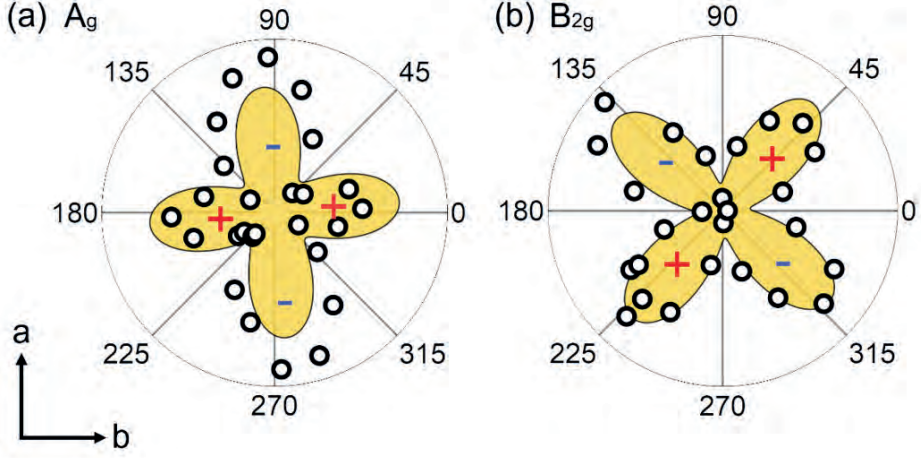


Figure 6.5: Amplitude of the pump-excited coherent A_g (a) and B_{2g} (b) phonon modes for various orientations of the pump polarization planes. For (a) the shade region denotes fitted polarization dependence with respect to Raman selection rules for this mode (formula 6.5, $\frac{b}{a} = 1.69$). For (b) the shade region is a guide to the eye. For all the measurements the polarization angle of the probe pulse is set to 45° relative to the a -crystal axis. The sign “+” and “-” plotted along the lobes of the dependencies indicate the relative phase of the observed oscillations. All the measurements are performed at a temperature of 80 K.

The electric field \mathbf{E} of the linearly polarized pump pulses incident along the z -crystal axis can be expressed as follows:

$$\mathbf{E} = (E_x, E_y, E_z) = (E_0 \cos \alpha, E_0 \sin \alpha, 0), \quad (6.4)$$

E_0 is the amplitude of the electric field component of light, α is the angle the pump polarization forms with the crystallographic x -axis. One can see that the driving force $F(A_g)$ leading to excitation of the A_g mode reads:

$$F(A_g) = aE_x^2 + bE_y^2 + cE_z^2 = aE_0^2(\cos^2 \alpha + \frac{b}{a} \sin^2 \alpha) \quad (6.5)$$

showing that the optical excitation A_g strongly depends on the orientation of the pump polarization plane relative to the crystal axes, i.e. following Raman selection rules. Fitting the experimentally observed polarization dependence shown in

Figure 6.5a to Eq. 6.5 gives good agreement between experiment and theory when $\frac{b}{a} = 1.69$, see Figure 6.5a. This agreement suggests ISRS as a possible mechanism for the coherent excitation of the A_g phonon mode.

The second B_{2g} phonon mode observed in our experiments is characterized by the Raman polarizability tensor, that reads [48]:

$$R(B_{2g}) = \begin{pmatrix} 0 & 0 & e \\ 0 & 0 & 0 \\ e & 0 & 0 \end{pmatrix}, \quad (6.6)$$

where e is a phenomenological parameter. One can see that the driving force $F(B_{2g})$ leading to excitation of the B_{2g} mode reads:

$$F(B_{2g}) = 2eE_xE_z \equiv 0 \quad (6.7)$$

implying that the B_{2g} phonon mode cannot be excited in the geometry of our experiment as $E_z \equiv 0$.

While the Raman polarizability tensor of the $Pnma$ space group effectively characterizes the polarization dependence of the fully symmetric A_g mode, it falls short in describing the B_{2g} mode. In our experimental geometry, the Raman selection rules prohibit the excitation of this mode. This discrepancy suggests that the symmetry of the undisturbed crystal lattice of DyFeO_3 is insufficient to describe the optical excitation of the B_{2g} mode, and some other mechanisms, different from the conventional Raman scattering should be at play.

To investigate the actual mechanism behind the optical excitation of the B_{2g} phonon mode and its relation to the orbital state of the Dy^{3+} ions we next studied the efficiency of the B_{2g} phonon excitation as a function of the pump photon energy $h\nu$. To achieve this goal we measure its amplitude as a function of $h\nu$ across a pair of low-energy electronic transitions within the manifold of orbital states of Dy^{3+} ions: ${}^6\text{H}_{15/2} \rightarrow {}^6\text{H}_{11/2}$ ($h\nu = 0.73$ eV) and ${}^6\text{H}_{15/2} \rightarrow {}^6\text{H}_{9/2}$ ($h\nu = 1$ eV) [38]. The energy of these transitions lies right below the lowest energy of the $d-d$ orbital excitations of the Fe^{3+} ions ${}^6\text{A}_{1g} \rightarrow {}^4\text{T}_{1g}$ and ${}^6\text{A}_{1g} \rightarrow {}^4\text{T}_{2g}$ (Figure 6.1b) [38, 49], and thus not only affords to single out excitation of the RE ions from their transition metal counterpart but also offers the possibility of comparing efficiencies of the considered $f-f$ resonances. Figure 6.6a shows that the amplitude of the phonon oscillations peaks when $h\nu \approx 0.69$ eV closely matching the energy of the ${}^6\text{H}_{15/2} \rightarrow {}^6\text{H}_{11/2}$ transitions. We also find that the amplitude of the excited phonon mode scales linearly with the fluence of the pump pulse, Figure 6.6b. Although the amplitude of the B_{2g} mode remains finite, no peak is observed when the energy of the pump photon matches the ${}^6\text{H}_{15/2} \rightarrow {}^6\text{H}_{9/2}$ transition, even so, the absorption line corresponding to this transition is an order of magnitude stronger than that of the ${}^6\text{H}_{15/2} \rightarrow {}^6\text{H}_{11/2}$ transition. Moreover, increasing $h\nu$ towards the even stronger ${}^6\text{A}_{1g} \rightarrow {}^4\text{T}_{1g}$ orbital $d-d$ transition of Fe^{3+} ions does not lead to any pronounced enhancement of the phonon amplitude.

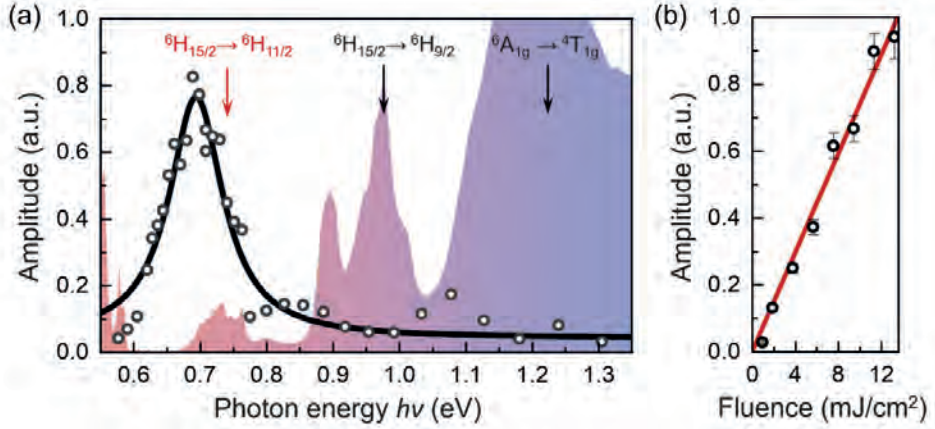


Figure 6.6: (a) The amplitude of the optically excited B_{2g} phonon mode as a function of the pump photon energy $h\nu$. The solid line is a guide to the eye. The shadow background is the optical absorption spectrum of DyFeO_3 in the infrared spectral range. The pump spot size was constant during the measurements, and the fluence was about $1 \text{ mJ}/\text{cm}^2$. The absorption peaks are marked with the corresponding $f - f$ and $d - d$ electronic transitions of the Dy^{3+} and Fe^{3+} ions, respectively. (b) The amplitude of the B_{2g} phonon mode scales linearly with the fluence of the pump pulse. Pump photon energy is 0.69 eV . All measurements were done at a temperature of 80 K .

To unveil the microscopic mechanism behind coherent excitation of the RE lattice in DyFeO_3 and the role of the ${}^6\text{H}_{15/2} \rightarrow {}^6\text{H}_{11/2}$ transition, we consider the ground and excited electronic states of the Dy^{3+} ions using the Clebsch–Gordan coefficients (for details, see [46]). The coefficients are normally used to describe the $4f$ electronic configuration of the RE ions in terms of total angular momentum eigenstates. These eigenstates have the form $|L; M_L; S; M_S\rangle$, where $L = \sum_i l_i$ and $S = \sum_i s_i$ are the sum over orbital l and s spin angular momenta of the individual $4f$ electrons on the RE site, M_L and M_S are orbital and spin angular momenta along the quantization axis, respectively. The ${}^6\text{H}_{15/2}$ ground state of Dy^{3+} ions can be presented by a single eigenstate $|5; 5; 5/2; 5/2\rangle$, schematically shown in Figure 6.7. The ${}^6\text{H}_{11/2}$ excited state of Dy^{3+} can be represented by a linear combination of the three individual eigenstates $|5; 5; 5/2; 1/2\rangle$, $|5; 4; 5/2; 3/2\rangle$, and $|5; 3; 5/2; 5/2\rangle$:

$${}^6\text{H}_{11/2} = 3\sqrt{\frac{5}{91}}|5; 5; 5/2; 1/2\rangle - 6\sqrt{\frac{1}{91}}|5; 4; 5/2; 3/2\rangle + \sqrt{\frac{10}{91}}|5; 3; 5/2; 5/2\rangle \quad (6.8)$$

where the multipliers in front of the states are the Clebsch–Gordan coefficients, which have the meaning of a probability amplitude. The change in spin angular momentum ΔM_S does not impact the spatial charge distribution of the RE electronic wavefunctions. Consequently, transition to the $|5; 5; 5/2; 1/2\rangle$ state, although characterized by the highest probability, cannot launch the lattice dynamics. Hence, our focus lies on orbital states that involve a change in the projection of the angular momentum ΔM_L . Equation 6.8 illustrates that transitions to the last two excited total angular momentum states, $|5; 4; 5/2; 3/2\rangle$ and $|5; 3; 5/2; 5/2\rangle$, result in $\Delta M_L = 1$ and $\Delta M_L = 2$, respectively.

Remarkably, these transitions can be elucidated by a shift in the orbital state of a single electron in a $4f^9$ configuration of Dy^{3+} ion and can be conveniently described using a single spherical harmonic Y_m^l , where l represents the electron’s angular momentum and m its projection. We first highlight the case of $\Delta M_L = 1$, as it is characterized by a larger Clebsch–Gordan coefficient and thus higher transition probability. In this scenario the electron wavefunction undergoes a transformation from $Y_2^3 \rightarrow Y_1^3$, as depicted in Figure 6.7a. Analysis reveals that such a change in electronic symmetry facilitates a lattice distortion leading to an excitation of phonons characterized by the B_{3g} , B_{2g} symmetries (for detailed information, see [46]). These findings suggest that the impulsive excitation of the B_{2g} phonon, as observed in our experiment, is governed by a coherent lattice distortion emergent in response to the optically induced change in the projection of angular momentum of the Dy^{3+} ions.

It is also interesting to consider the case of $\Delta M_L = 2$, facilitated by two distinct $Y_2^3 \rightarrow Y_0^3$ and $Y_3^3 \rightarrow Y_1^3$ single-electron transitions. The symmetry analysis (see [46]) shows that such electronic perturbation might trigger a lattice distortion leading to the excitation of complementary symmetry A_g and B_{1g} phonons. While this transition is characterized by a smaller probability, it demonstrates a possibility of resonant optical excitation of the A_g phonon mode.

6.4 Conclusion

To conclude, we have shown that in DyFeO_3 optical pumping using femtosecond pulses of light excites coherent THz dynamics of A_g and B_{2g} phonon modes dominated by the vibrations of the sublattice of the Dy^{3+} ions. We demonstrate a strong coupling between the optical excitation of the B_{2g} mode and the electronic $f-f$ transition from the ${}^6\text{H}_{15/2}$ to ${}^6\text{H}_{11/2}$ state in Dy^{3+} ions. Our findings,

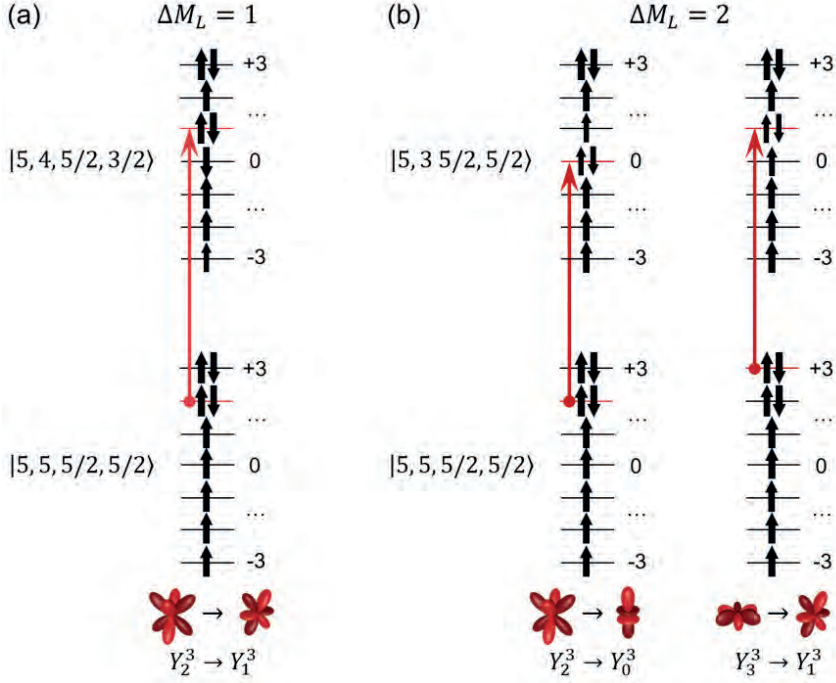


Figure 6.7: The energy levels diagram illustrates optical transitions (depicted by red arrows) that entail a change in the projection of the angular momentum (ΔM_L) within the total angular momentum eigenstates of Dy^{3+} ions with a $4f^9$ electronic configuration. The small black arrows indicate the spins of individual electrons. (a) The single-electron transition from the ground $|5; 5; 5/2; 5/2\rangle$ to $|5; 4; 5/2; 3/2\rangle$ excited state is accompanied by $\Delta M_L = 1$. The available change in the electronic wavefunction $Y_2^3 \rightarrow Y_1^3$ is shown below. (b) The single-electron transition from the ground $|5; 5; 5/2; 5/2\rangle$ to $|5; 4; 5/2; 3/2\rangle$ excited state is accompanied by $\Delta M_L = 2$. The available changes in the electronic wavefunctions $Y_2^3 \rightarrow Y_0^3$ and $Y_3^3 \rightarrow Y_1^3$ are shown below.

supported by quantum mechanical Clebsch-Gordan formalism and symmetry analysis, reveal that the dominant mechanism of excitation of the mode is due to a transition to a total angular momentum eigenstate denoted as $|5; 4; 5/2; 3/2\rangle$. This transition induces a change in the projection of Dy^{3+} orbital momentum ($\Delta M_L = 1$), concomitant with a coherent lattice distortion leading to the emis-

sion of the B_{2g} coherent phonon. Although the excitation of the fully symmetric A_g mode can be sufficiently explained by an off-resonant ISRS process, our theory suggests that resonance enhancement is possible when the energy of the pump photon pulse aligns with the ${}^6\text{H}_{15/2} \rightarrow {}^6\text{H}_{11/2}$ transition. The showcased control of crystal lattices via resonant pumping of electronic $f - f$ transitions not only enhances our understanding of electron-phonon coupling in complex compounds but also extends the optical control of crystal lattices beyond the recently demonstrated resonant pumping of the complementary $d - d$ transitions [3, 50, 51]. The demonstrated control of the RE lattice can be effectively employed to manipulate coupled electric and magnetic order parameters in the ordered phases of type-II multiferroics, where ferroelectric lattice distortions and net electric polarization are directly linked to the RE spin ordering [34, 52, 53]. The optically induced lattice distortions can be employed to impact RE spin-ordering, potentially activate coherent electromagnons, or interact with them. Moreover, the discovered interplay between the symmetry of optically excited RE orbital states and their lattice modes offers a promising method for time-resolved probing of multiferroicity in RE-based compounds. In particular, coherent phonon spectroscopy demonstrated here could help detect the dynamic signatures of multiferroicity, marked by the loss of center inversion and thus noticeable changes in the phonon spectrum.

Appendix A

Additional Data

A.1 Frequencies of Raman-active phonons in DyFeO_3

Table A1 presents the frequencies of Raman-active modes, obtained through ab-initio density-functional theory (DFT) calculations of the lattice dynamics in DyFeO_3 (col. 1). These results are compared to our experimental pump-probe data (col. 2), as well as Raman scattering experiments (col. 3) and previous ab-initio DFT studies (col. 4) done by Weber et al. [39]. The considered phonon modes are highlighted in red. For details of the DFT calculations see [46].

Phonon mode	DFT, THz	Our experiment, THz	Experiment [39], THz	DFT Ref. [39], THz
A_g (1)	3.21	—	3.39	3.35
A_g (2)	3.99	4.27 \pm 0.01	4.20	4.21
A_g (3)	7.46	—	7.82	7.85
A_g (4)	9.83	—	10.22	9.95
A_g (5)	12.23	—	12.65	12.65
A_g (6)	12.23	—	12.50	12.46
A_g (7)	12.98	—	12.65	12.65
A_g (8)	14.39	—	14.87	14.69
B_{1g} (1)	4.07	—	—	4.04
B_{1g} (2)	7.35	—	—	7.49
B_{1g} (3)	10.58	—	10.82	10.76
B_{1g} (4)	12.56	—	12.80	12.80
B_{1g} (5)	17.72	—	—	17.78
B_{2g} (1)	3.21	—	3.33	3.27
B_{2g} (2)	4.65	4.93 \pm 0.08	4.89	4.88
B_{2g} (3)	8.93	—	9.74	9.32
B_{2g} (4)	10.43	—	—	10.52
B_{2g} (5)	14.21	—	14.81	14.45
B_{2g} (6)	15.80	—	—	16.01
B_{2g} (7)	18.29	—	18.70	18.35
B_{3g} (1)	3.60	—	—	3.69
B_{3g} (2)	9.20	—	—	9.32
B_{3g} (3)	12.50	—	12.98	12.71
B_{3g} (4)	13.64	—	14.21	13.79
B_{3g} (5)	19.10	—	19.16	19.10

Table A.1: Frequencies of Raman-active phonons in DyFeO₃.

References

- [1] I. A. Mogunov, S. Lysenko, A. E. Fedianin, F. E. Fernández, A. Rúa, A. J. Kent, A. V. Akimov, and A. M. Kalashnikova. Large non-thermal contribution to picosecond strain pulse generation using the photo-induced phase transition in VO_2 . *Nat. Commun.*, 11:1, 2020.
- [2] L. A. Shelukhin, N. A. Pertsev, A. V. Scherbakov, D. L. Kazenwadel, D. A. Kirilenko, S. J. Hämäläinen, S. van Dijken, and A. M. Kalashnikova. Laser-induced magnetization precession in individual magnetoelastic domains of a multiferroic $\text{Co}_{40}\text{Fe}_{40}\text{B}_{20}/\text{BaTiO}_3$ composite. *Phys. Rev. Appl.*, 14:034061, 2020.
- [3] D. Khusyainov et al. Ultrafast laser-induced spin–lattice dynamics in the van der waals antiferromagnet CoPS_3 . *APL Mater.*, 11:071104, 2023.
- [4] R. Merlin. Generating coherent thz phonons with light pulses. *Solid State Commun.*, 102:207, 1997.
- [5] T. E. Stevens, J. Kuhl, and R. Merlin. Coherent phonon generation and the two stimulated raman tensors. *Phys. Rev. B*, 65:144304, 2002.
- [6] D. Bossini, A. M. Kalashnikova, R. V. Pisarev, Th. Rasing, and A. V. Kimel. Controlling coherent and incoherent spin dynamics by steering the photoinduced energy flow. *Phys. Rev. B*, 89:060405(R), 2014.
- [7] Y. Huang et al. Ultrafast measurements of mode-specific deformation potentials of Bi_2Te_3 and Bi_2Se_3 . *Phys. Rev. X*, 13:041050, 2023.
- [8] D. Afanasiev, I. Razdolski, K. M. Skibinsky, D. Bolotin, S. V. Yagupov, M. B. Strugatsky, A. Kirilyuk, Th. Rasing, and A. V. Kimel. Laser excitation of lattice-driven anharmonic magnetization dynamics in dielectric FeBO_3 . *Phys. Rev. Lett.*, 112:147403, 2014.
- [9] T. Kubacka et al. Large-amplitude spin dynamics driven by a thz pulse in resonance with an electromagnon. *Science*, 343:1333, 2014.
- [10] M. J. Neugebauer, D. M. Juraschek, M. Savoini, P. Engeler, L. Boie, E. Abreu, N. A. Spaldin, and S. L. Johnson. Comparison of coherent phonon generation by electronic and ionic raman scattering in LaAlO_3 . *Phys. Rev. Res.*, 3:013126, 2021.
- [11] S. Sharma, S. Shallcross, P. Elliott, and J. K. Dewhurst. Making a case for femto-phono-magnetism with fept. *Sci. Adv.*, 8:eabq2021, 2022.
- [12] S. F. Maehrlein et al. Dissecting spin-phonon equilibration in ferrimagnetic insulators by ultrafast lattice excitation. *Sci. Adv.*, 4:eaar5164, 2018.

- [13] A. Stupakiewicz, C. S. Davies, K. Szerenos, D. Afanasiev, K. S. Rabinovich, A. V. Boris, A. Caviglia, A. V. Kimel, and A. Kirilyuk. Ultrafast phononic switching of magnetization. *Nat. Phys.*, 17:4, 2021.
- [14] R. Mankowsky, A. von Hoegen, M. Först, and A. Cavalleri. Ultrafast reversal of the ferroelectric polarization. *Phys. Rev. Lett.*, 118:197601, 2017.
- [15] M. Henstridge, M. Först, E. Rowe, M. Fechner, and A. Cavalleri. Nonlocal nonlinear phononics. *Nat. Phys.*, 18:4, 2022.
- [16] A. Cavalleri, Th. Dekorsy, H. H. W. Chong, J. C. Kieffer, and R. W. Schoenlein. Evidence for a structurally-driven insulator-to-metal transition in VO_2 : A view from the ultrafast timescale. *Phys. Rev. B*, 70:161102(R), 2004.
- [17] A. D. Caviglia et al. Ultrafast strain engineering in complex oxide heterostructures. *Phys. Rev. Lett.*, 108:136801, 2012.
- [18] T. F. Nova, A. S. Disa, M. Fechner, and A. Cavalleri. Metastable ferroelectricity in optically strained SrTiO_3 . *Science*, 364:1075, 2019.
- [19] C. Gattinoni, N. Strkalj, R. Härdi, M. Fiebig, M. Trassin, and N. A. Spaldin. Interface and surface stabilization of the polarization in ferroelectric thin films. *Proc. Natl. Acad. Sci. U.S.A.*, 117:28589, 2020.
- [20] D. Fausti, R. I. Tobey, N. Dean, S. Kaiser, A. Dienst, and M. C. Hoffmann. Light-induced superconductivity in a stripe-ordered cuprate. *Science*, 331:189, 2011.
- [21] D. Afanasiev, B. A. Ivanov, A. Kirilyuk, Th. Rasing, R. V. Pisarev, and A. V. Kimel. Control of the ultrafast photoinduced magnetization across the morin transition in DyFeO_3 . *Phys. Rev. Lett.*, 116:097401, 2016.
- [22] A. S. Disa, T. F. Nova, and A. Cavalleri. Engineering crystal structures with light. *Nat. Phys.*, 17:10, 2021.
- [23] M. Buzzi et al. Photomolecular high-temperature superconductivity. *Phys. Rev. X*, 10:031028, 2020.
- [24] D. M. Juraschek, M. Fechner, A. V. Balatsky, and N. A. Spaldin. Dynamical multiferroicity. *Phys. Rev. Mater.*, 1:014401, 2017.
- [25] D. M. Juraschek, T. Neuman, and P. Narang. Giant effective magnetic fields from optically driven chiral phonons in $4f$ paramagnets. *Phys. Rev. Res.*, 4:013129, 2022.
- [26] C. P. Romao and D. M. Juraschek. Light makes atoms behave like electromagnetic coils. *Nature*, 628:505, 2024.

- [27] K. P. Belov, A. K. Zvezdin, A. M. Kadomtseva, and R. Z. Levitin. Spin-reorientation transitions in rare-earth magnets. *Sov. Phys. Usp.*, 19:574, 1976.
- [28] R. L. White. Review of recent work on the magnetic and spectroscopic properties of the rare-earth orthoferrites. *J. Appl. Phys.*, 40:1061, 1969.
- [29] A. K. Zvezdin and V. M. Matveev. Theory of the magnetic properties of dysprosium orthoferrite. *Sov. Phys. JETP*, 50:543, 1979.
- [30] F.-K. Chiang, M.-W. Chu, F. C. Chou, H. T. Jeng, H. S. Sheu, F. R. Chen, and C. H. Chen. Effect of jahn-teller distortion on magnetic ordering in dy(Fe,Mn)O_3 perovskites. *Phys. Rev. B*, 83:245105, 2011.
- [31] A. Sasani, J. Íñiguez, and E. Bousquet. Origin of nonlinear magnetoelectric response in rare-earth orthoferrite perovskite oxides. *Phys. Rev. B*, 105:064414, 2022.
- [32] A. K. Zvezdin and A. A. Mukhin. Magnetoelectric interactions and phase transitions in a new class of multiferroics with improper electric polarization. *JETP Lett.*, 88:505, 2008.
- [33] D. Afanasiev, A. K. Zvezdin, and A. V. Kimel. Laser-induced shift of the morin point in antiferromagnetic dyFeO_3 . *Opt. Express*, 23:23978, 2015.
- [34] Y. Tokunaga, S. Iguchi, T. Arima, and Y. Tokura. Magnetic-field-induced ferroelectric state in dyFeO_3 . *Phys. Rev. Lett.*, 101:097205, 2008.
- [35] R. V. Mikhaylovskiy, T. J. Huisman, A. I. Popov, A. K. Zvezdin, Th. Rasing, R. V. Pisarev, and A. V. Kimel. Terahertz magnetization dynamics induced by femtosecond resonant pumping of the dy_3^+ subsystem in the multisublattice antiferromagnet dyFeO_3 . *Phys. Rev. B*, 92:094437, 2015.
- [36] A. Sasani, J. Íñiguez, and E. Bousquet. Magnetic phase diagram of rare-earth orthorhombic perovskite oxides. *Phys. Rev. B*, 104:064431, 2021.
- [37] T. N. Stanislavchuk, Y. Wang, Y. Janssen, G. L. Carr, S.-W. Cheong, and A. A. Sirenko. Magnon and electromagnon excitations in multiferroic dyFeO_3 . *Phys. Rev. B*, 93:094403, 2016.
- [38] D. L. Wood, J. P. Remeika, and E. D. Kolb. Optical spectra of rare-earth orthoferrites. *J. Appl. Phys.*, 41:5315, 2003.
- [39] M. C. Weber, M. Guennou, H. J. Zhao, J. Íñiguez, R. Vilarinho, A. Almeida, J. A. Moreira, and J. Kreisel. Raman spectroscopy of rare-earth orthoferrites rFeO_3 ($\text{r} = \text{La, Sm, Eu, Gd, Tb, Dy}$). *Phys. Rev. B*, 94:214103, 2016.
- [40] H. C. Gupta, M. K. Singh, and L. M. Tiwari. Lattice dynamic investigation of raman and infrared wavenumbers at the zone center of orthorhombic rFeO_3 ($\text{r} = \text{Tb, Dy, Ho, Er, Tm}$) perovskites. *J. Raman Spectrosc.*, 33:67, 2002.

- [41] R. Iida, T. Satoh, T. Shimura, K. Kuroda, B. A. Ivanov, Y. Tokunaga, and Y. Tokura. Spectral dependence of photo-induced spin precession in dyfeo_3 . *Phys. Rev. B*, 84:064402, 2011.
- [42] S. L. Johnson, M. Savoini, P. Beaud, G. Ingold, U. Staub, F. Carbone, L. Castiglioni, M. Hengsberger, and J. Osterwalder. Watching ultrafast responses of structure and magnetism in condensed matter with momentum-resolved probes. *Struct. Dyn.*, 4.
- [43] J. R. Hortensius, D. Afanasiev, A. Sasani, E. Bousquet, and A. D. Caviglia. Ultrafast strain engineering and coherent structural dynamics from resonantly driven optical phonons in laalo_3 . *npj Quantum Mater.*, 5:1, 2020.
- [44] D. Afanasiev, J. R. Hortensius, B. A. Ivanov, A. Sasani, E. Bousquet, Y. M. Blanter, R. V. Mikhaylovskiy, A. V. Kimel, and A. D. Caviglia. Ultrafast control of magnetic interactions via light-driven phonons. *Nat. Mater.*, 20:607, 2021.
- [45] A. V. Kimel, A. Kirilyuk, P. A. Usachev, R. V. Pisarev, A. M. Balbashov, and T. Rasing. Ultrafast non-thermal control of magnetization by instantaneous photomagnetic pulses. *Nature*, 435:7042, 2005.
- [46] TT Gareev, Alireza Sasani, DI Khusyainov, Eric Bousquet, ZV Gareeva, AV Kimel, and D Afanasiev. Optical excitation of coherent thz dynamics of the rare-earth lattice through resonant pumping of f-f electronic transition in a complex perovskite dyfeo_3 . *Physical Review Letters*, 133(24):246901, 2024.
- [47] M. C. Weber, J. Kreisel, P. A. Thomas, M. Newton, K. Sardar, and R. I. Walton. Phonon raman scattering of rcro_3 perovskites ($r = y, \text{la}, \text{pr}, \text{sm}, \text{gd}, \text{dy}, \text{ho}, \text{yb}, \text{lu}$). *Phys. Rev. B*, 85:054303, 2012.
- [48] S. Venugopalan, M. Dutta, A. K. Ramdas, and J. P. Remeika. Magnetic and vibrational excitations in rare-earth orthoferrites: A raman scattering study. *Phys. Rev. B*, 31:1490, 1985.
- [49] F. J. Kahn, P. S. Pershan, and J. P. Remeika. Ultraviolet magneto-optical properties of single-crystal orthoferrites, garnets, and other ferric oxide compounds. *Phys. Rev.*, 186:891, 1969.
- [50] F. Mertens et al. Ultrafast coherent thz lattice dynamics coupled to spins in the van der waals antiferromagnet feps_3 . *Adv. Mater.*, 35:2208355, 2023.
- [51] A. Marciniak et al. Vibrational coherent control of localized $d-d$ electronic excitation. *Nat. Phys.*, 17:3, 2021.
- [52] D. Khomskii. Classifying multiferroics: Mechanisms and effects. *Physics*, 2:20, 2009.

-
- [53] A. P. Pyatakov and A. K. Zvezdin. Magnetoelectric and multiferroic media. *Phys. Usp.*, 55:557, 2012.

Summary

Controlling the magnetic state of materials with the lowest possible energy consumption and at the fastest achievable time scale is among the grand challenges in modern condensed matter physics. At a time when sustainable, energy-efficient technologies are increasingly in demand, our work presents a novel pathway to harness ultrafast phenomena that have the potential to revolutionize data storage and spintronic devices. We exploit femtosecond laser pulses and electrical gating to steer both spin and lattice dynamics along non-equilibrium trajectories that remain largely unexplored.

In **Chapter 1**, we introduce the fundamental principles underlying magnetism, detailing the role of spin and orbital contributions to the magnetic moment as well as the various magnetic orders – ferromagnetic, antiferromagnetic, and ferrimagnetic – that form the basis of current storage technologies. Special attention is given to the magnetoelectric effect, wherein electric fields are shown to influence magnetic order. By operating on timescales that are much shorter than those associated with conventional atomic and spin motions, ultrashort laser pulses allow us to excite magnetic systems into strongly non-equilibrium states, opening new routes for switching magnetic states.

Chapter 2 describes the state-of-the-art experimental techniques developed in this work. Our approach combines ultrafast pump-probe spectroscopy, spatially resolved magneto-optical imaging, and electrical gating to probe and control the dynamics of magnetic and lattice degrees of freedom. The detailed discussion encompasses the fundamentals of light-matter interaction, covering both linear and nonlinear regimes, such as those involving Second Harmonic Generation (SHG), that are crucial for detecting subtle magnetic order even in systems lacking a net moment.

In **Chapter 3**, we report our first striking observation in an iron garnet film. A femtosecond laser pulse with a Gaussian intensity profile is found to trigger strongly inhomogeneous spin dynamics. Ultrafast imaging reveals ring-like magneto-optical patterns and localized phase shifts within the ex-

cited region. Analysis shows that these spatial variations arise from local gradients in temperature and magnetic anisotropy, resulting in differential torques within the pumped area. This finding suggests that conventional pump-probe experiments might underestimate the full scale of laser-induced spin dynamics if spatial variations are not taken into account.

Chapter 4 extends our investigation by introducing electrical gating to the ultrafast optical methodology. Experiments on an iron garnet film at room temperature demonstrate that an externally applied electric field (on the order of 0.5 MV/m) can dramatically enhance the excitation of coherent spin waves. Time-resolved magneto-optical imaging, corroborated by numerical simulations using the Landau–Lifshitz–Gilbert equation, reveals that the electric field serves as a tuning parameter for the light–spin coupling. Importantly, electrical gating allows for spatial control defined by the electrode geometry, thereby overcoming the inherent diffraction limit of optical excitation that can be potentially used for Electrically Assisted All-Optical Switching.

In **Chapter 5**, the focus shifts to antiferromagnetic systems, where operating frequencies can reach the THz regime – about 1000 times faster than those of conventional data storage devices operating in the GHz range. We investigate the electric-field-driven motion of domain walls in Cr_2O_3 thin films. By employing Second Harmonic Generation imaging combined with a localized high-voltage tip, we show that the application of an electric field leads to reproducible attraction or repulsion of the domain walls, contingent on the polarity of the applied field. Temperature-dependent hysteresis loops further reveal that the dynamics of domain wall displacement are highly sensitive near the Néel temperature. This chapter not only validates the robustness of the magnetoelectric coupling in Cr_2O_3 but also provides important insights for the development of antiferromagnetic memory devices.

Finally, **Chapter 6** investigates the resonant optical excitation of terahertz (THz) lattice dynamics in the rare-earth perovskite DyFeO_3 – a material known for exhibiting one of the strongest magnetoelectric effects. By selectively pumping the $f - f$ electronic transitions in Dy^{3+} ions, we show that it is possible to impulsively launch coherent THz phonon modes, specifically those with A_g and B_{2g} symmetries. Detailed pump-probe measurements, supported by Fast Fourier Transform analysis and corroborated by density-functional theory (DFT) calculations, reveal that the excitation

mechanism is intimately linked to a change in the orbital angular momentum of Dy^{3+} ions. This mechanism offers a promising route for extending optical control of crystal lattices and manipulating coupled spin-lattice phenomena in multiferroic materials.

In summary, our work demonstrates that merging ultrafast optical excitation with electrical gating enables probing and controlling magnetization and lattice vibrations in complex oxides with unprecedented speed and spatial precision – paving the way for faster, more energy-efficient spintronic, data-storage, and multiferroic devices.

Outlook

While femtosecond laser pulses have long been known to trigger magnetization dynamics, and electric fields have independently been used to control magnetization in magneto-electric materials, the combined use of both stimuli has remained largely unexplored. In this thesis, we demonstrated that electric fields and ultrafast optical excitation can indeed be applied together to manipulate spin dynamics.

This combination opens a new pathway for overcoming the diffraction limit in ultrafast all-optical switching. Our numerical simulations based on the Landau-Lifshitz-Gilbert equation for iron garnets (Chapter 4) reveal that an optimized light-spin coupling regime can be achieved by adjusting the applied electric field. This suggests that ultrafast electric-field-assisted all-optical switching is experimentally feasible. Achieving this will require developing alternative electrode geometries that support higher field strengths – for example, by reducing the distance between electrodes. Such advancements would not only improve switching efficiency but also enable nanoscale spatial control, as the switched region would be defined by electrode size – bypassing the optical diffraction limit. This could allow nucleation of topological spin textures, such as magnetic vortices or skyrmions,* opening new avenues for spin-based logic and memory devices.

Furthermore, our results on antiferromagnetic Cr_2O_3 show that localized electric fields can precisely control domain wall motion and enable stable domain writing. Since ultrashort laser pulses are also capable of ex-

*Vélez, S. *et al.* Nat. Nanotechnol. 17, 834–841 (2022). <https://doi.org/10.1038/s41565-022-01144-x>

citing THz spin modes in antiferromagnets, combining optical and electric stimuli potentially offers a powerful mechanism for controlling magnetic order in antiferromagnets at sub-picosecond timescales.

Together, these results point toward a strategy where electric and optical control are combined to enable ultrafast, nanoscale manipulation of magnetic states, offering a faster and more energy-efficient approach to magnetization control.

Samenvatting

Het beheersen van de magnetische toestand van materialen met het laagst mogelijke energieverbruik en in de snelst haalbare tijdschaal is een van de grote uitdagingen in de moderne gecondenseerde materie fysica. Nu duurzame, energiezuinige technologieën steeds meer worden gevraagd, biedt ons werk een nieuw pad om ultrasnelle fenomenen te benutten die het potentieel hebben om datastorage en spintronica radicaal te veranderen. We benutten femtoseconde laserpulsen en elektrische gating om zowel spin- als rooster dynamica langs niet-evenwichts trajecten te sturen die nog grotendeels onontdekt zijn.

In **Hoofdstuk 1** introduceren we de fundamentele principes van magnetisme, met details over de rol van spin- en orbitaalbijdragen aan het magnetische moment, en de verschillende magnetische orden – ferromagnetisch, antiferromagnetisch en ferrimagetisch – die de basis vormen van huidige opslagtechnologieën. We besteden speciale aandacht aan het magneto-elektrisch effect, waarbij elektrische velden de magnetische ordening beïnvloeden. Door te opereren op tijdschalen die veel korter zijn dan die van conventionele atomaire en spinbewegingen, kunnen ultrakorte laserpulsen magnetische systemen in sterk niet-evenwichtstoestanden brengen en zo nieuwe routes voor het schakelen van magnetische toestanden openen.

Hoofdstuk 2 beschrijft de experimentele top technieken die in dit werk zijn ontwikkeld. Onze aanpak combineert ultrasnelle pump-probe spectroscopie, ruimtelijk geresolveerde magneto-optische beeldvorming en elektrische gating om de dynamica van magnetische en rooster vrijheidsgraden te onderzoeken en te beheersen. De gedetailleerde bespreking omvat de basis van licht-materie-interactie, zowel in de lineaire als de niet-lineaire regimes, zoals bij Second Harmonic Generation (SHG), die cruciaal zijn voor het opsporen van subtiele magnetische orden, zelfs in systemen zonder netto moment.

In **Hoofdstuk 3** rapporteren we onze eerste opvallende waarneming in een ijzer garnetfilm. Een femtoseconde laserpuls met een Gaussiaanse

intensiteits profiel blijkt sterke inhomogene spin dynamica teweeg te brengen. Ultrafast beeldvorming onthult ringachtige magneto-optische patronen en gelokaliseerde fasedraaiingen binnen het geactiveerde gebied. Analyse toont aan dat deze ruimtelijke variaties voortkomen uit lokale gradienten in temperatuur en magnetische anisotropie, wat resulteert in differentiële krachten binnen het gepompte gebied. Deze bevinding suggereert dat conventionele pump-probe-experimenten mogelijk de volledige omvang van laser-geïnduceerde spin dynamica onderschatten als ruimtelijke variaties niet in aanmerking worden genomen.

In **Hoofdstuk 4** breiden we ons onderzoek uit door elektrische gating toe te voegen aan de ultrasnelle optische methodiek. Experimenten op een ijzer garnetfilm bij kamertemperatuur tonen aan dat een extern aangelegd elektrisch veld (van ongeveer 0.5 MV/m) de excitatie van coherente spin golven dramatisch kan versterken. Tijd geresolveerde magneto-optische beeldvorming, ondersteund door numerieke simulaties met de Landau–Lifshitz–Gilbert vergelijking, laten zien dat het elektrische veld fungeert als stem knop voor de licht-spin koppeling. Belangrijk is dat elektrische gating ruimtelijke controle mogelijk maakt via de elektrode geometrie, waarmee de inherente diffractie grens van optische excitatie kan worden overwonnen—potentieel bruikbaar voor Electrically Assisted All-Optical Switching.

In **Hoofdstuk 5** verschuift de focus naar antiferromagnetische systemen, waar bedrijfs frequenties de THz-regio kunnen bereiken—ongeveer 1000 keer sneller dan conventionele opslag apparaten in de GHz-range. We onderzoeken het door elektrische velden aangedreven bewegings gedrag van domein wanden in Cr_2O_3 -dunne films. Met behulp van SHG-beeldvorming gecombineerd met een gelokaliseerde hoge-spanningstip tonen we aan dat het aanleggen van een elektrisch veld leidt tot repeteerbare aantrekking of afstoting van de domeinwanden, afhankelijk van de veld polariteit. Temperatuurafhankelijke hysteresis lussen onthullen verder dat de dynamica van domeinwand verplaatsing zeer gevoelig zijn rond de Néel-temperatuur. Dit hoofdstuk valideert niet alleen de robuustheid van de magneto-elektrische koppeling in Cr_2O_3 , maar geeft ook belangrijke inzichten voor de ontwikkeling van antiferromagnetische geheugensystemen.

Ten slotte onderzoekt **Hoofdstuk 6** de resonante optische excitatie van terahertz (THz) rooster dynamica in het zeldzame-aarde perovskiet DyFeO_3 —een materiaal dat bekendstaat om een van de sterkste magneto-elektrische effecten. Door selectief de f - f elektronische overgangen in Dy^{3+} -

ionen te pompen, laten we zien dat het mogelijk is om impulsgewijs coherente THz-fononmodi te lanceren, met name die van A_g - en B_{2g} -symmetrieën. Gedetailleerde pump-probe-metingen, ondersteund door Fast Fourier Transform analyse en bekrachtigd door density-functional theory (DFT) berekeningen, onthullen dat het excitatiemechanisme nauw samenhangt met een verandering in de orbitaal momentumcomponent van Dy^{3+} -ionen. Dit mechanisme biedt een veelbelovende route om optische controle over kristalroosters en gekoppelde spin-rooster fenomenen in multiferroïsche materialen uit te breiden.

Samenvattend toont ons werk aan dat het samenvoegen van ultrasnelle optische excitatie met elektrische gating het mogelijk maakt om magnetisatie en rooster trillingen in complexe oxiden te onderzoeken en te beheersen met ongeëvenaarde snelheid en ruimtelijke precisie—en zo de weg vrijmaakt voor snellere, energiezuinigere spintronische, data-opslag- en multiferroïsche apparaten.

Vooruitzicht

Hoewel femtoseconde laserpulsen al lang bekendstaan om magnetisatie dynamica te triggeren en elektrische velden onafhankelijk worden gebruikt om magnetisatie in magneto-elektrische materialen te beheersen, is het gecombineerde gebruik van beide stimuli grotendeels onontgonnen gebleven. In dit proefschrift hebben we aangetoond dat elektrische velden en ultrasnelle optische excitatie samen kunnen worden toegepast om spin dynamica te manipuleren.

Deze combinatie opent een nieuw pad om de diffractie grens in ultrasnel all-optical switching te overwinnen. Onze numerieke simulaties op basis van de Landau–Lifshitz–Gilbert-vergelijking voor ijzer garnetten (**Hoofdstuk 4**) laten zien dat een optimaal licht-spin koppelingsregime kan worden bereikt door het aangelegde elektrische veld bij te stellen. Dit suggereert dat ultrasnel elektrisch ondersteund all-optical switching experimenteel haalbaar is. Om dit te realiseren, moeten alternatieve elektrode geometrieën worden ontwikkeld die hogere veldsterkten ondersteunen, bij voorbeeld, door de afstand tussen de elektroden te verkleinen. Dergelijke verbeteringen zouden niet alleen de switching efficiëntie verhogen, maar ook nanoschaal ruimtelijke controle mogelijk maken, aangezien het geschakelde

gebied wordt bepaald door de grootte van de elektrode—waardoor de optische diffractie grens wordt omzeild. Dit zou de nucleatie van topologische spin structuren, zoals magnetische vortexen of skyrmions,* mogelijk maken en zo nieuwe wegen openen voor spingebaseerde logica en geheugenapparaten.

Bovendien tonen onze resultaten op antiferromagnetisch Cr_2O_3 aan dat gelokaliseerde elektrische velden domein wand beweging precies kunnen beheersen en stabiel domeinschrijven mogelijk maken. Aangezien ultrakorte laserpulsen ook THz-spinmodi in antiferromagneten kunnen excitëren, biedt de combinatie van optische en elektrische stimuli potentieel een krachtig mechanisme om magnetische ordening in antiferromagneten op sub-picoseconde tijdschalen te beheersen.

Gezamenlijk wijzen deze bevindingen op een strategie waarbij elektrische en optische controle worden gecombineerd om ultrasnelle, nanoschaal-manipulatie van magnetische toestanden mogelijk te maken—en zo een snellere en energiezuinigere benadering van magnetisatie beheersing te bieden.

*Vélez, S. *et al.* Nat. Nanotechnol. 17, 834–841 (2022).

Research Data Management

This thesis research has been carried out in accordance with the research data management policy of the Institute for Molecules and Materials (IMM) of Radboud University, the Netherlands*.

The following datasets have been produced during the research:

- **Chapter 3:** T.T. Gareev, N.E. Khokhlov, L. Körber, A. V. Kimel
“Strongly inhomogeneous spin dynamics induced by ultrashort laser pulses with a gradient intensity profile”, *Physical Review Letters*, **135**, 156701 (2025),
<https://doi.org/10.1103/gspf-b9n2>
(published)
 - *CNCZ, Radboud University (2025):*
`smb://uscm-ssi-srv.science.ru.nl/uscm-ssi/TimurGareev/Thesis/RDM/2025_Inhomogeneous_Spin_Dynamics`
 - *EU Open Research Repository Zenodo (2025):*
<https://zenodo.org/records/15881053>
- **Chapter 4:** T.T. Gareev, N.E. Khokhlov, L. Körber, A.P. Pyatakov, A.V. Kimel, “Ultrafast Imaging of Electrically-Gated Laser-Induced Spin Dynamics”.
(manuscript submitted, preprint published)

*<https://www.ru.nl/en/about-us/policies-and-regulations/research-data-management/guidelines-for-research-data-management>

- *CNCZ, Radboud University (2025):*
`smb://uscm-ssi-srv.science.ru.nl/uscm-ssi/TimurGareev/Thesis/RDM/2025_Electrically_Gated_Spin_Dynamics`
- *EU Open Research Repository Zenodo (2025):*
<https://zenodo.org/records/15737942>
- **Chapter 5:** N.E. Khokhlov, T.T. Gareev, A. G. Buzdakov, S. Artyukhin, A. K. Zvezdin, A.V. Kimel, “Electric field control of antiferromagnetic domain patterns in Cr_2O_3 ”.
 (manuscript process)
 - *CNCZ, Radboud University (2025):*
`smb://uscm-ssi-srv.science.ru.nl/uscm-ssi/TimurGareev/Thesis/RDM/2024_Electric_Field_Control_AFM_DW`
- **Chapter 6:** T.T. Gareev, A. Sasani, D. I. Khusyainov, E. Bousquet, Z.V. Gareeva, A.V. Kimel, and D. Afanasiev, “Optical excitation of coherent THz dynamics of the rare-earth lattice through resonant pumping of $f - f$ electronic transition in a complex perovskite DyFeO_3 ”, *Physical Review Letters*, **133**, 246901 (2024),
<https://doi.org/10.1103/PhysRevLett.133.246901>
 (published)
 - *CNCZ, Radboud University (2025):*
`smb://uscm-ssi-srv.science.ru.nl/uscm-ssi/TimurGareev/Thesis/RDM/2024_PRL_THz_phonon_dynamics_in_DyFeO3`

List of Publications

- [1] N.E. Khokhlov, **T.T. Gareev**, A. G. Buzdakov, S. Artyukhin, A. K. Zvezdin, A.V. Kimel, “Electric field control of antiferromagnetic domain patterns in Cr_2O_3 ” (in preparation).
- [2] J. Groefsema, V. Radovskaia, T. Janssen, N. Dessmann, P. Kim, **T.T. Gareev**, M.X. Na, J.R. Hortensius, A. Caviglia, Th. Rasing, A. Kiriliouk, C. Davies, A.V. Kimel, D. Afanasiev, “Two Distinct Regimes in Phonon-Induced Non-Equilibrium Magnetization Dynamics” (submitted).
- [3] **T.T. Gareev**, N.E. Khokhlov, L. Körber, A.P. Pyatakov, A.V. Kimel, “Electrically-gated laser-induced spin dynamics in magneto-electric iron garnet at room temperature”, arXiv preprint arXiv:2506.20366 (2025).
<https://doi.org/10.48550/arXiv.2506.20366>
- [4] **T.T. Gareev**, N.E. Khokhlov, L. Körber, A.V. Kimel, “Strongly inhomogeneous spin dynamics induced by ultrashort laser pulses with a gradient intensity profile”, *Physical Review Letters*, **135**, 156701 (2025).
<https://doi.org/10.1103/gspf-b9n2>
- [5] **T.T. Gareev**, A. Sasani, D. I. Khusyainov, E. Bousquet, Z.V. Gareeva, A.V. Kimel, and D. Afanasiev, “Optical excitation of coherent THz dynamics of the rare-earth lattice through resonant pumping of $f-f$ electronic transition in a complex perovskite DyFeO_3 ”, *Physical Review Letters*, **133**, 246901 (2024).
<https://doi.org/10.1103/PhysRevLett.133.246901>

- [6] F. Formisano, **T.T. Gareev**, D. I. Khusyainov, A.E. Fedianin, R.M. Dubrovin, P.P. Syrnikov, D. Afanasiev, R.V. Pisarev, A.M. Kalashnikova, J.H. Mentink, A.V. Kimel, “Coherent THz spin dynamics in antiferromagnets beyond the approximation of the Néel vector”, *APL Materials* **12.1** (2024).
<https://doi.org/10.1063/5.0180888>
- [7] D. Khusyainov, **T.T. Gareev**, V. Radovskaia, K. Sampathkumar, S. Acharya, M. Šiškins, S. Mañas-Valero, B.A. Ivanov, E. Coronado, Th. Rasing, A.V. Kimel, D. Afanasiev, “Ultrafast laser-induced spin-lattice dynamics in the van der Waals antiferromagnet CoPS₃”, *APL Materials* **11.7** (2023).
<https://doi.org/10.1063/5.0146128>
- [8] R.M. Vakhitov, R.V. Solonetsky, V.R. Gurjanova, A.R. Nizjamova, D.A. Sechin, **T.T. Gareev**, and A.P. Pyatakov, “Magnetic-field tuning of domain-wall multiferroicity”, *Physical Review B* **104.14**, 144407 (2021).
<https://doi.org/10.1103/PhysRevB.104.144407>
- [9] A.P. Pyatakov, **T.T. Gareev**, A.S. Kaminskiy, K.S. Antipin, E.P. Nikolaeva, D.P. Kulikova, A.S. Sergeev, and A.V. Nikolaev, “Magnetoelectricity of chiral micromagnetic structures,” in *Chirality, Magnetism and Magnetoelectricity: Separate Phenomena and Joint Effects in Metamaterial Structures*, pages 127–146 (2021).
https://doi.org/10.1007/978-3-030-62844-4_6
- [10] K.S. Antipin, **T.T. Gareev**, N.V. Myasnikov, E.P. Nikolaeva, A.P. Pyatakov, “Bipolar electric field-induced nucleation of magnetic domains with 90° domain walls”, *Journal of Applied Physics* **129.2** (2021).
<https://doi.org/10.1063/5.0029652>
- [11] D.P. Kulikova, **T.T. Gareev**, E.P. Nikolaeva, T.B. Kosykh, A.V. Nikolaev, Z.A. Pyatakova, A.K. Zvezdin, and A.P. Pyatakov, “The Mechanisms of Electric Field-Induced Magnetic Bubble Domain Blowing”, *Physica Status Solidi (RRL) – Rapid Research Letters* **12.6**, 1800066 (2018).
<https://doi.org/10.1002/pssr.201800066>

Curriculum Vitae

Personal Information

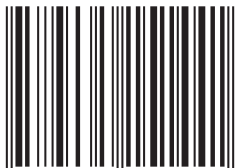
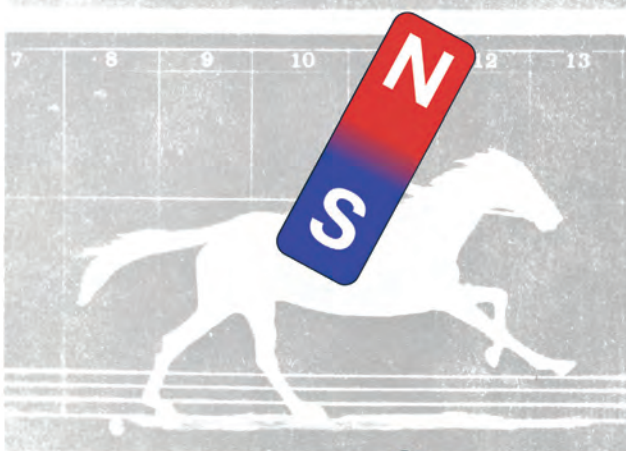
Name: Timur Tagirovich Gareev
Date of Birth: August 17, 1996
Place of Birth: Davlekanovo, Russia
Languages: Russian (native), English (fluent), Dutch (fluent),
German (basic)
Email: timur.tj17@gmail.com

Professional Experience

- **2025 – now:** Postdoctoral Researcher at Radboud University, Department of Ultrafast Spectroscopy of Correlated Materials, Nijmegen, the Netherlands.
- **2021 – 2025:** PhD Researcher at Radboud University, Department of Ultrafast Spectroscopy of Correlated Materials, Nijmegen, the Netherlands.
- **2023 – 2024:** Failure Analysis Engineer at NXP Semiconductors (secondment), Nijmegen, the Netherlands.
- **2024 – 2024:** Guest Researcher at Lancaster University (1 month), Lancaster, United Kingdom.

Education

- **2019 – 2021:** MSc in Physics, specialization in Quantum Oscillation Systems, Lomonosov Moscow State University, Moscow, Russia, *Cum Laude*.
- **2020 – 2020:** MSc Exchange Student (Erasmus+ fellow) at the Faculty of Science, Radboud University, Nijmegen, the Netherlands.
- **2014 – 2019:** BSc in Physics, specialization in Physics, Lomonosov Moscow State University, Moscow, Russia.
- **2012 – 2014:** High School Diploma, specialization in exact sciences, Lyceum 153 at Ufa Aviation State Technical University, Ufa, Russia.
- **2003 – 2012:** Middle School Diploma, Lyceum 6, Ufa, Russia.



9 789465 151441 >